Development of Low Cost CdS/CdTe Thin Film Solar Cells by Using Novel Materials

A Thesis Submitted to University of Liverpool

in Partial Fulfillment of the Requirements for

the Degree of Doctor of Philosophy

in the Department of Electrical Engineering and Electronics

By

Jingjin WU

Master of Science in Sustainable Energy Technologies,

Southampton University, Southampton, United Kingdom

Bachelor of Engineering in Electronic Science and Technology,

Xi'an Jiaotong University, Xi'an, China

Abstract

Cadmium Telluride (CdTe) thin film solar cells are one of the most promising solar cell technologies and share 5% of the photovoltaics market. CdTe thin film solar cells are expected to play a crucial role in the future photovoltaics market. The limitations of terawatt-scale CdTe solar cells deployment are scarcity of raw materials, low power conversion efficiency, and their stability. During the last few decades, intensive studies have been made to further understand the material properties, explore substitute materials, and get insight into the defect generation and distribution in solar cells. Yet, these problems are still not fully resolved. One of these significant topics is replacement of indium tin oxide (ITO). Following the introduction of aluminum doped zinc oxide (ZnO:Al or AZO) into thin film solar cells application, zinc oxide based transparent conducting oxides attract the attention from academic research institutes and industry. Zinc oxides are commonly doped with group III elements such as aluminium and gallium. Some researchers introduced group IV elements, including titanium, hafnium, zirconium, and obtained good properties. In our work, deposited zirconium doped zinc oxide (ZnO:Zr or ZrZO) by atomic layer deposition (ALD). Based on the advantage of precisely controlling of chemical ratio, the nature of ZrZO could be revealed. It is found that the ZrZO thin film has good thermal stability. By increasing zirconium concentration, the energy bandgap of ZrZO film follows the Burstein – Moss effect.

Another issue of CdTe solar cells is the doping of CdTe thin films, low carrier concentration in CdTe thin films hinders the open circuit voltage and thus power conversion efficiency. Copper is a compelling element that is used as a CdTe dopant; however, high concentration of copper ions results in severe solar cell degradation. One approach was to evaporate a few nm thick copper on CdTe thin film followed with annealing. Another approach was to introduce a buffer layer in between the CdTe thin film and back metallic electrode. Numerous works have been shown that Sb_2Te_3 layer performs better than copper-based buffer layer, and the stability of carbon-based buffer layers, such as Graphene and single wall carbon nanotubes showed excellent permeability.

Acknowledgments

After four years of continuous research on photovoltaics, the final stage of this project is approaching. Here, it gives me great opportunity to acknowledge those people who contributed to the unique atmosphere of the research group and the department which trained me at the beginning of my academic life.

First and foremost, I would like to offer my sincere thanks to my supervisor Prof. Ce Zhou Zhao. His research methodology and technical guidance are extremely helpful for me during the four year Ph.D. period. To me, Prof. Zhao is not only an academic supervisor, but also a mentor and a friend. Besides giving me guidance in research and advice on my career and future life, he influenced my life by his attitude towards work and living. I admire his devotion to science and work. Again, I would like to say it was a great privilege to work with him.

Also, I would like to express my gratitude to my supervisors and professors: Prof. Hongcai Wu, Prof. Jeremy Smith, Dr. Jinling Zhang, and Dr. Li Yang. They have encouraged me to explore the new scientific world and extend research to two-dimensional materials. They have offered help and support by all means. Their efforts are highly appreciated.

I am deeply grateful to Prof. EngGee Lim, Prof. Moncef Tayahi, Dr. Gang Liu, Dr. Sang Lam, and Prof. Ka Lok Man. During these years, they have given me help,

advices and support towards my academic career, and work. They are one of the reasons that I have lived a happy life here.

Many thanks to my comrades: Dr. Chun Zhao, Mr. Yifei Mu, Mr. Qifeng Lu, Ms. Yinchao Zhao, Mr. Chenguang Liu, Ms. Chufan Tang, and Mr. Ferryanto Ang. Your help, encouragement and company have filled my life with happiness and laughter. I wish everything goes well with your Ph.D., Master or career at Liverpool, Queensland or Indonesia. Also, I would like to thank my colleagues, Dr. Shi Cheng, Dr. Jie Ren, Dr. Jimin Xiao, and Dr. Jieming Ma. Wish you every success in your further life.

Special thanks to my family for their love and motivation. My parents and my sister are those who have provided me with a relaxed working environment, faith, and support throughout the years. They deserve the highest praise. Also, I own heartiest gratitude to my fiancée, who always accompanies me, encourages me, and motivates me. She is the treasure that life brings to me.

Jingjin Wu

Sept. 2015

List of Publications

JOURNAL ARTICLES

[1] **Jingjin Wu**, Yinchao Zhao, Ce Zhou Zhao, Jeremy Smith, Recent Progress in Materials for CdTe Thin Film Solar Cells applications, *Materials*, under major revision.

[2] **Jingjin Wu**, Yinchao Zhao, Ce Zhou Zhao, Li Yang, Qifeng Lu, Qian Zhang, Jeremy Smith, Yongming Zhao, Effects of Rapid Thermal Annealing on Structural Electrical and Optical Properties of Zr-Doped ZnO Thin Films Grown by Atomic Layer Deposition, *Materials*, Submitted.

[3] **Jingjin Wu**, Yinchao Zhao, Chenguang Liu, Li Yang, Jeremy Smith, Yongming Zhao, Structural, Optical and Electrical Properties of Atomic Layer Deposition derived Zr-doped ZnO and Hf-doped ZnO films, *Nanoscale Research Letters*, Submitted.

[4] Qifeng Lu, Yifei Mu, Joseph W. Roberts, Mohammed Althobaiti, Vinod R. Dhanak, **Jingjin Wu**, Chun Zhao, Ce Zhou Zhao, Qian Zhang, Li Yang, Ivona Z. Mitrovic, Stephen Taylor and Paul R. Chalker, Electrical Properties and Interfacial Studies of $Hf_xTi_{1-x}O2$ High Permittivity Gate Insulators Deposited on Germanium Substrate, *Materials*, **2015**, *8(12)*, 8169-8182.

[5] Qiuyu Chen, **Jingjin Wu**, Zhou Fang, Ce Zhou Zhao, The Design and Simulation of p-type Si/SiGe Terahertz Quantum Cascade Lasers, *Optics & Laser Technology*, **2014**, *57*, 104-109.

CONFERENCE PROCEEDINGS

[1] **Jingjin Wu**, Ce Zhou Zhao, Jeremy Smith, Technology Challenge of Substrate Configurations in CdTe Thin Film Solar Cells, In *2nd International Symposium on Energy Challenges and Mechanics (ECM)*, August 19-21, **2014**, Aberdeen, United Kingdom **(Invited Talk)**

[2] **Jingjin Wu**, Ferryanto Ang, Ce Zhou Zhao, Jeremy Smith, Electrical Properties of N-type CdS and P-type CdTe Thin Films in CdS/CdTe Solar Cells, In *20th International Symposium on the Physical and Failure Analysis of Integrated Circuits (IPFA)*, July 15-19, **2013**, Suzhou, China

[3] **Jingjin Wu**, Hongcai Wu, Ce Zhou Zhao, CdTe Solar Cells on Flexible Metallic Substrates, In *2012 International Conference on Advanced Engineering Materials and Technology (ICAEMT)*, July 6-8, **2012**, Zhuhai, China

[4] **Jingjin Wu**, Hongcai Wu, Ce Zhou Zhao, Low Cost Anti-reflection Coating for Photovoltaic Application, *2012 International Conference on Advanced Engineering Materials and Technology (ICAEMT)*, July 6-8, **2012**, Zhuhai, China

PATENTS

[1] **Jingjin Wu**, Ce Zhou Zhao, Chenguang Liu, A PN junction transient capacitance measurement system, Patent No.: 201520179615.5

[2] **Jingjin Wu**, Ce Zhou Zhao, Yinchao Zhao, A graphene-based flexible CdTe thin film solar cells, Patent No.: 201520181122.5

[3] **Jingjin Wu**, Ce Zhou Zhao, Yinchao Zhao, A graphene/metal nanowire/graphene sandwich structure flexible transparent conduction thin film, Patent No.: 201520154437.0

[4] **Jingjin Wu**, Ce Zhou Zhao, Chenguang Liu, A semiconductor device transient capacitance measurement system, Patent No.: 201520179612.1

[5] **Jingjin Wu**, Ce Zhou Zhao, A method for Cu_xTe nanomaterial synthesis, Patent Application No.: 201510050155.0

[6] **Jingjin Wu**, Ce Zhou Zhao, Chenguang Liu, A PN junction transient capacitance measurement method and its system, Patent Application No.: 201510139962.X

[7] **Jingjin Wu**, Ce Zhou Zhao, Yinchao Zhao, A graphene-based flexible CdTe thin film solar cells and its fabrication method, Patent Application No.: 201510140153.0

[8] **Jingjin Wu**, Ce Zhou Zhao, Yinchao Zhao, A graphene/metal nanowire/graphene sandwich structure flexible transparent conduction thin film and its fabrication method, Patent Application No.: 201510118778.7

[9] **Jingjin Wu**, Yifei Mu, Ce Zhou Zhao, Chufan Tang, A method to grow high-K dielectric layer on Graphene by Atomic Layer Deposition, Patent Application No.: 201510210826.5

[10] **Jingjin Wu**, Ce Zhou Zhao, Chenguang Liu, A semiconductor device transient capacitance measurement method and its system, Patent Application No.: 201510140554.6

[11] **Jingjin Wu**, Ce Zhou Zhao, Yinchao Zhao, Fluorinated graphene as a high resistivity layer replacement, In application processing

[12] **Jingjin Wu**, Ce Zhou Zhao, Yinchao Zhao, Boron doped Graphene as copper diffusion barrier, In application processing

[13] **Jingjin Wu**, Chenguang Liu, Chufan Tang, Jun Liu, Ce Zhou Zhao, A condensed CdS thin film deposition method and its system, In application processing

[14] **Jingjin Wu**, Chenguang Liu, Chufan Tang, Jun Liu, Ce Zhou Zhao, A low cost wireless temperature sensor for vacuum and high working temperature application, In application processing

[15] Ferryanto Ang, **Jingjin Wu**, Ce Zhou Zhao, A powder deposit system for CdTe thin film solar cells fabrication, Patent No.: 201310172608.8

[16] Ferryanto Ang, **Jingjin Wu**, Ce Zhou Zhao, A powder deposit method for CdTe thin film solar cells fabrication, Patent No.: 201320254418.6

[17] Qifeng Lu, **Jingjin Wu**, Ce Zhou Zhao, A Germanium interface passivation method for ALD deposited high-K material/Germanium substrate MOS device, In application processing

List of Figures

List of Tables

List of Acronyms

Term	Initial components of the term
AFM	Atomic Force Microscopy
ALD	Atomic Layer Deposition
a-Si:H	Hydrogenated Amorphous Silicon
CBD	Chemical Bath Deposition
CdS	Cadmium Sulfide
CdTe	Cadmium Telluride
CIGS	Copper Indium Gallium Diselenide
CM-AFM	Contact Mode-AFM
c-Si	Crystalline Silicon
CSS	Closed-space Sublimation
CVD	Chemical Vapor Deposition
DI water	Deionized Water
EDS	Energy Dispersive X-ray Spectroscopy
FF	Fill Factor
FWHM	Full Width at Half Maximum
GaAs	Gallium Arsenide
HIT	Heterojunction with Intrinsic Thin Layer
HRT	High Resistive Thin Layer
HVTE	High Vacuum Thermal Evaporation
LPCVD	Low-pressure Chemical Vapor Deposition

mc-Si	Multicrystalline Silicon
MJ	Multijunction
PSPD	Position Sensitive Photo Detector
PV	Photovoltaics
SEM	Scanning Electron Microscope
TM-AFM	Tapping Mode-AFM
TCO	Transparent Conducting Oxide
XRD	X-ray Diffraction

Table of Contents

Chapter 1: Introduction

1.1 Overview of Photovoltaics

Recently, solar photovoltaics (PV) market is undergoing a swift expansion. As reported, the grid-connected PV capacity grew to 139 giga peak watt (GWp) in 2014, 106 times larger than the PV capacity in 2000. Despite the rapid and unrelenting growth, PV power contributes only 0.87% of global electricity production in 2013 [1]. To meet the globally recognized climate change target in 2050, the fraction of renewable energy should be increased by several orders of magnitude.

In this scenario, renewable energy should meet 15% of global baseline demand (around 33 000 TWh by mid-century). Based on this assumption, the fraction of PV capacity can be calculated. It is estimated that 50% renewable energy fraction requires 12.5 TWp PV deployment. Such an ambitious target requires improving solar cells efficiency, manufacturing and materials availability.

Nowadays, there are several PV technologies ranking scheme. One of the most popular ranking schemes is the generation-based classification. Another classification method divides the solar cells into two categories: wafer-based and thin-film cells shown in Fig.1-1.

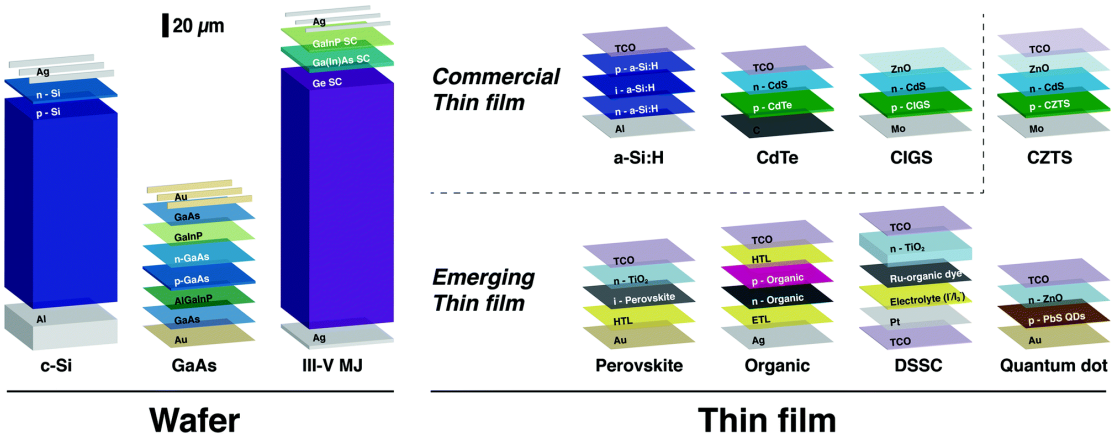

Fig. 1-1 Typical solar PV device structures, divided into wafer-based and thin-film technologies. *Reproduced from ref. [2]*.

The wafer-based cells technologies are the most mature of all PV technologies. Due to the mature silicon semiconductor industry and material abundance, crystalline silicon solar cells are the most popular in the market. They share ~90% of the current global production capacity in 2014. At the very beginning of PV history, crystalline silicon (c-Si) solar cells dominated the market. Later on, multicrystalline silicon (mc-Si) solar cells replaced them and constituted ~55% in 2014. Silicon-based solar cells are fabricated by doping the silicon wafer prior to slicing c-Si ingot or mc-Si block into 150-180 μm wafers. Record cell of c-Si cells is the variant heterojunction cell with intrinsic thin layer (HIT) architecture first announced by Panasonic. The HIT cell holds an efficiency of 25.6% [3]. For mc-Si cells, the best cell made by Trina Solar stands at 20.8% [4]. Although silicon-based solar cells show relatively high efficiencies, technologists are concerned with the high material usage of the technique for terawatt-scale application. Other challenges of the technique are the purity requirements and their low throughput.

Gallium arsenide (GaAs) is an ideal material for solar electricity conversion

application. It has a large absorption coefficient, matching energy band gap, and low non-radiative energy loss. Up until now, GaAs solar cells fabricated by Alta Devices are the best-reported lab cell with efficiency of 28.8% [5]. However, the main challenge is the high cost of such material.

Multijunction (MJ) solar cells are developed for matching the solar spectrum with different bandgap to absorb most of energy in sunlight. Record cell efficiency of 38.8% without concentration was announced by Spectrolab [6]. The barriers for large-scale deployment are complex manufacturing processes and low reservation of the materials involved.

Thin film cells provide another approach for terawatt-scale deployment. Thin film cells, with high light absorption coefficient materials allow the use of ultrathin film. A few micron thick absorber film significantly reduces material usage. Furthermore, thin film cells are believed to be the high energy density cell. Energy payback time suggests that CdTe cells are the best in the commercial PV cells, three times better than c-Si cells. The energy payback time can be translated into greenhouse gas emission during production and use. It demonstrates that the greenhouse gas emission are 5 g CO_2-eq per kWh for c-Si, compared to 21, 27, and 14 g CO_2-eq per kWh for a-Si:H, CIGS, and CdTe, respectively [2].

There are eight types of thin film solar cells. Three of them, including hydrogenated amorphous silicon solar cells, copper indium gallium diselenide solar cells, and cadmium telluride solar cells, are commercially available. Hydrogenated amorphous silicon (a-Si:H) solar cell is one of the crucial thin film solar cells. In

generally, a-Si:H thin film acts as an absorber in solar cells. 300 nm a-Si:H film is sufficient for ~90% above-bandgap photons, much lower than that of silicon absorber. Along with the abundance of silicon resource, a-Si:H solar cells became one of the popular solar cells. In 2013, a-Si:H solar cells held 2% of global PV market (22% of thin film PV market). However, the serious light-induced degradation (the Staebler–Wronski effect) imposed a constraint to their further development.

Copper Indium Gallium Diselenide (CIGS) solar cells are another well-known PV technology. CIGS solar cells have comparably high efficiency as silicon-based solar cells. Record CIGS solar cells had achieved 21.0% by Solibro [7]. The difficulty of such a quaternary material based technology lies in the control of the thin film stoichiometry. The variability of thin film significantly changes the properties of the absorber. Although CIGS cells have a place in PV industry (2% of PV market, 22% of thin film PV market), based on Fig 1-2, the scarcity of indium and selenium is a hinder in the future for terawatt-scale application.

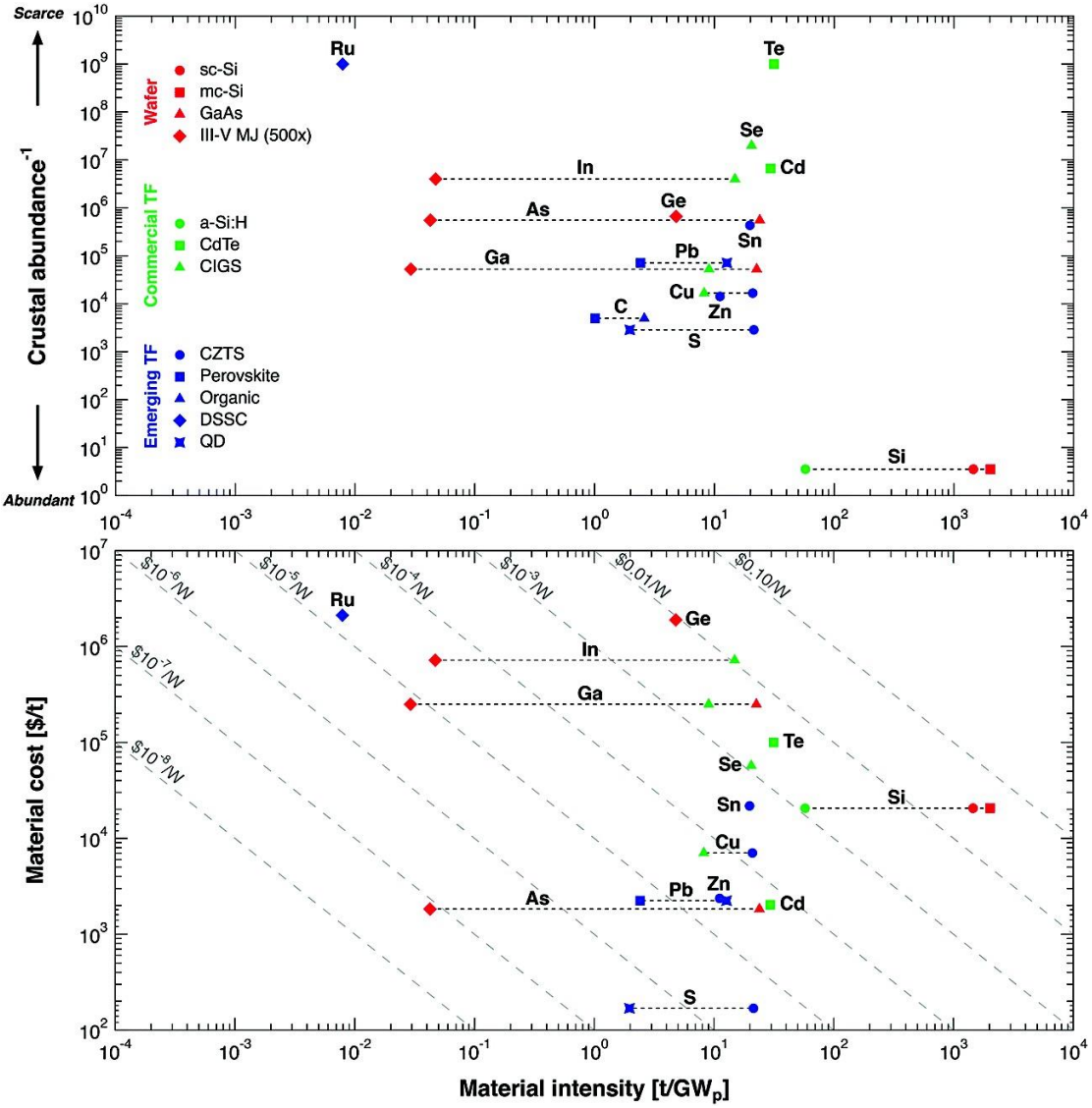

Fig. 1-2 Materials usage, abundance, and cost for key elements used in commercial and emerging PV technologies. *Reproduced from ref. [2]*.

Cadmium telluride (CdTe) solar cells are a leading thin-film PV technology. Record efficiency has been broken several times during these years. CdTe technology employs roll-to-roll deposition processes with high-throughput. This technique is believed to offer the lowest module cost of any PV technology in the market. In 2014, First Solar claimed to have improved the efficiency to 21.0% for stand alone solar cells and 17.5% for modules [2]. Hence, we foresee the PV market share of CdTe will be greater than that of 5% in the future.

1.2 CdS/CdTe Thin Film Solar Cells Current Status

CdTe solar cells technology occupies the second place in the photovoltaic market behind silicon-based device technology. The competitiveness of CdTe solar cells will further be improved as the increase of understanding of CdTe cells mechanism and the decrease of manufacturing cost.

According to the manufacturing sequences, leading thin film technology can be classified into two categories: substrate and superstrate configurations. Substrate configuration in the other hand uses metal foil as a substrate, then, CdTe is deposited as an absorber layer, later cadmium sulfide (CdS) window layer and transparent conductive oxide (TCO) is deposited as contact. The superstrate configuration is an inverted structure of the conventional substrate structure. In this approach, a TCO coated transparent glass is used as a substrate on which deposit window layer, absorber, and back contact accordingly [8].

After more than 40 years intensively studied, the efficiency of CdTe solar cells has reached a relatively high value. In substrate configuration; a conversion efficiency of up to 13.6% has been reported [9]. However, the recorded efficiency of the superstrate configuration CdTe solar cells reached 20.0%. The difference arises from the fact that CdTe has a relatively high electron affinity. Substrate configuration limits the device processing, which imposes restriction on the formation of ohmic contact at the back surface field. Moreover, the diffusion of impurities from the buffer layer and the metal substrate to the junction further destroys the solar cell. Hence, superstrate configuration CdTe cells are widely used in industry, even though the metal substrate

in substrate configuration can be thin and hence light weight, and the substrate configuration devices have a significant price reduction potential.

To further improve the competitiveness of superstrate CdTe solar cells, the ongoing research focuses on two aspects: improvement of the solar cell quality and reduction of the manufacturing cost. For the former, research concentrates on improving junction activation, solar cells efficiency and stability. For the latter, researchers interest in tuning the CdS/CdTe thin film thickness and replacing ITO with cheaper transparent conductors. Moreover, they search new materials that serve as buffer layer at the back surface field to avoid Schottky diode formation at the back contact electrode.

In this thesis, we focus on three aspects: (a) strategies being developed to fabricate a suitable front contact; (b) the effect of the chlorine activation process and the post-treatment; and (c) suitable buffer layers, such as Cu_xTe, Sb_2Te_3, MoO_3 to form the ohmic contact at the back electrode.

1.2.1 Front Contact Fabrication

The front contact film is a thin film that covers CdS window layer and serves as a front electrode of the solar cell. Therefore, materials that can be used as a front contact should have high transparency to allow more than 85% visible light penetrating into the CdTe solar cells over its working wavelength (400-860 nm). The materials should have relatively low resistivity on the order of 2×10^{-3} Ω·cm to reduce the series resistance of the device. The materials are also required to withstand high

fabrication temperature in the final deposition procedures in superstrate configuration devices shown in Table 1-1 are some popular materials listed as transparent conducting oxide.

Table 1-1 Properties of popular Transparent Conducting Oxide (TCO) materials. *Reproduced from ref. [10]*.

Material	Resistivity (Ω·cm)	Transparency (%)
SnO_2:F (FTO)	8×10^{-4}	80
In_2O_3:Sn (ITO)	2×10^{-4}	80
In_2O_3:Ga	2×10^{-4}	85
In_2O_3:F	2.5×10^{-4}	85
Cd_2SnO_4 (CTO)	2×10^{-4}	85
Zn_2SnO_4 (ZTO)	10^{-2}	90
ZnO: In	8×10^{-4}	85

The most commonly used TCOs for CdTe solar cells are SnO_2:Sn (ITO), SnO_2:F (FTO) and Zn:Al (AZO). Instead of using one layer, they are often used in combination with a High Resistive and Transparent (HRT) layer. HRT layers are usually 50 nm thick and made by SnO_2, ZnO, or Zn_2SnO_4. The TCO and HRT bi-layer act as barrier to passivate the diffusion of sodium ions from the soda-lime glass. In addition, an HRT film may act as an "etch-stop" in the acid treated CdTe thin film process to prevent possible shunts from the over-etched CdTe films. Therefore, the use of TCO and HRT bi-layer facilitates the possibility of using thinner CdS film.

1.2.1.1 ZnO:Al Thin Films as Front Contact for CdTe Solar Cells

Conventional TCO materials are SnO_2:F (FTO), SnO_2:In (ITO) and SnO_2:Cd (CTO). Recently, ZnO-based TCO films have attracted significant attention due to their untoxic characteristic and low cost potentials. Gupta and Compaan used ZnO:Al as a TCO layer in the all-sputtered CdTe solar cells and obtained a device with 14.0% efficiency [11]. Mazzamuto also reported an ZnO:Al-based solar cell with an efficiency of 14.0%, higher than the SnO_2:F-based solar cells; it is shown in Table 1-2 [12].

Table 1-2 CdS/CdTe devices using SnO2:F (FTO) and ZnO:Al, respectively. *Reproduced from ref. [12]*.

TCO	V_{oc} (mV)	J_{sc} (mA·cm^{-2})	FF (%)	η (%)	R_s (Ω·cm^2)	R_{sh} (Ω·cm^2)
SnO_2:F	820	20.7	73.96	12.6	3.9	1822
ZnO:Al	814	23.6	73.25	14.0	3.16	989

The ZnO:Al film shows better transparency in the visible spectrum (<900 nm) based on Fig. 1-3. It also shows higher electron mobility and lower sheet resistance, compared to the FTO film.

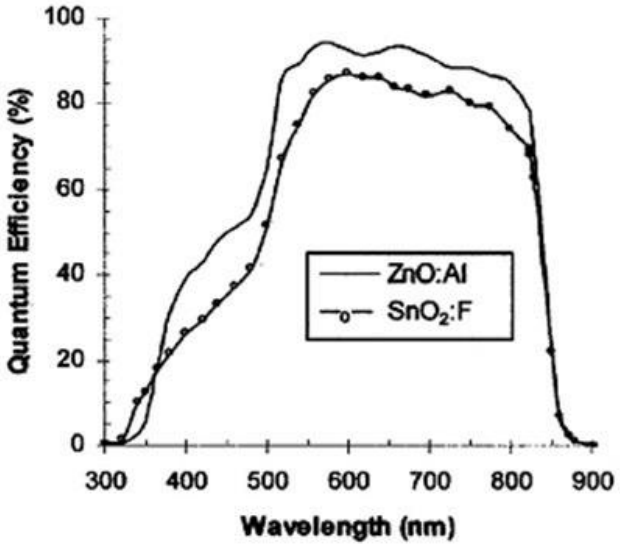

Fig. 1-3 Quantum Efficiency curves of CdS/CdTe solar cells using ZnO:Al and SnO2:F as front contact. *Reproduced from ref. [11]*.

Another advantage is the diffusion of Zn into CdS layer during chlorine treatment, which may tune the energy bandgap and transmittance of the CdS layer [13].

1.2.1.2 Transparent Conducting Graphene Films

ZnO:Al is believed to be a superior front contact material. However, ion diffusion from the ZnO:Al film to junction region during deposition process or illumination leads to cells deterioration. Therefore, a substitution is required.

Graphene film would be quite encouraging due to their high electron mobility and high optical transparency. Large scale and high quality grapheme films can be prepared by chemical vapor deposition (CVD). Graphene films show higher optical transparency in all wavelength regions, from 350 to 2200 nm. Also, the mobility is much higher than that of conventional TCOs as shown in Table 1-3 [14]. The high

sheet resistance of graphene could reduce from 125 Ω sq^{-1} to 30 Ω sq^{-1} by doping [15].

With such superior properties, graphene films have been used as a front electrode. Wang et al. used graphene as a front electrode of a dye sensitive cells (DSC) cell and obtained a low efficiency of 0.26% [16]. Hui Bi et al. have also successfully fabricated a CdTe solar cell with an efficiency of 4.17% in a glass/graphene/ZnO/CdS/CdTe/graphite configuration [14].

Table 1-3 Average transmittance (Tr), sheet resistance (Rs), and carrier mobility (μ) of the TCO films, including CVD graphene (GR), mechanically exfoliated graphene (ME GR), SnO2:In (ITO), ZnO:Al, and FTO. *Reproduced from ref. [14]*.

Transparent Conducting Film	**Thickness**	**Tr (%) (350-900nm)**	**Rs (Ω sq^{-1})**	**μ ($cm^2 V^{-1}s^{-1}$)**
GR	1 layer	95.5	1150	602.4
GR	2 layers	92.8	780	578.3
GR	4 layers	88.7	445	550.0
GR	7 layers	82.2	220	450.8
ITO	700nm, 300nm	81.7, 80.1	24.7, 20.0	23.2, 19.0
AZO	600nm, 718nm	81.6, 80.9	15.9, 7.5	18.7, 24.0
FTO	420nm	84.1	25.8	20.0
GR (Ni)	1-12 layers	89.7	1000	100-2000
GR (Cu)	4 layers	90.4	350	-
GR (Cu)	1 layer	97.4	272	5100
ME GR	1 layer	97.6	-	10000

1.2.2 Activation Processes

Activation processes are another important research topic since they are necessary to improve the thin film and the junction qualities.

1.2.2.1 Oxygen Assisted CdTe Growth

Oxygen is believed to have significant effects on controlling CdTe grain size, doping concentration enhancement, and GBs passivation [17]. Oxygen plays a crucial role in CdTe grain growth [18]. It is shown that an increasing in oxygen partial pressure leads to an increasing nucleation site density. Therefore, CdTe layers that are grown under higher oxygen partial pressure ambient will generate small but compact grains. The dense CdTe grain structure will further suppress the shunting problem of the device. On the contrary, CdTe thin films grown without O_2 shows large grain size. It is relatively easy to form voids or pinholes between large grains. The voids and pinholes may further increase the possibility of shunting problem [17].

Oxygen could enhance the p-type doping in the CdTe layer. Valdna et al. have demonstrated that a small amount of oxygen during deposition process led to a decrease in film resistivity [19]. The presence of oxygen in the closed-space sublimation (CSS)-related CdTe deposition facilitate the hole concentration up to 3.4×10^{14} cm^3. Higher doping concentration leads to an increase of V_{oc}. However, the net carrier concentration in CdTe films saturates at 3.4×10^{14} cm^3. High oxygen partial pressure results in the oxidation of Cadmium, and consequently increases the resistivity by six orders of magnitude [19].

The presence of oxygen could improve the junction quality. Albin et al. advocated that oxygen slow down the reaction between Te and Cd atoms, which reduces the inter-diffusion of CdS and CdTe leading to an improvement in junction quality [17]. Flores et al. demonstrated that an oxygen involved annealing improved the property of chemical bath deposition grew CdS (CBD-CdS), the efficiency of the oxygen-treated solar cell increased to 6.6%, compared to the as-deposited solar cells with an efficiency of 5.4% [20]. The device efficiency was further improved to 9.8% by removing the oxidation on the surface of the CdS film [17].

1.2.2.2 $CdCl_2$ Treatment

It is hypothesized that Chloride ion acts as a fluxing agent that enhances the atom mobility of CdTe film during the annealing process [21]. $CdCl_2$ was commonly used in the post-deposition treatment of CdTe solar cell. The CdTe – $CdCl_2$ phase diagram indicates that the eutectic temperature of CdTe – $CdCl_2$ is around 490 ℃. $CdCl_2$ will vaporize and may not influence the grain growth at higher annealing temperatures [22]. Hence, the temperatures chosen in $CdCl_2$ treatment are mostly lower than 490 ℃.

$CdCl_2$ was mostly deposited on the device by two methods, including dry method and wet method [23, 24]. The chloride vapor treatment method was also reported [25, 26].

$CdCl_2$ dry deposition method is a vacuum evaporation technology. A few nm thick $CdCl_2$ was evaporated on the CdTe surface prior to post-annealing, in which

vacuum evaporation is a high cost and time-consuming technology. Wet $CdCl_2$ deposition provides an easy handling method. Therefore, the wet deposition method is used in most of the research institutes. In wet deposition, CdTe film was initially dipped into the saturated $CdCl_2$ – CH_3OH solution [27]. The sample was dried to precipitate a $CdCl_2$ film followed by annealing in the presence of oxygen or inert air atmosphere at <490 ℃ for around half an hour [18]. After heat treatment, residual $CdCl_2$ on the sample surface is washed with distilled water. However, the wet $CdCl_2$ treatment method fails for large area solar cells fabrication. The humid environment of the treatment process may further lead to device degradation. The vaporized $CdCl_2$ treatment method was reported to effectively eliminate the rinsate on the sample surface with better reproducibility [25].

In summary, oxygen/chloride co-processing enhances the junction formation and eliminates lateral shunt path of the device. However, O and Cl co-doping needs further understanding.

1.2.3 Back Contact Buffer Layer

The electron affinity of p-type CdTe is high. Since most metals do not have a relatively high work function, it forms a Schottky junction with the back electrode. Thereby, back contact technique is one of the challenges in the manufacture of CdTe solar cells.

Generally, people introduce superstrate configuration to overcome the problem. In the superstrate configuration, a CdTe layer is etched with nitric-phosphoric solution

or bromine-methanol solution. After a few seconds of treatment, the etched CdTe surface forms a thin p+ region. The p+ region acts as a heavily doped p-type semiconductor in-between the CdTe film and metal electrode, which facilitates the carrier transportation through tunneling effect. Other materials can also be used as a back contact buffer layer. Popular materials include graphite: Cu [28], Te [29-31], Au, Cu_xTe [32-34], ZnTe [35], HgTe, Sb_2Te_3 [36], As_2Te_3, and MoO_x [37, 38]. Such materials can help overcome the potential barrier and improve the cell efficiency.

For devices in the substrate configuration, the CdTe layer is deposited on the metal electrode at the very first step. The deposition sequence brings difficulties to the acid-etching process. In order to form an ohmic contact between the back electrode and CdTe layer, a heavily doped semiconductor buffer layer should be introduced. It should be noted that the buffer layer must be stable and capable of withstanding high temperatures during the subsequent manufacturing and heat treatment steps. Popular buffer layers are listed in Table 1-4 [39].

Table 1-4 Parameters of solar cells (substrate configuration) with different buffer layers. *Reproduced from ref. [39]*.

Buffer layer	**η(%)**	**V_{oc} (mv)**	**FF (%)**	**J_{sc} (mA/cm^2)**
MoO_3/Te	10.0	733	62.3	22.0
Sb_2Te_3	8.6	658	61.2	21.4
MoO_3	5.9	597	48.4	20.3
Sb	4.6	446	49.6	21.1
Cu/Te/MoO_3	11.3	768	68.6	21.4
Cu	8.9	751	61.2	20.0

Cu/Sb_2Te_3	7.7	622	58.2	21.2
CuO_x	7.5	690	49.2	22.0
Cu/Sb	6.1	658	51.3	18.3

1.2.3.1 Material with high stability: Sb_2Te_3

With the matched thermal expansion coefficient of CdTe, Mo has been chosen as the back electrode. However, the difference in the work function between the absorber and Mo results in a non-rectifying junction. Two approaches have been used to form a quasi-ohmic contact. One method is to place a layer with the required high work function materials to reduce the barrier height. By applying such layer, the holes can overcome the barrier and reach the back electrode at its operating temperature. Another approach is to introduce a heavily doped layer to narrow the barrier width. Using this approach, holes can reach the back electrode by tunneling effect. Using this approach, materials such as Cu_xTe and Sb_2Te_3 have attracted the most attention.

Remeo et al. first introduced Sb_2Te_3 into superstrate configurations CdS/CdTe thin film solar cells [40]. With a Sb_2Te_3 /Mo back contact, the solar cell showed 14.6% efficiency with a 74% fill factor (FF). Subsequently, extensive research was applied to Sb_2Te_3. The research revealed that the degenerate p-type Sb_2Te_3 has a very low resistivity, on the order of 10^{-4} Ω·cm. The work function of the p-type Sb_2Te_3 can be tuned between 5.12-5.8 eV, which matches well with CdTe [41]. It is also reported that $CdTe/Sb_2Te_3$ is in thermodynamic equilibrium and no reaction occurs between them from a chemical point of view [42]. Moreover, a small amount of Sb diffuses into the CdTe, forms a thin p^+ CdTe layer, which further facilitates the formation of a

quasi-ohmic contact [40].

The Sb doping effect and dopant compensation mechanism in the CdS/CdTe solar cell still do not fully be understood at the moment. However, it is believed that Sb substitutes for Cd atoms and forms Sb_{cd}^{+} donors when it diffuses into the Te-rich area. On the contrary, Sb_{Te}^{-} acceptors form at the Cd-rich limit [41]. The Sb_{cd}^{+} donors in the p-CdTe layer have several positive effects. Since most Sb ions diffuse through grain boundaries, Sb_{cd}^{+} donors accumulate at the boundaries. As positive particles, they repulse the holes from the grain bulk towards the back contact and the electrons are pulled to the grain boundaries and transport to the depletion region [41]. By this means, Sb_{cd}^{+} donors promote the separation of electron-hole pairs and greatly reduce the recombination in the grain boundaries. On the other hand, the Sb_{cd}^{+} donors compensate V_{Cd}, the missing Cd atoms at the lattice site, which leading to a higher Fermi level in the device.

In the meantime, Sb_2Te_3 acts as an impurities barrier at the back contact [36]. The diffused impurities accumulate at the CdS/CdTe junction and form Generation-Recombination centers. As the impurities accumulate at the grain boundaries, voids and interfaces, they change the shunts. All this reveals that the diffused impurities lead to device degradation.

In thin film solar cells, most of the impurities come from the sodium in the glass substrate and metal elements in the back contact buffer. It is necessary to deposit an thin film on the substrate acting as substrate ion impurities barrier. In the superstrate configuration, a transparent layer such as Al_2O_3, SiO_2, or ITO is deposited

on the glass substrate prior to solar cell deposition. In the substrate configuration case, impurities come from the metal foil substrate. The back contact buffer is also expected to act as a passivation layer. As fast diffusers like Cu and Al degrade solar cells over a short period, it is essential to find a metal electrode with a low diffusion coefficient and a buffer material with high ion diffusion barrier.

Molybdenum is a material that has low diffusion velocity. In addition, Mo foil can be prepared with a high purity. Therefore, Sb_2Te_3/Mo is expected to be a stable back contact for long term operation [43]. An aging test had been applied to CdTe solar cells with a Sb_2Te_3/Mo stack. After 5 months of testing, the performance of the device changed with no decrease, but increased of 10%. The explanation for this is that the light soaking effect facilitated a better back contact. The aging test carried on for 9 months, with the efficiency declining slightly but still higher than the initial efficiency by 4%. In contrast, solar cells with a Sb/Mo stack show severe degradation [44]. A Sb_2Te_3/Mo stack forms a successful Cu-free back contact. However, the stability and resistivity of Sb_2Te_3 depend on the manufacturing conditions. Also, the dopant compensation effect of telluride affects the doping step [45].

1.2.3.2 The novel high work function material: MoO_x

Most of the back contact buffers lie in a heavily doped semiconductor to narrow the Schottky barrier, which facilitates hole transportation by the tunneling effect. Another approach is to use materials with a high work function to reduce the barrier height, hence enhancing hole transportation. One of such material is MoO_x. MoO_x has

a high work function of (Φ_s=5.3–6.8 eV) [38]; yet, its working mechanism has not been fully revealed. It is understood that its high work function contributes to promoting the work function of the electrode and therefore lowering the level of the Schottky barrier [46]. Gao et al. [47] and Huang [48] believe that the presence of defect states in the band gap may align the semiconductor valence band and serve as a hole transport pathway.

This novel material attracts worldwide attention. Lin [49] grew CdTe solar cells on FTO coated soda lime glass with a MoO_x/Ni stack back contact. The solar cell exhibits an efficiency of 12.2% with a open circuit voltage of 816mV. The J-V behavior showed that the roll-over phenomenon was eliminated. Despite a proper thickness of MoO_x film contributing to the forming of quasi-ohmic contact with CdTe, precise control of the process condition is another challenge for this technique.

The properties of MoO_x film are strongly dependent on the deposition methods [50-53]. A MoO_x layer prepared by thermal evaporation produces a transparent layer of stoichiometric composition to form quasi-ohmic contact accompanied by a p-CdTe and metal electrode. The solar cells demonstrated the normal J-V characteristics and an excellent FF. However, a sputtering deposited MoO_x layer exhibit poor J-V characteristics. A roll-over phenomenon could be observed. Also, the composition of the sputtering prepared layer changed as Mo^{6+} and Mo^{5+} ions were found in such films [54].

The thickness of the MoO_x layer should be carefully controlled, since MoO_x is an insulating material [49]. Lin reported that a MoO_x layer of 40 nm results in a

normal J-V characteristic, whilst a buffer layer with excess MoO_x of 80nm introduces an additional series resistor [49].

The residual rinsing step is crucial to superstrate configuration, as the residual layer may compensate for the work function of MoO_x, which leads to higher Schottky barrier. Experiments demonstrated that CdTe films with and without the rinsing procedure prior to MoO_x/Ni stack deposition showed 71.4% and 47.4% FF, respectively [54]. For substrate configuration, the MoO_x layer is deposited prior to the CdTe film. Therefore, the metal foil should be rinsed to remove the oxides, organic, and other impurities.

The metal electrode affects the stability of the MoO_x layer. Lin [54] coated various metals like Ni, Mo, Cr, Al and Mg on the CdTe solar cells as the back electrode. The efficiencies of different cells are similar. However, aging test showed that cells with Cr and Al electrodes were less stable. The reason is that Cr and Al tend to form oxides, as their standard enthalpy of oxide formation is larger than that of Mo. In contact with such metals, oxygen in MoO_x is extracted and forms metal oxides. In contrast, metals with lower standard enthalpy formation of their oxides like Mo and Ni are expected to be stable [55].

Another problem is MoO_x sensitivity to air exposure [55]. This brings complexity in the MoO_x layer deposition, and makes vacuum evaporate deposition preferential.

1.3 Objectives of Thesis

In silicon-based solar cells, silver paste is sintered to form front gate wire electrode. However, transparent conduction oxide films are more popular than wire electrode in thin film solar cells. Since the recombination rate in the surface of thin film solar cells is extremely high, a large number of carriers will be recombined during lateral migration to the metal wire electrodes. Transparent conduction oxide electrode that covers the whole surface of thin film solar cells will enhance the carrier collection by avoiding lateral recombination. Transparent electrode requires high optical transparency (more than 80%) in the visible region and low resistivity (about 10^{-3} Ω cm) simultaneously. Thin metal films have fairly good conductivity, but the transparency is far from enough to satisfy the demand. The possible way to obtain eligible transparent conductors is to introducing dopants to wide band gap oxide (greater than 3eV). The degeneracy oxide thus shows good electrical conductivity. ITO is the most popular material among all the transparency oxides. ITO is commercially available with low sheet resistance and high transparency. However, small indium reserve is a potential threat to terawatt-scale photovoltaic application. One of the approaches to mitigate potential material scaling limit is employing alternatives that use abundant elements. AZO is one of such substitutes. However, scientists often target the cost reduction of AZO without regard to thermal stability issue. Since the fabrication of CdTe solar cells process involved high temperature process, transparent conductor that can withstand high temperature is required. In this thesis, Zirconium doped Zinc Oxide (ZnO:Zr) thin films will be deposited on quartz

glass by ALD. Then, the electrical, optical and structure properties of ZnO:Zr thin films were further investigated.

Another research challenge of CdTe solar cells is low doping concentration in absorber layer. Polycrystalline CdTe thin film involves high thermal process during thin film deposition and post-treatment. The high thermal environment favors the generation of V_{Cd}, giving rise to the p-type conductivity. It is reported that CdTe thin film reaches perfect stoichiometry at 400 ℃ [56]. At a temperature of 500-600 ℃, absorber layer has a carrier concentration of 10^{14} cm^{-3} [2]. The carrier concentration could slightly be increased after $CdCl_2$ post-treatment at ambient environment. Oxygen environment is considered to enhance the grain growth and p-doping [57]. In addition, few nanometer copper layers were deposited on the CdTe to increase the doping concentration and eliminate Schottky diode. But a large amount of copper ions lead to solar cell degradation. Therefore, it is necessary to investigate the solar cell degradation with Cu_xTe as back contact buffer layer. In chapter 4, researches focus on the effect of Cu_xTe.

Copper is the most commonly used material that acts as a dopant in CdTe layer. There are several copper states: interstitial ion Cu_{i+}, deep acceptor state Cu_{Cd}^{+}, (Cu_{Cd}^{-}-Cu_i^{+}) complex, and (Cu_i^{+}-V_{Cd}^{-}) complex. On one hand, copper ions will increase the carrier concentration; on the other hand, extra copper ions that migrate to the interface of CdS/CdTe result in serious cell degradation. It is demonstrated that the shallow donor, interstitial form of Cu, is a faster diffuser than Cu_{Cd}^{-} in the form of (Cu_i^{+}-V_{Cd}^{-}) complex [58-60]. Their distribution is progressively uniform and deeper

into the CdTe film. The deep acceptor Cu_{Cd}^{-}, however, is nonuniform and is strongly related to the back contact interface [61]. To fabricate a CdTe solar cell with high stability, the effects of conventional back contact materials, including Cu_xTe, MoO_3, is investigated by SCAPS. Later on, graphene is synthesized by low-pressure chemical vapor deposition, followed by solar cells stability simulation using graphene as buffer layer.

References for the Chapter

1. *Trends in Photovoltaic Applications*. 19th ed.; International Energy Agency Photovoltaic Power Systems Programme: 2014.
2. Jean, J.; Brown, P. R.; Jaffe, R. L.; Buonassisi, T.; Bulovic, V., Pathways for solar photovoltaics. *Energy & Environmental Science* **2015,** 8, (4), 1200-1219.
3. Masuko, K.; Shigematsu, M.; Hashiguchi, T.; Fujishima, D.; Kai, M.; Yoshimura, N.; Yamaguchi, T.; Ichihashi, Y.; Mishima, T.; Matsubara, N.; Yamanishi, T.; Takahama, T.; Taguchi, M.; Maruyama, E.; Okamoto, S., Achievement of More Than 25% Conversion Efficiency With Crystalline Silicon Heterojunction Solar Cell. *Ieee Journal of Photovoltaics* **2014,** 4, (6), 1433-1435.
4. Verlinden P, D. W., Zhang X, Yang Y, Xu J, Shu Y, Quan P, Sheng J, Zhang S, Bao J, Ping F, Zhang Y, Feng Z, Strategy, development and mass production of high-efficiency crystalline Si PV modules. In *6th World Conf. on PV Energy Conversion* Kyoto, 2014; Vol. Paper 4sMoO.1.4.
5. Kayes BM, N. H., Twist R, Spruytte SG, Reinhardt F, Kizilyalli IC, Higashi GS 27.6% conversion efficiency, a new record for single-junction solar cells under 1 sun illumination. In *Proceedings of the 37th IEEE Photovoltaic Specialists Conference*, 2011.
6. Chiu PT, L. D., Woo RL, Singer S, Hong WD, Zakaria A, Boisvert JC, Mesropian S, King RR, Karam NH, Continued progress on direct bonded 5J space and terrestrial cells. In *Proc. 40th IEEE PVSC* 2014.
7. Solibro beats world record for solar cells. Solibro Press 2014.
8. Kim, H.; Horwitz, J. S.; Kushto, G. P.; Kafafi, Z. H.; Chrisey, D. B., Indium tin oxide thin films grown on flexible plastic substrates by pulsed-laser deposition for organic light-emitting diodes. *Applied Physics Letters* **2001,** 79, (3), 284-286.
9. Kumar, S. G.; Rao, K. S. R. K., Physics and chemistry of CdTe/CdS thin film

heterojunction photovoltaic devices: fundamental and critical aspects. *Energy & Environmental Science* **2014,** 7, (1), 45-102.

10. Morales-Acevedo, A., Thin film CdS/CdTe solar cells: Research perspectives. *Solar Energy* **2006,** 80, (6), 675-681.
11. Gupta, A.; Compaan, A. D., All-sputtered 14% CdS/CdTe thin-film solar cell with ZnO : Al transparent conducting oxide. *Applied Physics Letters* **2004,** 85, (4), 684-686.
12. Mazzamuto, S.; Vaillant, L.; Bosio, A.; Romeo, N.; Armani, N.; Salviati, G., A study of the CdTe treatment with a Freon gas such as CHF2Cl. *Thin Solid Films* **2008,** 516, (20), 7079-7083.
13. Barrioz, V.; Irvine, S. J. C.; Jones, E. W.; Rowlands, R. L.; Lamb, D. A., In situ deposition of cadmium chloride films using MOCVD for CdTe solar cells. *Thin Solid Films* **2007,** 515, (15), 5808-5813.
14. Bi, H.; Huang, F. Q.; Liang, J.; Xie, X. M.; Jiang, M. H., Transparent Conductive Graphene Films Synthesized by Ambient Pressure Chemical Vapor Deposition Used as the Front Electrode of CdTe Solar Cells. *Advanced Materials* **2011,** 23, (28), 3202-+.
15. Bae, S.; Kim, H.; Lee, Y.; Xu, X.; Park, J.-S.; Zheng, Y.; Balakrishnan, J.; Lei, T.; Ri Kim, H.; Song, Y. I.; Kim, Y.-J.; Kim, K. S.; Ozyilmaz, B.; Ahn, J.-H.; Hong, B. H.; Iijima, S., Roll-to-roll production of 30-inch graphene films for transparent electrodes. *Nat Nano* **2010,** 5, (8), 574-578.
16. Wang, X.; Zhi, L.; Muellen, K., Transparent, conductive graphene electrodes for dye-sensitized solar cells. *Nano Letters* **2008,** 8, (1), 323-327.
17. Albin, D. S.; Yan, Y.; Al-Jassim, M. M., The effect of oxygen on interface microstructure evolution in the CdS/CdTe solar cells. *Progress in Photovoltaics* **2002,** 10, (5), 309-322.
18. Cruz, L. R.; Pinheiro, W. A.; Medeiro, R. A.; Ferreira, C. L.; Dhere, R. G.; Duenow, J. N., Influence of heat treatment and back contact processing on the performance of CdS/CdTe thin film solar cells produced in a CSS in-line system. *Vacuum* **2013,** 87, 45-49.

19. Valdna, V., Optoelectronic properties of chlorine- and oxygen-doped CdTe thin films. *Solar Energy Materials and Solar Cells* **2005,** 87, (1-4), 369-373.

20. Rios-Flores, A.; Pena, J. L.; Castro-Pena, V.; Ares, O.; Castro-Rodriguez, R.; Bosio, A., A study of vapor CdCl2 treatment by CSS in CdS/CdTe solar cells. *Solar Energy* **2010,** 84, (6), 1020-1026.

21. Dharmadasa, I., Review of the CdCl2 Treatment Used in CdS/CdTe Thin Film Solar Cell Development and New Evidence towards Improved Understanding. *Coatings* **2014,** 4, (2), 282.

22. Xu, B. L.; Rimmaudo, I.; Salavei, A.; Piccinelli, F.; Di Mare, S.; Menossi, D.; Bosio, A.; Romeo, N.; Romeo, A., CdCl2 activation treatment: A comprehensive study by monitoring the annealing temperature. *Thin Solid Films* **2015,** 582, 110-114.

23. Romeo, A.; Bätzner, D. L.; Zogg, H.; Tiwari, A. N., Recrystallization in CdTe/CdS. *Thin Solid Films* **2000,** 361–362, (0), 420-425.

24. Bai, Z.; Wang, D., Oxidation of CdTe thin film in air coated with and without a CdCl2 layer. *Physica Status Solidi a-Applications and Materials Science* **2012,** 209, (10), 1982-1987.

25. McCandless, B. E.; Hichri, H.; Hanket, G.; Birkmire, R. W.; Ieee, *Vapor phase treatment of CdTe/CdS thin films with CdCl2:O-2*. 1996; p 781-784.

26. Major, J. D.; Bowen, L.; Treharne, R. E.; Phillips, L. J.; Durose, K., NH4Cl alternative to the CdCl2 treatment step for CdTe thin-film solar cells. *IEEE Journal of Photovoltaics* **2015,** 5, (1), 386-389.

27. Gorji, N. E., Degradation sources of CdTe thin film PV: CdCl2 residue and shunting pinholes. *Applied Physics a-Materials Science & Processing* **2014,** 116, (3), 1347-1352.

28. Demtsu, S. H.; Albin, D. S.; Sites, J. R.; Metzger, W. K.; Duda, A., Cu-related recombination in CdS/CdTe solar cells. *Thin Solid Films* **2008,** 516, (8), 2251-2254.

29. Vigil, O.; Ochoa-Landin, R.; Fandino, J.; Cruz-Gandarilla, F., Comparative study of the p plus layer created in CdTe films by nitric-phosphoric etching

and chemical-deposition methods. *Journal of Physics and Chemistry of Solids* **2010,** 71, (3), 404-406.

30. Ochoa-Landin, R.; Vigil-Galan, O.; Vorobiev, Y. V.; Ramirez-Bon, R., Chemically-deposited Te layers improving the parameters of back contacts for CdTe solar cells. *Solar Energy* **2009,** 83, (1), 134-138.
31. Potlog, T.; Ghimpu, L.; Antoniuc, C., Comparative study of CdS/CdTe cells fabricated with and without evaporated Te-layer. *Thin Solid Films* **2007,** 515, (15), 5824-5827.
32. Park, Y.; Lee, S.; Yi, J.; Choi, B. D.; Kim, D.; Lee, J., Sputtered CdTe thin film solar cells with Cu2Te/Au back contact. *Thin Solid Films* **2013,** 546, 337-341.
33. Teeter, G., Cu2Te synthesis and in-vacuum thermal decomposition: Chemical-kinetics analysis and comparison to equilibrium vapor-pressure measurements. *Thin Solid Films* **2007,** 515, (20–21), 7886-7891.
34. Wu, X.; Zhou, J.; Duda, A.; Yan, Y.; Teeter, G.; Asher, S.; Metzger, W. K.; Demtsu, S.; Wei, S.-H.; Noufi, R., Phase control of CuxTe film and its effects on CdS/CdTe solar cell. *Thin Solid Films* **2007,** 515, (15), 5798-5803.
35. Späth, B.; Fritsche, J.; Säuberlich, F.; Klein, A.; Jaegermann, W., Studies of sputtered ZnTe films as interlayer for the CdTe thin film solar cell. *Thin Solid Films* **2005,** 480-481, 204-207.
36. Paudel, N. R.; Wieland, K. A.; Compaan, A. D., Characterization of rf sputtered Sb2Te3 thin films for back contacts to CdS/CdTe solar cells. *Journal of Materials Science-Materials in Electronics* **2015,** 26, (1), 78-83.
37. Kroeger, M.; Hamwi, S.; Meyer, J.; Riedl, T.; Kowalsky, W.; Kahn, A., Role of the deep-lying electronic states of MoO3 in the enhancement of hole-injection in organic thin films. *Applied Physics Letters* **2009,** 95, (12).
38. Irfan, I.; Ding, H.; Gao, Y.; Small, C.; Kim, D. Y.; Subbiah, J.; So, F., Energy level evolution of air and oxygen exposed molybdenum trioxide films. *Applied Physics Letters* **2010,** 96, (24).
39. Gretener, C.; Perrenoud, J.; Kranz, L.; Kneer, L.; Schmitt, R.; Buecheler, S.; Tiwari, A. N., CdTe/CdS thin film solar cells grown in substrate configuration.

Progress in Photovoltaics **2013,** 21, (8), 1580-1586.

40. Romeo, N.; Bosio, A.; Tedeschi, R.; Romeo, A.; Canevari, V., A highly efficient and stable CdTe CdS thin film solar cell. *Solar Energy Materials and Solar Cells* **1999,** 58, (2), 209-218.
41. Hu, S.; Zhu, Z.; Li, W.; Feng, L.; Wu, L.; Zhang, J.; Gao, J., Band diagrams and performance of CdTe solar cells with a Sb2Te3 back contact buffer layer. *Aip Advances* **2011,** 1, (4).
42. Schmidt, T.; Durose, K.; Rothenhausler, C.; Lerch, M., Chemical stability of Sb2Te3 back contacts to CdS/CdTe solar cells. *Thin Solid Films* **2000,** 361, 383-387.
43. Abken, A. E.; Bartelt, O. J., Sputtered Mo/Sb2Te3 and Ni/Sb2Te3 layers as back contacts for CdTe/CdS solar cells. *Thin Solid Films* **2002,** 403–404, 216-222.
44. Batzner, D. L.; Romeo, A.; Terheggen, M.; Dobeli, M.; Zogg, H.; Tiwari, A. N., Stability aspects in CdTe/CdS solar cells. *Thin Solid Films* **2004,** 451, 536-543.
45. Du, M. H., First-principles study of back-contact effects on CdTe thin-film solar cells. *Physical Review B* **2009,** 80, (20).
46. Irfan, I.; Lin, H.; Xia, W.; Wu, H. N.; Tang, C. W.; Gao, Y., The effect of MoOx inter-layer on thin film CdTe/CdS solar cell. *Solar Energy Materials and Solar Cells* **2012,** 105, 86-89.
47. Gao, J.; Perkins, C. L.; Luther, J. M.; Hanna, M. C.; Chen, H.-Y.; Semonin, O. E.; Nozik, A. J.; Ellingson, R. J.; Beard, M. C., n-Type Transition Metal Oxide as a Hole Extraction Layer in PbS Quantum Dot Solar Cells. *Nano Letters* **2011,** 11, (8), 3263-3266.
48. Huang, J.; Chen, L.; He, F.; Zhang, T.; Niu, G.; Pan, J.; Xiong, Z.; Song, Q., P-type sensitized organic solar cells with cascade energy alignment. *Journal of Physics D-Applied Physics* **2012,** 45, (19).
49. Lin, H.; Xia, W.; Wu, H. N.; Tang, C. W., CdS/CdTe solar cells with MoOx as back contact buffers. *Applied Physics Letters* **2010,** 97, (12).

50. Paudel, N. R.; Compaan, A. D.; Yan, Y., Sputtered CdS/CdTe solar cells with MoO3-x/Au back contacts. *Solar Energy Materials and Solar Cells* **2013,** 113, 26-30.

51. Paudel, N. R.; Xiao, C. X.; Yan, Y. F., CdS/CdTe thin-film solar cells with Cu-free transition metal oxide/Au back contacts. *Progress in Photovoltaics* **2015,** 23, (4), 437-442.

52. Paudel, N. R.; Xiao, C. X.; El-Amin, A.; Zartman, R.; Heben, M. J.; Yan, Y. F.; Ieee, CdS/CdTe thin-film solar cells with Cu-free MoO3-x/Au back contacts. *2013 Ieee 39th Photovoltaic Specialists Conference (Pvsc)* **2013**, 1161-1164.

53. Paudel, N.; Compaan, A.; Yan, Y., Ultrathin CdTe Solar Cells with MoO3−x /Au Back Contacts. *Journal of Electronic Materials* **2014,** 43, (8), 2783-2787.

54. Lin, H.; Irfan; Xia, W.; Wu, H. N.; Gao, Y.; Tang, C. W., MoOx back contact for CdS/CdTe thin film solar cells: Preparation, device characteristics, and stability. *Solar Energy Materials and Solar Cells* **2012,** 99, 349-355.

55. Gretener, C.; Perrenoud, J.; Kranz, L.; Baechler, C.; Yoon, S.; Romanyuk, Y. E.; Buecheler, S.; Tiwari, A. N., Development of MoOx thin films as back contact buffer for CdTe solar cells in substrate configuration. *Thin Solid Films* **2013,** 535, 193-197.

56. and, R. W. B.; Eser, E., Polycrystalline thin film solar cells: Present Status and Future Potential. *Annual Review of Materials Science* **1997,** 27, (1), 625-653.

57. Albin, D. S.; Yan, Y.; Al-Jassim, M. M., The effect of oxygen on interface microstructure evolution in CdS/CdTe solar cells. *Progress in Photovoltaics: Research and Applications* **2002,** 10, (5), 309-322.

58. Lyubomirsky, I.; Rabinal, M. K.; Cahen, D., Room-temperature detection of mobile impurities in compound semiconductors by transient ion drift. *Journal of Applied Physics* **1997,** 81, (10), 6684-6691.

59. Woodbury, H. H.; Aven, M., Some Diffusion and Solubility Measurements of Cu in CdTe. *Journal of Applied Physics* **1968,** 39, (12), 5485-5488.

60. Jones, E. D.; Stewart, N. M.; Mullin, J. B., The diffusion of copper in cadmium telluride. *Journal of Crystal Growth* **1992,** 117, (1), 244-248.

61. Romero, M. J.; Albin, D. S.; Al-Jassim, M. M.; Wu, X.; Moutinho, H. R.; Dhere, R. G., Cathodoluminescence of Cu diffusion in CdTe thin films for CdTe/CdS solar cells. *Applied Physics Letters* **2002,** 81, (16), 2962-2964.

Chapter 2: Experimental Methods

2.1 Sample Preparation

ZnO, ZnO:Al_2O_3, and ZnO:ZrO_2 thin films were deposited on quartz glass, respectively, using atomic layer deposition (ALD), as shown in Fig. 2-1. Depositions were carried out in a 200 mm diameter ALD chamber in which temperature can be changed from room temperature to 300 ℃. For all the experiments, water and nitrogen were used as oxidation agent and purge gas, respectively. The volume of vapor state precursors, oxidation agent, and inert gas were controlled by fast valve made by Savannah. N-type silicon (100) wafers were placed alongside the quartz glass acting as thin film substrate.

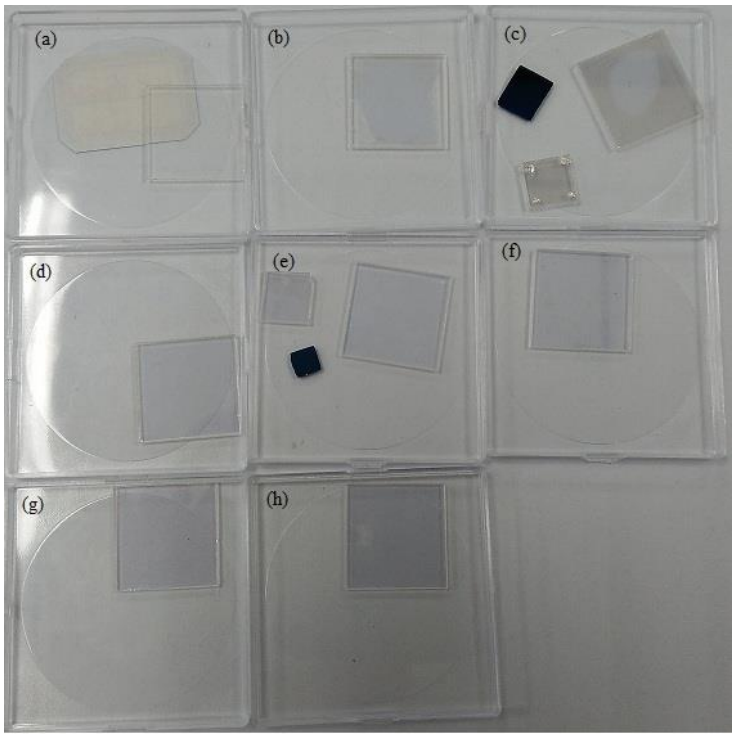

Fig. 2-1 100 nm undoped and doped ZnO thin films deposited on quartz glass by ALD: (a) quartz glass, (b) ZnO thin film, (c) ZnO:Al thin film, (d) ZnO:Zr thin film with 2% doping concentration, (e) ZnO:Zr thin film with 4% doping concentration, (f) ZnO:Zr thin film with 6% doping concentration, (g) ZnO:Zr thin film with 8% doping concentration, (h) ZnO:Zr thin film with 10% doping concentration.

CdTe thin films were obtained by high vacuum thermal evaporation (HVTE). A tungsten boat was used as the evaporation boat. The temperature of tungsten boat was measured by a home-made temperature measuring system. Glass slides and n-type silicon (100) wafers were placed in a substrate holder that can control the temperature in the range of 25 to 300 ℃. CdTe powders with 99.999% purity were used as evaporation source. 4-10 microns CdTe films were deposited prior to $CdCl_2$ post-treatment. After immersing the specimens into saturate $CdCl_2$-methanol solution,

post-treatment annealing was performed at 400 ℃ at air atmosphere for 15 minutes. Then, the recrystallized CdTe film was doped with copper ions by immersing the CdTe film in a diluted CuCl – H_2O solution. After annealed for another 15 minutes, the Cu-doped CdTe film was washed by DI water and stored in a vacuum environment.

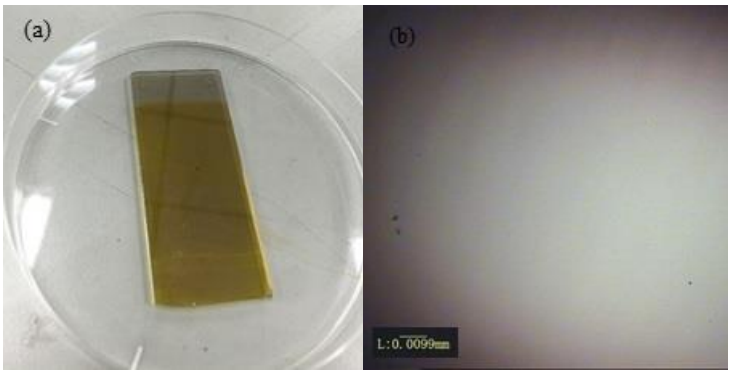

Fig. 2-2 CdTe thin films deposited on glass slide by HVTE: (a) 1μm as-deposited CdTe thin films deposited on glass slide by HVTE, (b) morphology of 1μm as-deposited CdTe thin films observed by metallographic microscopy.

Cu_xTe buffer layer was obtained from a complex process. Initially, the bromine – methanol solution was used to remove the oxide on the surface of post-treated CdTe film. A Te rich thin film was thus deposited on the surface of CdTe film, followed with evaporating a 5 nm copper layer. Without breaking the vacuum environment, annealing was performed to the multilayer specimen at 200 ℃. The chemical composition and ratio of Cu_xTe were controlled by various conditions, including concentration of bromine – methanol solution, etching time, and the thickness of copper layer.

Graphene was grown on copper foils in Low-Pressure Chemical Vapor

Deposition (LPCVD). The precursors included methanol and hydrogen. Argon was used for diluting precursors in the quartz tube. 1 cm^2 copper foils were cleaned by diluted hydrochloric acid, acetone, ethanol, and DI water in an ultrasonic cleaner three times. Later on, copper foils were put into the quartz tube immediately after cleaning process. Then, the copper was recrystallized at 1000 ℃ under hydrogen ambient. Finally, gaseous mixture containing hydrogen, methanol, and argon was admitted in the quartz tube. After graphene growth, the sliding furnace was moved to the other side, allowing a rapid cooling (cooling rate higher than 10 ℃/min) of the sample.

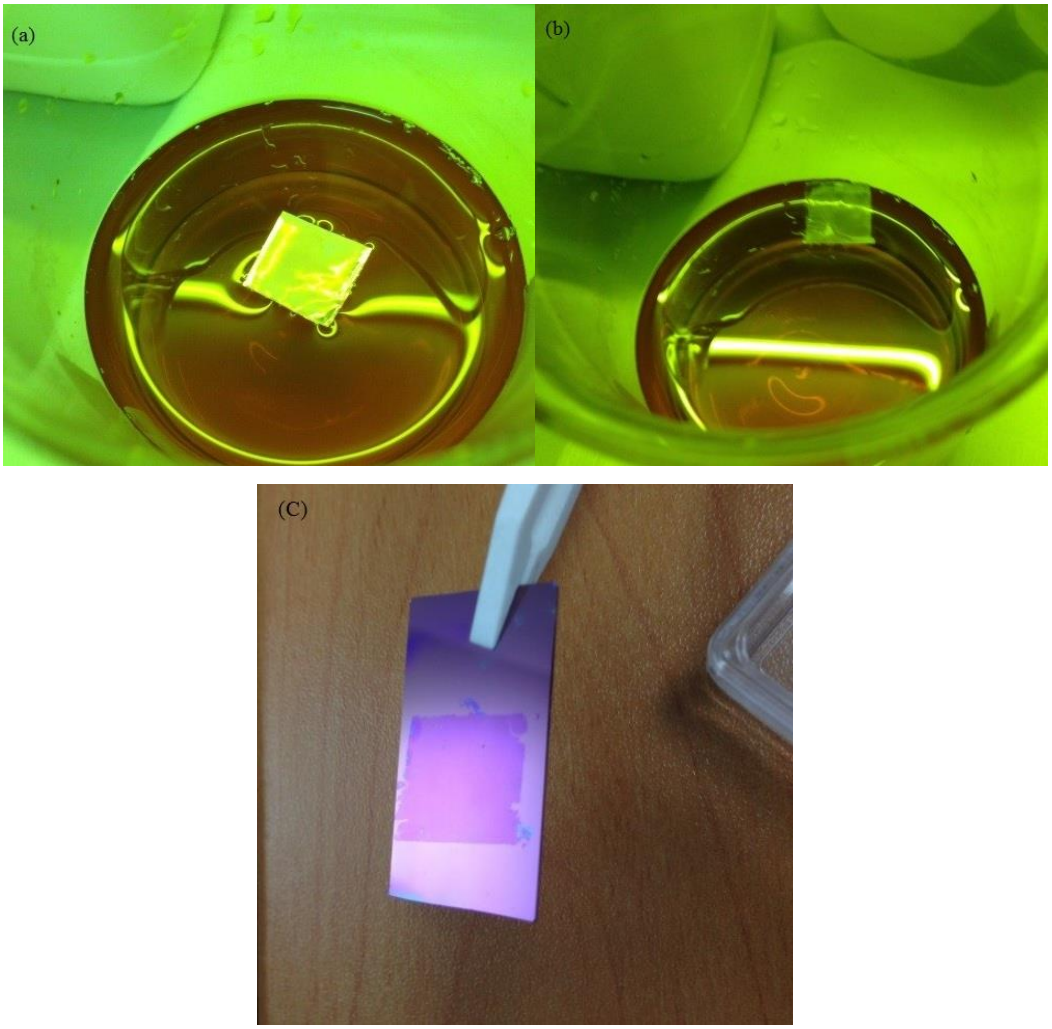

Fig. 2-3 Graphene grown copper foil (25μm) by LPCVD: (a) as-grown graphene on copper foil, (b) copper foil was removed by $FeCl_3$ solution, (c) graphene has been

transferred to SiO_2/Si substrate.

2.2 Sample Characterization

The physical and electrical properties of thin films were investigated. The ZnO-based thin films were studied using ellipsometer, X-ray diffraction (XRD), atomic force microscopy (AFM), ultraviolet-visible spectrophotometer (UV-Vis), and Hall measurement. CdTe films were characterized by XRD, and SEM. Graphene films were evaluated with metallographic microscope, scanning electron microscope (SEM), and Raman spectroscopy.

XRD is considered as one of the most analytical methods for analyzing thin film material structure. If thin film materials exhibit crystalline state where the atoms are arranged in sequence, when X-ray will interact with the atom arrays, resulting in the characteristic diffraction peaks in thin film diffraction spectra when it reaches the surface of thin film materials [1]. In addition, the comparison between the location and relative intensity of diffraction peaks in the thin film diffraction spectra and standard diffraction spectra contributes to the calculation of stress in thin film and determination of the preferred orientation film [1]. Moreover, depending on the full width at half maximum (FWHM) in thin film diffraction spectra, the size of grains in thin films can be calculated by the equation beneath,

$$\mathrm{d} = \frac{0.9\lambda}{\beta cos\theta} \qquad (2.1)$$

where d is the grain size, λ is the wavelength, β is the full width at half maximum, and

θ is the grazing angle. The variation of material structures of ZnO:Zr (4%) thin films according to annealing temperature are shown in Fig. 2-4. Preferential growth orientation and grain size can be derived from the XRD pattern.

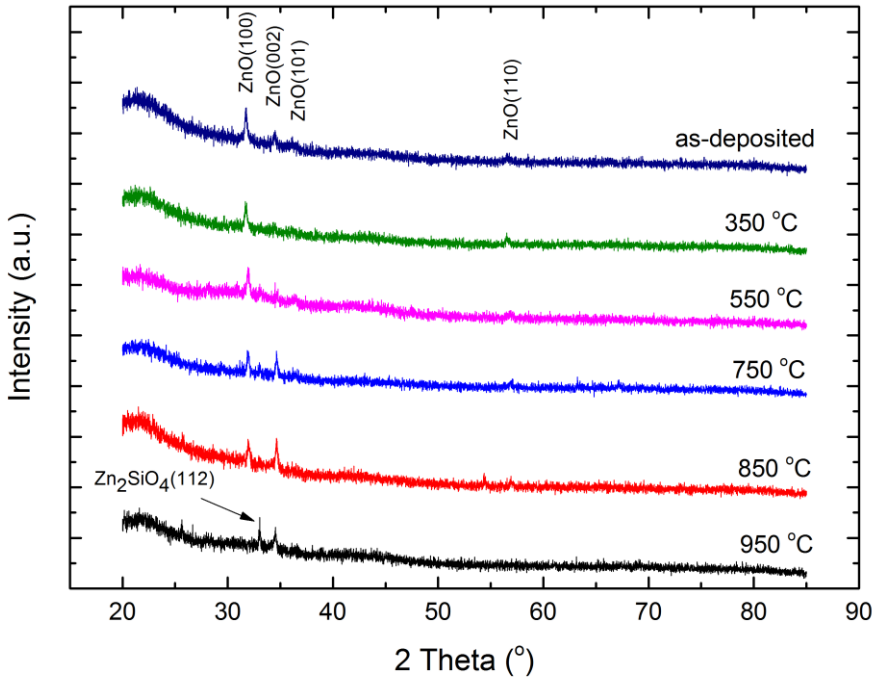

Fig. 2-4 XRD pattern of ZnO:Zr thin films (4%) annealed at different temperatures.

AFM is a nanometer measurement instrument, which obtains three-dimension images of the surface of samples. AFM can test not only the surface topology of metal, ceramics and other solid material, but also biomacromolecule, DNA, and so on [2]. AFM can test samples under different measuring environment, and cause no damage to the sample with a large measuring scale. Therefore, in recent year, AFM becomes an important instrument to test microscopic domain.

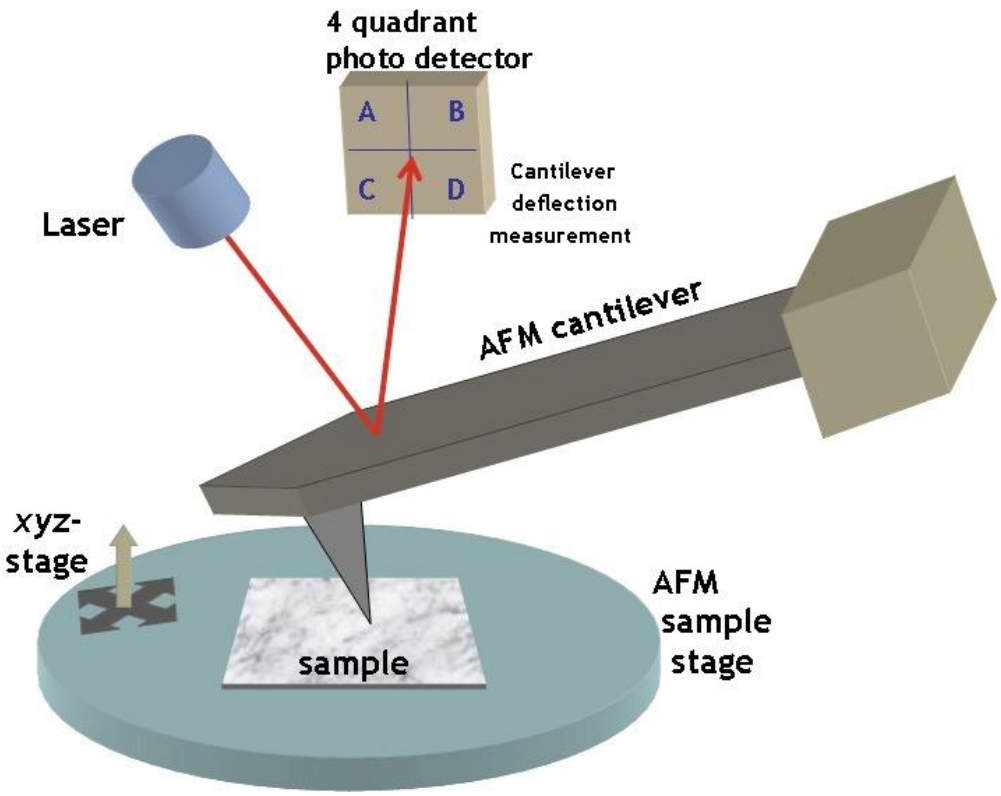

Fig. 2-5 Schematic diagram of AFM. *Reproduced from ref. [2]*.

AFM consists of four main parts, which can be observed in Fig 2-5. It is comprises of a cantilever with a sharp pinpoint, position sensitive photo detector (PSPD), scanner and feedback controller. AFM generates images of surface of samples by scanning the surface with a sharp pinpoint attached to the cantilever [2]. According to the working pattern, AFM can be divided into three modes: contact mode AFM (CM-AFM), non-contact mode AFM, and tapping mode AFM (TM-AFM) [3]. The apparatus in our experiments involves a new mode, PeakForce Tapping Mode. This is a patent mode of BRUKER. This mode combines the advantages of CM-AFM and TM-AFM. The scanning speed is high with high resolution and causes no damage to the surface of samples. Specially, the cantilever is oscillated by well below resonance, which leads to a continuous series of force-distance curves. The curves

imply a lot of material properties such as modulus, adhesion force, and deformation depth [3]. AFM characterization of ALD-derived ZnO:Zr (4%) thin film is shown in Fig. 2-6. The film has an smooth surface, with (100) preferential orientation. And the grains size is around 70 nm. All the results are compliant with the XRD results.

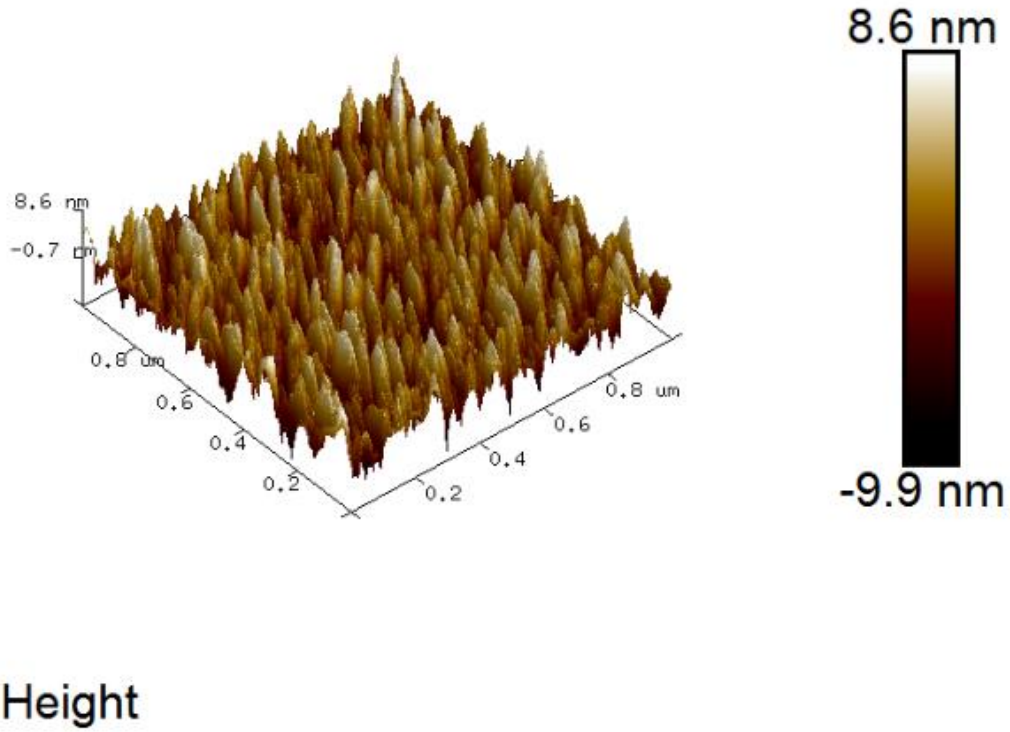

Fig. 2-6 AFM images of as-deposited ZnO:Zr films (4%) grown on Si (100) wafer by ALD.

SEM is a common analytical technique to observe the morphology and cross-section of samples. SEM scans the surface of samples using an electron beam, which interacts with the sample surface in scanning region [4]. Consequently, the morphology of the sample is determined by changes in detecting signals. There are

different types of methods of generating electron beams, depending on which, the scanning electron microscope can be divided into tungsten lamp scanning electron microscope and field emission scanning electron microscope that has high resolution about 1nm. Modern scanning electron microscope commonly attaches the Energy Dispersive X-Ray Spectroscopy (EDS) that is responsible for composition detection in the micro-region of thin films [5]. In theory, if the electron beam strikes the surface of thin films, the X-ray will be emitted from the thin film materials. The composition of thin films and their content at the impact site could be calculated by analyzing the characteristics of the X-ray photon energy. The SEM images of graphene/Cu samples are shown in Fig. 2-7. Graphene sheet can be observed by SEM. In addition, the effect of hydrogen concentration on copper substrate and graphene can be evaluated by SEM as well.

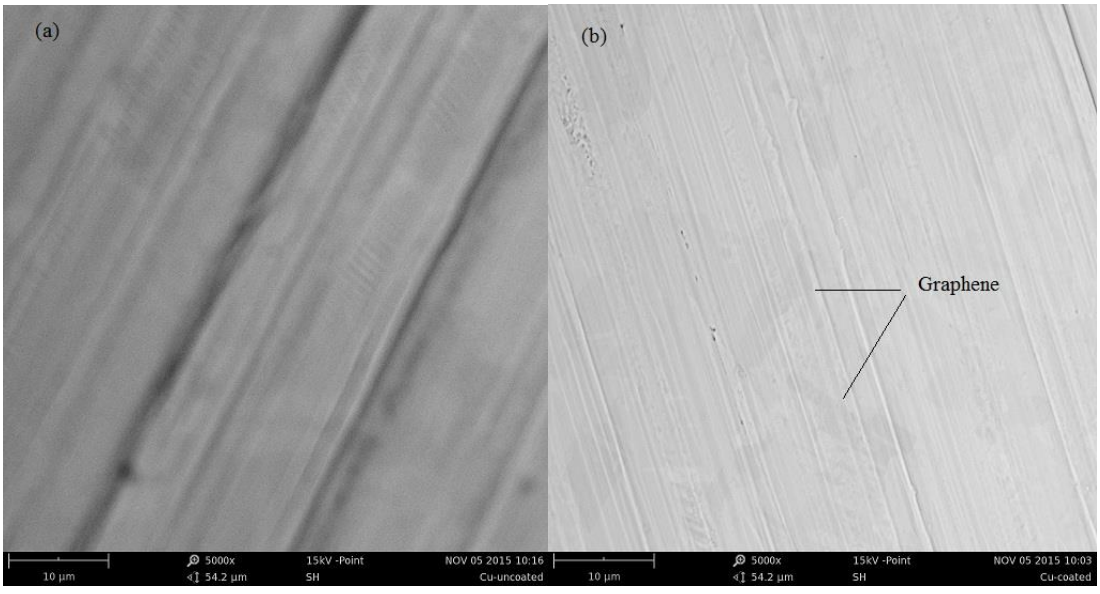

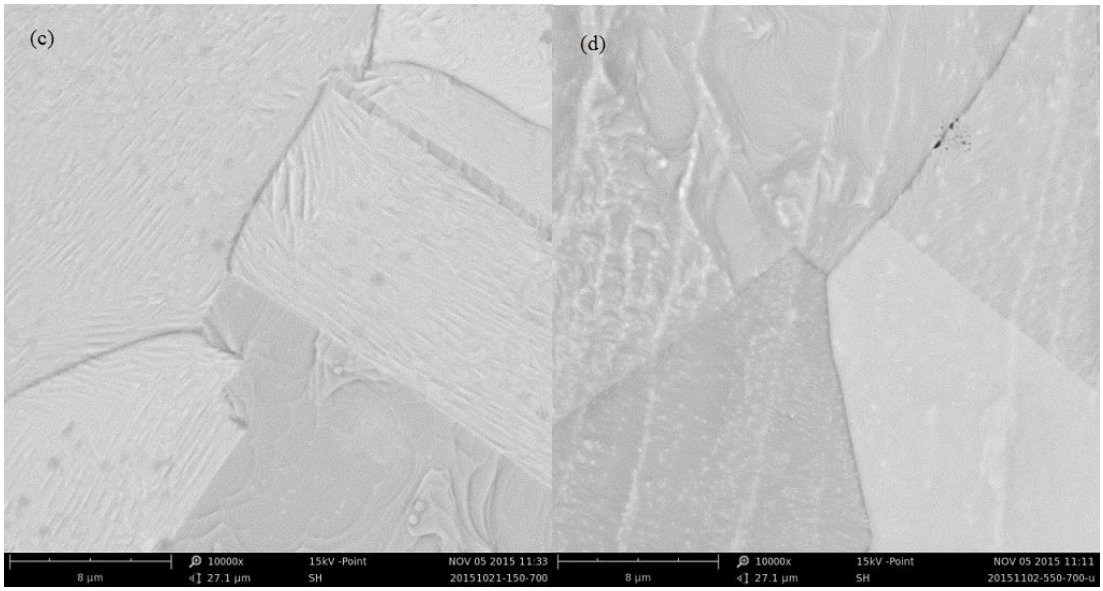

Fig. 2-7 Uncoated and coated copper foils investigated by SEM: (a) uncoated copper foil, (b) graphene has grown on copper foil, (c) 150 mTorr of H_2 during graphene growth, (d) 550 mTorr of H_2 during graphene growth.

Ultraviolet spectrophotometer is a measuring technique that characterizes the optical properties of thin film materials. When a beam of light transmits through the thin film, the semiconductor materials always absorb the photons that have energy larger than their bandgap. Moreover, some photons with energy smaller than the bandgap are also absorbed, because the electrons in semiconductor materials jump within the band gap or transit to the conduction band from impurities energy level [6]. Spectrophotometer can measure the transmittance and refractive index of thin films at different wavelengths. Assuming that the transmittance and refractive index at certain wavelength are T (%) and R (%) respectively, then, the absorption coefficient of the thin film at this wavelength is

$$\alpha = {\ln[\frac{100-R}{T}]}\Big/_{t} \qquad (2.2)$$

where t is the thickness of the thin film. Then, the absorption coefficient of the thin film over the whole wavelength could be calculated following the equation above [7]. As a consequence, the optical bandgap of the thin film can be obtained by the equation below,

$$\alpha h\nu^{m} = \mathrm{A}(\mathrm{hv} - E_g) \qquad (2.3)$$

where hv stands for the photon energy at certain wavelength and E_g represents the optical bandgap of the thin film, while m and A are constants. The value of optical bandgap of the thin film is determined by finding the tangent of a line that takes hv as the abscissa and $(\alpha hv)^m$ as ordinate. In addition, four values of m in the equation are 2, 1/2, 2/3, and 1/3 that correspond, respectively, to the direct allowed transition, indirect allowed transition, direct band transition, and indirect band transition in semiconductor materials. The type of transition in semiconductor materials is dependent on the value of m, when the linearity between hv and $(\alpha hv)^m$ is most obvious.

Raman spectroscopy is an analytical method that is based on Raman scattering effect. When light reaches the surface of samples, the incident light is absorbed by molecules, which simulates photons with higher frequencies as well as the molecules transition from high energy level to low energy level. Raman scattering effect is defined as the phenomenon where incident light undergoes changes in optical frequency after scattered by molecules of samples. Depending on the Raman scattering frequency and shift in incident light frequency, the intrinsic vibration

frequency of molecules is obtained, which then determines the significant information, including the symmetry of molecules and internal force within molecules [8]. Raman spectroscopy has become a popular and valuable tool for characterizing graphene about its thickness and properties [9]. On the other hand, graphene functions as an ideal platform for investigating the surface enhanced Raman spectra of chemical enhancement mechanism. Xie, et al. have found that graphene is able to quench the molecules fluorescence. In addition, it is reported by Ling that the Raman enhancement factor of graphene is associated with layers of graphene. In other words, more layers of graphene lead to less Raman enhancement. For example, the enhancement factor of single-layer graphene is approximately 17. Moreover, the enhancement is regarded as the chemical enhancement mechanism, which aroused by charge transfer between molecules and graphene. By calculating the I_{2D}/I_G in Fig. 2-8, it can be concluded that an bilayer graphene has been successfully deposited and transferred.

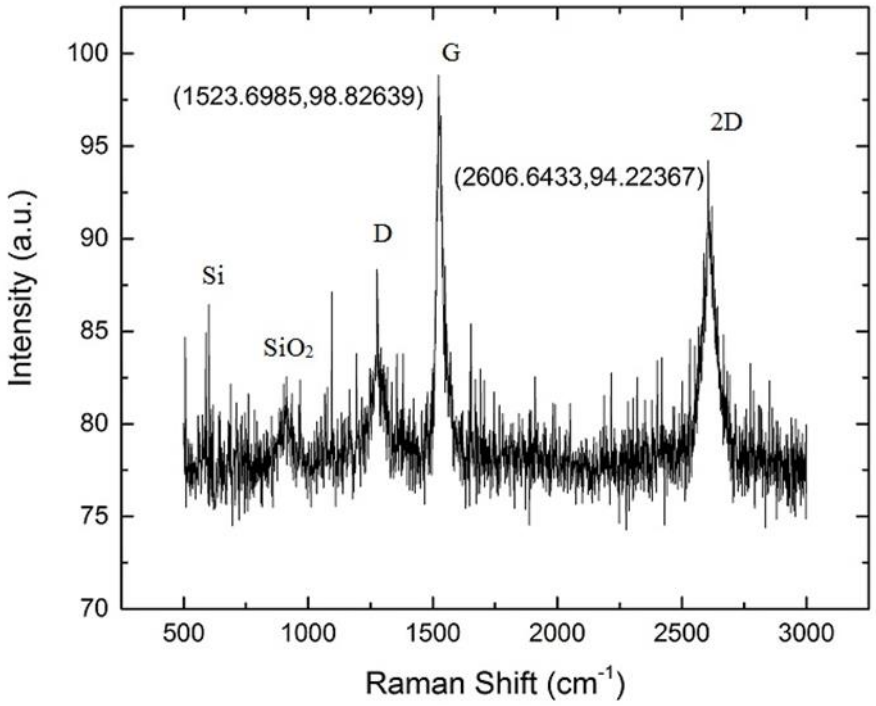

Fig. 2-8 Raman spectra of Graphene/SiO_2/Si.

Hall measurement is one of the crucial technology in semiconductor research. By using Hall measurement, the conduction type, mobility, resistivity, and carrier concentration can be evaluated. There are many types of measurement methods, including Van der Pauw, Hall bar, four-probe magnetoresistance. Among them, Van der Pauw method are most popular due to its less demanding on electrodes symmetry. To obtain an accurate values, it is significant to ensure the formation of ohmic contact between electrodes and thin film. Generally, Ga/In eutectic alloy (25% In by weight) is soldered on the thin film after surface cleaning and oxide removal. Moreover, it is necessary to make sure the resistance between any pair of contacts should less than 1Mohm.

References for the Chapter

1. Fewster, P. F., A new theory for X-ray diffraction. *Acta Crystallographica a-Foundation and Advances* **2014,** 70, 257-282.
2. Drive.Raleigh, S. Single-molecule AFM and fluorescence imaging laboratory. http://www.physics.ncsu.edu/wang/
3. Bruker AFM Probes. **http://blog.brukerafmprobes.com/category/guide-to-spm-and-afm-modes/**
4. Park, M. H.; Kim, T. H.; Yang, C. W., Thickness contrast of few-layered graphene in SEM. *Surface and Interface Analysis* **2012,** 44, (11-12), 1538-1541.
5. Donolato, C., THEORY OF SEM CHARGE-COLLECTION IMAGING OF LOCALIZED DEFECTS IN SEMICONDUCTORS. *Optik* **1978,** 52, (1), 19-36.
6. Mak, K. F.; Ju, L.; Wang, F.; Heinz, T. F., Optical spectroscopy of graphene: From the far infrared to the ultraviolet. *Solid State Communications* **2012,** 152, (15), 1341-1349.
7. Gray, A.; Balooch, M.; Allegret, S.; De Gendt, S.; Wang, W.-E., Optical detection and characterization of graphene by broadband spectrophotornetry. *Journal of Applied Physics* **2008,** 104, (5).
8. Malard, L. M.; Pimenta, M. A.; Dresselhaus, G.; Dresselhaus, M. S., Raman spectroscopy in graphene. *Physics Reports* **2009,** 473, (5–6), 51-87.
9. Calizo, I.; Ghosh, S.; Bao, W.; Miao, F.; Ning Lau, C.; Balandin, A. A., Raman nanometrology of graphene: Temperature and substrate effects. *Solid State Communications* **2009,** 149, (27–28), 1132-1135.

Chapter 3: Zirconium Doped Zinc Oxide as ITO Replacement

Cadmium oxide is the first transparent conductive oxide ever found. However, its application is limited due to the toxicity and carcinogenicity of cadmium oxide. Later on, In_2O_3-based TCOs were found as a cadmium oxide replacement. Among them, Indium Tin Oxide (ITO) achieved a great success. ITO is the first commercialized TCO material and it is the most widely used TCO thin film. ITO is regarded as an excellent photoelectric material. The commercial ITO thin films show a resistivity around 10^{-3}~10^{-5} Ω cm, with a transmittance higher than 85% in the visible range [1]. Moreover, ITO films have good mechanical properties, including good wear properties and high hardness. However, the stability of ITO limits its applications. It is demonstrated that indium precipitates out of the ITO film under the reducing atmosphere or under plasma condition. The degradation of ITO film under high temperature is also caused by the precipitation and diffusion of indium [2]. Another restriction of ITO film is the low reserve indium ore, around 0.1 ppm reservations in the earth's crust [3]. Hence, it is crucial to develop a low cost, abundant, and good properties material for Tera-watt photovoltaics application. Among them, zinc oxide has attracted great attention.

ZnO is a direct wide bandgap semiconductor material. It has excellent electromechanical coupling properties such as stability, irradiation resistance, and

photoelectric property. It is widely used in rheostat, guided-wave optical device, piezoelectric transducer, laser, and transparent conducting electrode. Intrinsic ZnO has many types of donor defects, such as interstitial zinc ion (Zn_{in}^{2+}) and oxygen vacancy (V_o^{2+}) [4]. Therefore, ZnO is a natural n-type semiconductor [5]. Yet, intrinsic ZnO film cannot be used as TCO film due to its high resistivity and unstable electrical properties. On the contrary, doped ZnO thin film shows stable electrical property. It is the donor elements that substitute the zinc ions to make the crystal structure stable [4]. Consequently, the resistivity can decrease by several orders of magnitude. On the other hand, the growth in carrier concentration increases the energy bandgap, which further facilitates the transmittance of visible light. Furthermore, thermal stability can also be increased by doping [6]. It is asserted that the thermal stability limit for intrinsic ZnO thin film is 450K. By contrast, the thermal stability limit of ZnO film doped with B, F, and Al was improved to 500K, 700K, and 800K, respectively [7, 8].

To date, ZnO-based transparent electrode has made a remarkably progress. ZnO-based TCO film in photovoltaics grade has been commercialized and is widely used in a-Si:H thin film solar cells [9]. The successful companies in this area are Nippon Sheet Glass in Japan, Asahi in Japan, AFG in the U.S., and Leybold Optics in the U.S.

It is necessary to realize that the properties of TCO are closely related to the composition, substrate, and deposition technologies. The popular TCO deposition technologies include sputtering, vacuum evaporation, spraying, pulse laser deposition, chemical vapor deposition, sol-gel, reactive ion injection, and atomic layer deposition

(ALD). Sputtering, chemical vapor deposition, and sol-gel are key technologies to the industrialization of ZnO-based thin film. ALD, on the other hand, is an important deposition technology in research community. It allows the possibility of atomic layer control and conformal deposition.

3.1 Intrinsic ZnO Layer Grown by Atomic Layer Deposition

3.1.1 Basic Principle of Atomic Layer Deposition

Semiconductor technology has led to the requirement of precise controlling of elements composition in the material. ALD meets the need for precise controlling of chemical ratio and the requirement of deposition of pinhole free film for semiconductor devices.

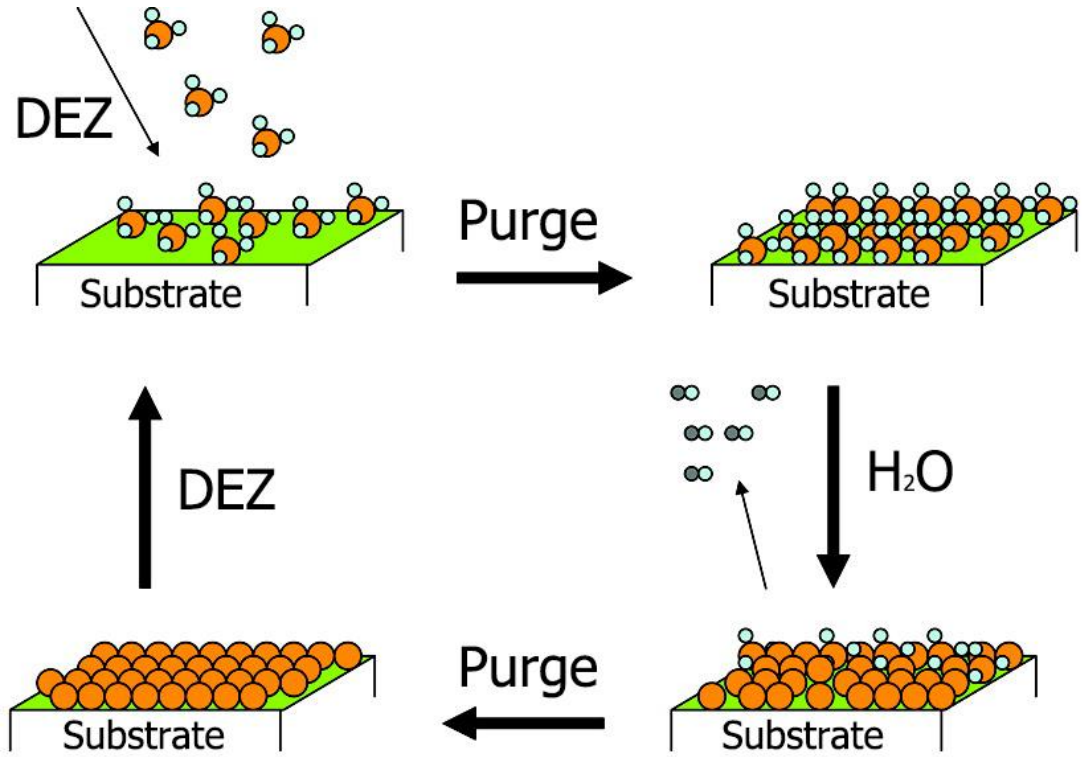

Fig. 3-1 Schematic representation of self-limiting surface reaction in ALD deposition.

Fig. 3-1 illustrates the reaction sequence in ALD. At the very beginning, the surface of a specimen exposes to the precursor. The precursor, diethylzinc (DEZ) in our case, was absorbed on the surface of the specimen. Extra precursor was removed by inert gas. Then, oxidizing agent reacts with the chemical matter that adsorb on the surface of the specimen. After the target oxide is generated, oxidizing agent is removed by another purging process. Thus far, specimen is covered with almost one atom layer and is ready for the next deposition cycle.

Most ALD processes are AB binary reaction sequences similar to the reactions that are demonstrated in Fig. 3-1. Since the reactions occur at the surface of the specimen, each of the two surface reactions is self-limiting. With each deposition cycle, a thin film with atom level thickness is successfully deposited.

It is notable that the average thickness of each cycle does not strictly agree with atomic layer of the target oxide. The adsorption of precursors is a dynamic process. The adsorbed precursors may be also desorbed from the surface areas. At another cycle, the precursors will then cover the entire unreacted surface again regardless of the structure of the surface. Hence, the films tend to be free of pinholes [10].

3.1.2 ZnO Thin Film Grown by Atomic Layer Deposition

By far the most common Zn precursors are zinc acetate, dimethyl zinc, diethyl zinc (DEZ), and zinc chloride. Oxygen sources usually prefer distilled water (H_2O), oxygen, ozone, and nitrous oxide. DEZ and H_2O are mostly used in ALD to grow zinc oxide. The reaction of DEZ and H_2O is an exothermic process. Therefore, the reaction can occur at low temperature. It is reported that the DEZ precursor has been successfully used from room temperature to the temperature as high as 600 ℃. Typical deposition temperatures are in the range of 100~200 ℃ [11]. Except Zn precursor, the deposition temperature has effect on the oxygen sources. Compared with other oxidation agent, such as oxygen, ozone, and nitrous oxide, distilled water has similar deposition rate but requires much lower deposition temperature.

In our project, DEZ and H_2O are the two precursors used in ALD. The reaction mechanism of DEZ and H_2O follows:

$$Zn(CH_2CH_3)_2 + H_2O \rightarrow ZnO + 2C_2H_6 \qquad (3.1)$$

$$\Delta H = -70\text{kcal} \qquad (3.2)$$

The ALD experiments were performed in a MNT F-200 system. The working

chamber is 200mm in diameter and can be heated from room temperature to 300 ℃. The bubbler and pipeline were heated allowing vapor state diethyl zinc and water flow into the chamber. The precursor delivery volume was controlled by fast Savannah valves with controllable opening time (>10 ms). Detail of the deposition parameters are listed in Table 3-1.

Table 3-1. Deposition parameters for ZnO thin film.

Substrate temperature	180-220 ℃
Nitrogen flow rate	20 sccm
Working pressure	30 Pa/225 mTorr
Cycles	150
Pulse sequences	(DEZ/purge/water/purge)
DEZ/purge/H_2O/purge	0.02/20/0.02/20 s

ZnO thin films of 25-35 nm were deposited on a Si substrate. The thickness of the thin films was characterized by ellipsometry. Thus, the growth condition was examined by simply altering the substrate temperature, while other growing parameters were kept constant.

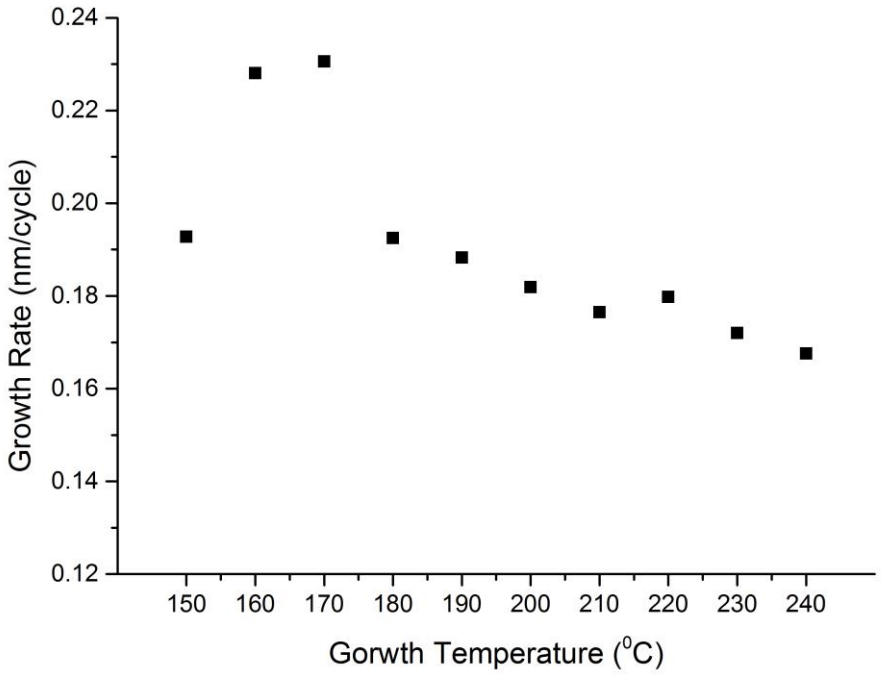

Fig. 3-2 Growth rate per cycle of ZnO under various substrate temperatures.

Fig. 3-2 shows the average growth per cycle of ZnO as a function of growing temperature. The growth rate increases rapidly with the increasing of substrate temperature and saturates at 160 ℃. The growth window is found at the range from 180–220 ℃, and the growth rate is around 1.8 angstrom per cycle. The growth rate approaches the reported 1.8-1.9 angstrom from 180–220 ℃ [12, 13]. At a higher temperature, growth rate decreases dramatically. It is speculated that the ALD precursors are evaporated or are released from the substrate at high temperatures. Therefore, precursors do not effectively react with the initial substrate. Generally, reactions only take place at the pinholes and craters of the initial substrate. The island nucleation phenomenon at the beginning of deposition is described by a Volmer-Weber growth mechanism [14]. Nucleus and islands growth at holes of the

initial surface at the very beginning of ALD deposition. After multiple cycles, the islands grow and gather together to form a continuous thin film. Therefore, the average growth rate is expected to be low.

3.1.3 ZnO Thin Film Characterization

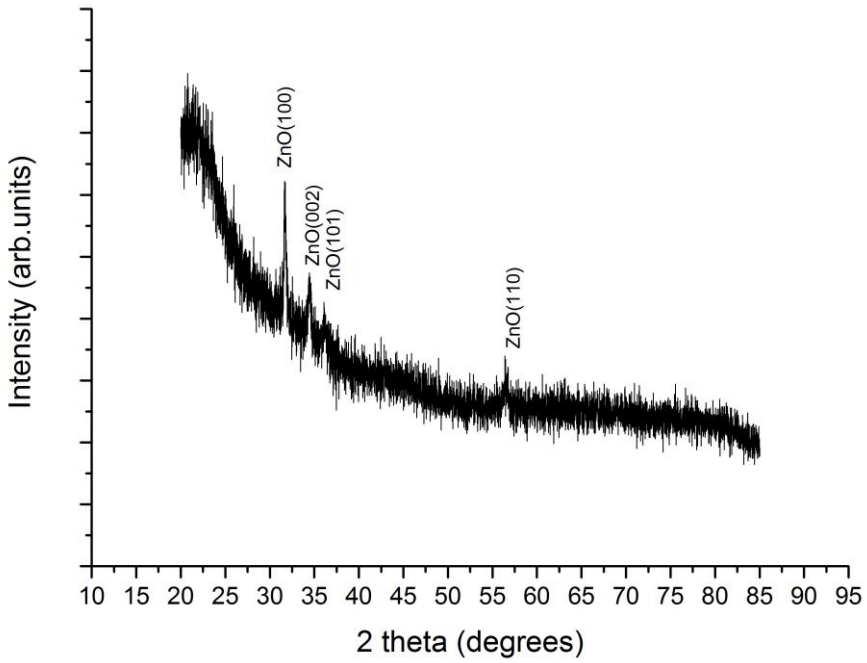

Fig. 3-3 XRD pattern of ZnO thin film grown at 200 ℃.

The XRD investigations performed in the angular range of 10-40 ° indicate that films grown at temperature between 150 ℃ and 240 ℃ are polycrystalline. Fig. 3-3 illustrates the XRD spectrum of ZnO thin film grown at the temperature of 200 ℃. It shows (100), (002), and (101) crystallographic orientations, in which (100) and (101) represent the orientations of silicon substrate. It is reported that the preferred crystallographic orientation is related to the growth temperature, pulsing time, and

purging time [15]. In Fig.3-3, the preferential ZnO is grown with a-axis in the plane of the film. It is expected that the primary ZnO growth mode will be changed to the one with c axis perpendicular to the surface, with the increasing growth temperature [16, 17]. In addition, the (002) peak becomes more obvious for ZnO films grown at higher temperature.

3.2 ZnO:Al Layer Grown by Atomic Layer Deposition

3.2.1 ZnO:Al Thin Film Grown by Atomic Layer Deposition

In order to take control of the electrical properties of ZnO thin films, a variety of elements are doped into ZnO films using ALD respectively. Aluminum has been considered as the most common doping element [18]. Although ZnO has a large resistivity, Aluminum-doped ZnO (ZnO:Al) reduces the resistivity to 10^{-4} Ω·cm, with an transmittance larger than 80% over the visible wavelengths [11, 18]. Therefore, Al-doped ZnO can function as an alternative as a transparent conducting oxide.

The ZnO:Al thin films were deposited on Si (100) and glass by ALD with trimethylaluminum ($Al(CH_3)_3$ or TMA), DEZ, and H_2O as precursors and N_2 as purging gas. The detailed parameters are listed in Table 3-2.

Table 3-2 Deposition parameters for ZnO:Al thin film.

Substrate temperature	180-200 ℃

Nitrogen flow rate	20 sccm
Working pressure	30 Pa/225 mTorr
Cycles	500
Al_2O_3 pulse sequences	(TMA/purge/ H_2O/purge)
ZnO pulse sequences	(DEZ/purge/ H_2O/purge)
DEZ/purge/H_2O/purge/TMA/purge/H_2O/purge	0.02/20/0.02/20/0.02/20/0.02/20 s

The growth temperature ranges from 180 ℃ to 220 ℃. The ALD pulse sequence is divided into two parts, 0.02/20/0.02/20s (DEZ/purge/H_2O/purge) and 0.02/20/0.02/20 s (TMA/purge/H_2O/purge), which are designed to fabricate ZnO and Al_2O_3, respectively. There are total 500 cycles. The ZnO:Al was deposited by repeating 25 times ALD sequence that is composed of 19 cycles of DEZ/purge/H_2O/purge and one cycle of TMA/purge/H_2O/purge following the separate time in Table 3-2. It is clear that the cycle ratio of Zn and Al is 19:1. Considering the growth rate of ZnO and Al_2O_3, it is reasonable to determine the doping concentration of ZnO:Al thin film.

3.2.2 ZnO:Al Thin Film Characterization

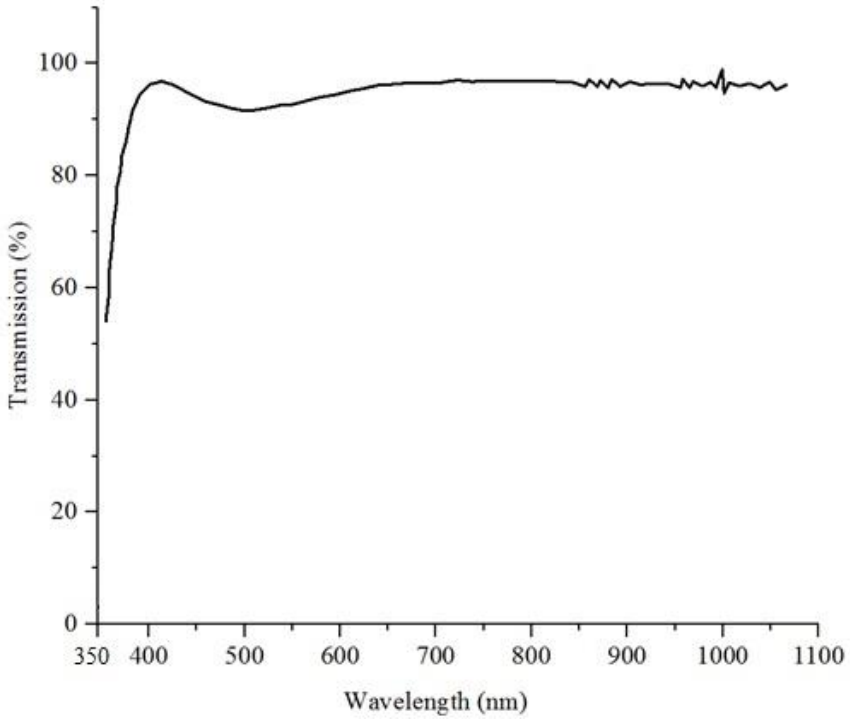

Fig. 3-4 Transmission spectrum of ZnO:Al film characterized by UV-Vis spectrophotometry.

Transparency is an important factor that judges whether the thin film could replace the ITO as a transparent conducting oxide. Fig. 3-4 shows the transmission spectrum of an ZnO:Al thin film grown at 200 ℃. The optical transparency of ZnO:Al thin films was measured by an UV spectrophotometry. It is obvious that the optical transparency of ZnO:Al is larger than 80% over the wide spectra region of 400-1100 nm. The high transmittance indicates that it is reasonable to use ZnO:Al thin films in optoelectronic devices.

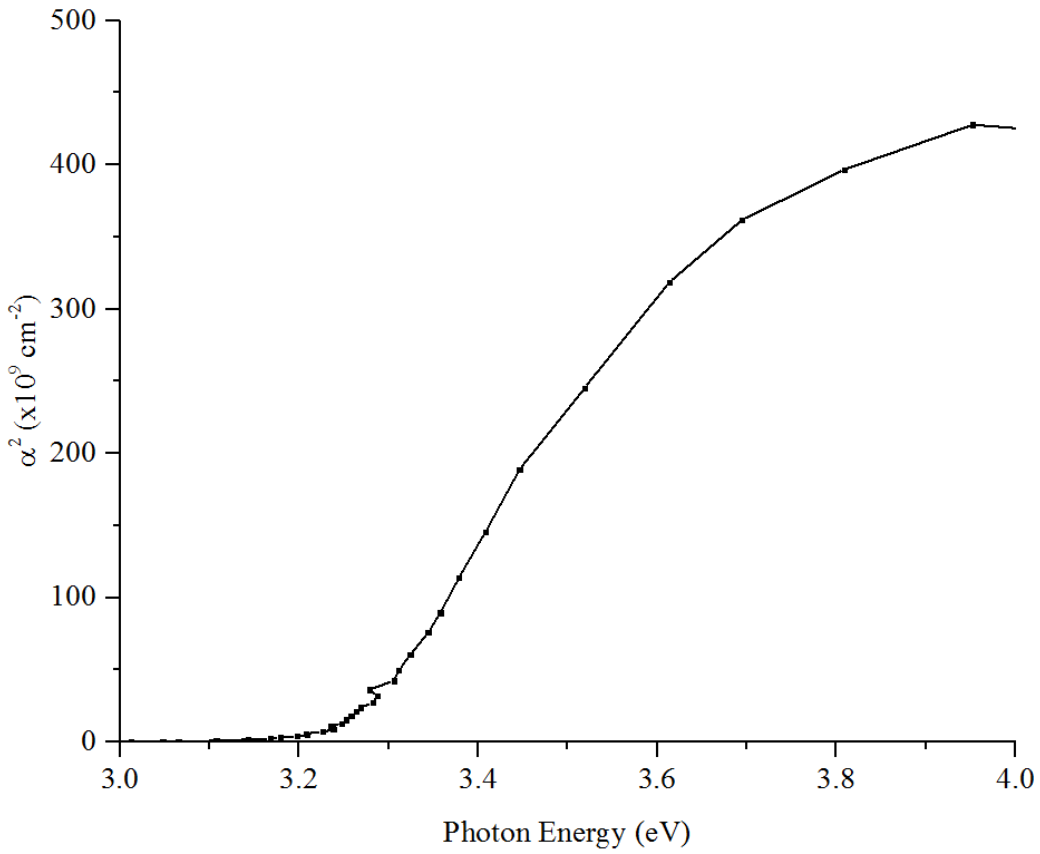

Fig. 3-5 The α^2 versus hv plot of the ZnO:Al film grown at 200 ℃.

Fig. 3-5 shows the plot of α^2 versus hv, which is obtained from Fig. 3-4 by the calculation in Appendix 1. α stands for the absorption coefficient and hv is the photon energy. Tauc et al. [19] put forward the expression explaining the relationship between the absorption coefficient and photon energy with given transmittance.

$$\alpha = \frac{A(hv-Eg)^{m/2}}{hv} \qquad (3.3)$$

where m equals to1 representing the direct transition while m equals to 4 standing for the indirect transition, and A is a constant.

Moreover, the absorption coefficient follows an exponential law corresponding to Pankove's expression [19]

$$\alpha(hv) = AE_0^{\frac{3}{2}}\exp(\frac{hv}{E_0}) \qquad \text{for } hv<Eg \qquad (3.4)$$

where E_0 stands for the width of the localized state in the bandgap.

The bandgap (Eg) of ZnO:Al films is obtained by the value of intersection of the tangent line and the axis of photon energy. It is found that the bandgap of the ZnO:Al film grown at 200 ℃ is 3.25 eV.

3.3 ZnO:Zr Layer Grown by Atomic Layer Deposition

3.3.1 Material Properties of ZnO:Zr

The limitation of ZnO thin films lies on its instability at high temperature in the atmosphere of oxygen, which leads to the deterioration of electrical properties during aging test in environment condition. ZnO thin films doped by Al, Ga, or In achieve the stabilization with improved conductivity [20]. Ahn et al. investigated ZnO:Hf grown at 200 ℃ by ALD [21]. It is reported that ZnO:Hf thin films with low Hf contents (<6.7 at.%) show high conductivity. In addition, the electrical resistivity is reduced to 6×10^{-4} Ω·cm with the Hf content about 3.3 at.% and the highest carrier concentration of 3.7×10^{20} cm^{-3} [21]. Moreover, it is found that electrical stability of ZnO thin films doped by group IV elements such as Hf is better than that doped by group III elements such as Al. With respect to the ZnO:Al thin films, the Al diffusion at high temperature results in the instability of ZnO:Al thin films. Besides, ZnO:Al thin films grown by sputtering exhibit low electron mobility with increasing carrier concentration because of grain barrier-limited transports [16].

Recently, it is popular to dope ZnO thin films with ZrO_2, which crystallizes in a

monoclinic structure. However, at temperature of 980 and 2300 ℃, the ZrO_2 will transform to tetragonal and cubic structures, respectively [22]. During the transform between monoclinic and tetragonal phase, a volume contraction of approximately 3% occurs resulting in cracks in the film. Compared with ZnO:Al, ZnO:Zr thin films are stable and show low possibility to create micro-cracking after several cycles over a wide range of temperatures [23].

3.3.2 ZnO:Zr Thin Film Grown by Atomic Layer Deposition

ZnO:Zr thin films were also fabricated by ALD, which dopes ZrO_2 into ZnO thin films by depositing one cycle of ZrO_2 following with several cycle of ZnO in a circulation mode. The precursors in the fabrication process include tetrakis-(dimethylamino)- zirconium ($Zr[N(CH_3)_2]_4$ or TDMAZ), DEZ, and H_2O.

Table 3-3 Deposition parameters for ZnO:Zr thin films.

Substrate temperature	180-220 ℃
Nitrogen flow rate	20 sccm
Working pressure	30Pa/225 mTorr
Cycles	500
Concentration ratio	2%, 4%, 6%, 8%, 10%
ZrO_2 pulse sequences	(TDMAZ/purge/ H_2O/purge)
ZnO pulse sequences	(DEZ/purge/ H_2O/purge)
DEZ/purge/H_2O/purge/ TDMAZ /purge/H_2O/purge	0.02/20/0.02/20/ 0.20/20/0.02/20 s

Similar to ZnO:Al, the growth temperature is designed ranging from 160 ℃ to 240 ℃. The ALD pulse sequence is also divided into two parts：0.02/20/0.02/20 s (DEZ/purge/H_2O/purge) and 0.02/20/0.02/20 s (TDMAZ/purge/H_2O/purge) that correspond to the deposition of ZnO and Al_2O_3, respectively. In Table 3-3, the concentration ratios are 2%, 4%, 6%, 8% and 10%, which represent the different ratios of Zr and Zn. For example, if the concentration ratio of Zr and Zn is 2%, it indicates that the ZrZO thin film is deposited by repeating 10 times ALD sequence consisting of 49 cycles of DEZ/purge/H_2O/purge followed by one cycle of TDMAZ/purge/H_2O/purge. Consequently, the total cycle is 500.

3.3.3 ZnO:Zr Thin Films Characterization

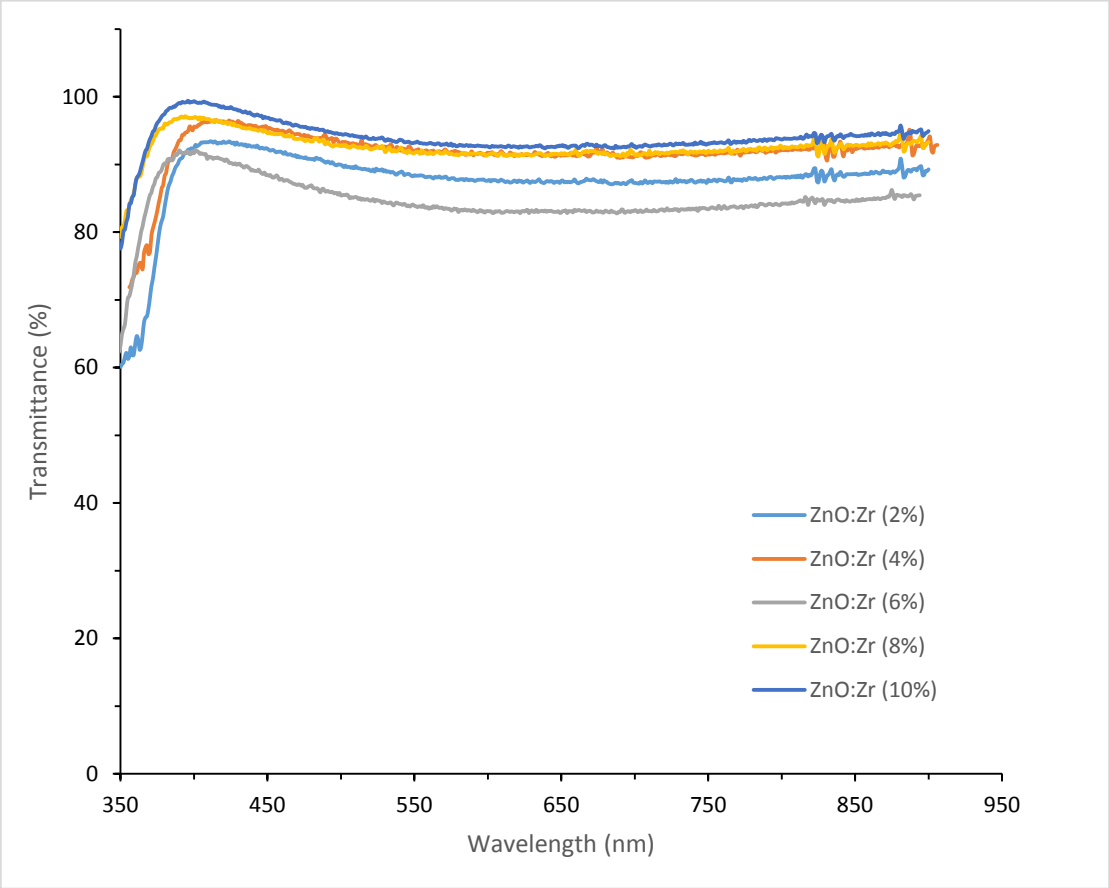

Fig. 3-6 Transmittance spectrum of ZnO:Zr films with different doping concentrations characterized by UV-VIS spectrophotometry.

Similarly, the optical transmittance of ZnO:Zr thin films were measured to evaluate their optical properties. Fig. 3-6 shows the transparency spectrum of ZnO:Zr films with different concentration ratios grown at 200 ℃. Compared with the transparency spectrum of the ZnO:Al thin film above, ZnO:Zr thin films with different Zr concentrations show an average transmittance larger than 90% over the same spectra region. Moreover, it is obtained that ZnO:Zr thin films with higher ratio of Zn and Zr have larger optical transparency over the visiblewavelength. On the contrary, the ZnO: Zr thin film with a higher concentration ratio seems to have a worse transmittance.

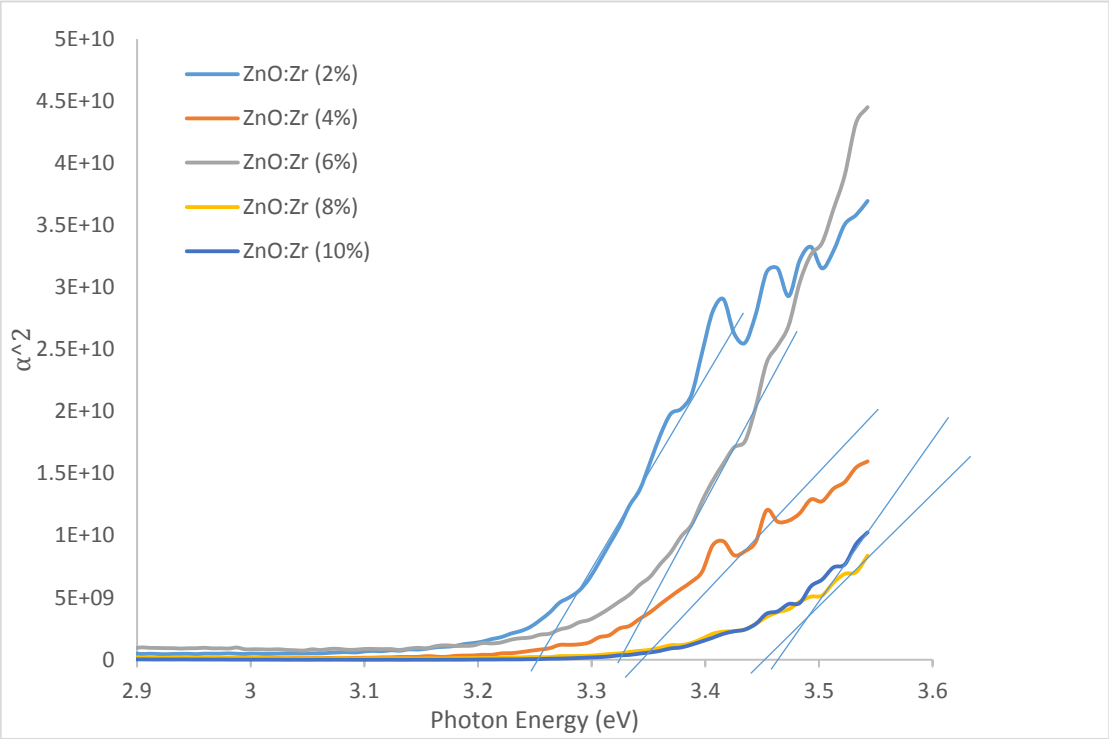

Fig. 3-7 The α^2 versus hv plot of the ZnO:Zr films with different doping concentrations.

Fig. 3-7 shows the plot of α^2 versus hv, which is obtained from Fig. 3-6 by the same way as mentioned in section 3.2.2. The bandgap (Eg) of ZnO:Al films is obtained by the value of intersection of the tangent line and the axis of photon energy. It is clear that the absorption coefficient of ZnO:Zr is lower for the ZnO:Zr thin film with higher Zr concentration. Because the carrier concentration decreases with increasing Zr concentration; in this case, increasing Zr atoms concentrate on some neutral defects without contribution to the free electrons [24]. Moreover, there are many factors related to the mobility of thin films such as the grain size, roughness of surface, and scattering of electrons with the ionized impurities [19]. Some other defects are regarded as the traps to parts of carriers.

According to Fig. 3-7, it is found that the values of bandgap of the ZrZO films with ratio of 2%, 4%, 6%, 8%, and 10% are 3.25, 3.32, 3.35, 3.44, and 3.47 eV

respectively. The increase of bandgap is explained by the upwards shifting of conduction band, due to the exchange and correlation among the electrons. Moreover, there is additional shift in conduction band, when the electron density relaxes around the impurities [24].

The bandgap widening of degenerate semiconductors can be explained by the Burstein Moss (B-M) effect. The B-M effect is expressed as:

$$E_g = E_{g0} + \Delta E_g^{BM} \qquad (3.5)$$

Where E_{g0} is the bandgap energy of intrinsic semiconductor, ΔE_g^{BM} represents the B-M shifted bandgap energy, and E_g is the bandgap energy of doped materials.

The B-M shift bandgap energy follows:

$$\Delta E_g^{BM} = \frac{h^2}{8m_e^*}\left(\frac{3}{\pi}\right)^{2/3} n_e^{\,2/3} \qquad (3.6)$$

Where n_e is electron carrier density, h is Plank's constant, and m_e^* is the effective electron mass in conduction band.

From the equations above, the blue-shifting of heavily doped ZnO:Zr film is explicable. With increase in zirconium concentration, the electron carrier density increase. Since ΔE_g^{BM} is proportional to $n_e^{\,2/3}$, high zirconium concentration will result in a large bandgap energy.

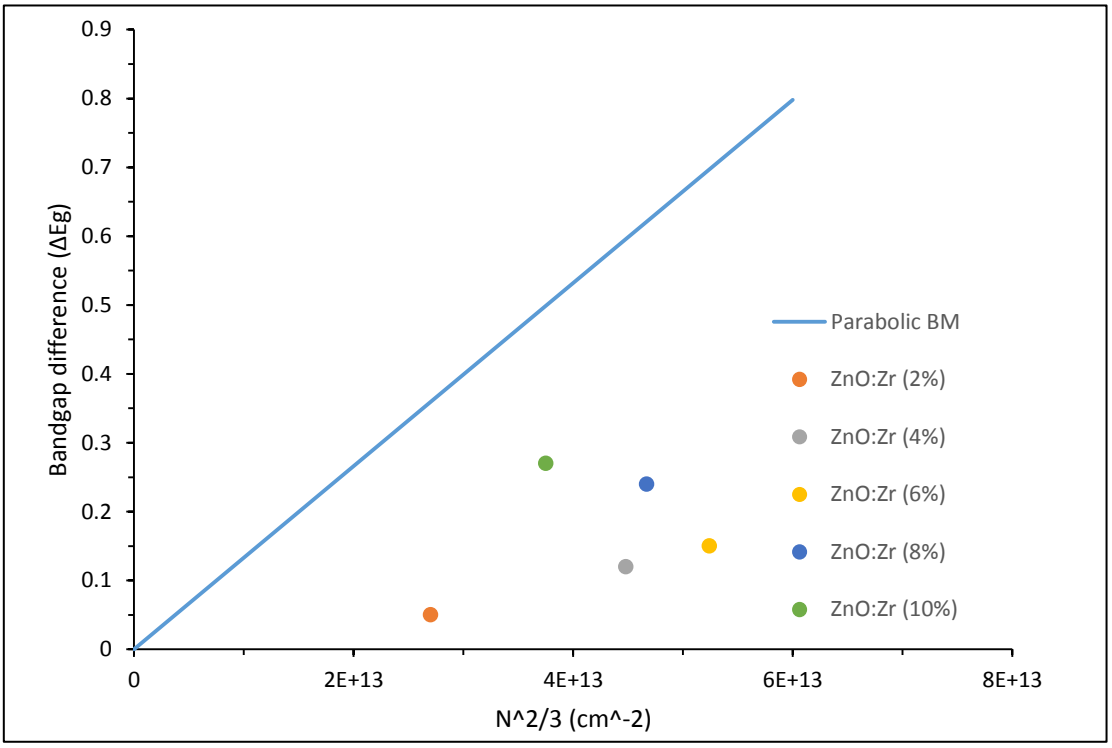

Fig. 3-8 Bandgap difference as a function of Zr doping concentration

As shown in Fig. 3-8, bandgap difference of doped ZnO thin films do not strictly follow the B-M equation. The bandgap difference of all samples were well below the parabolic BM curve. Carrier concentrations increase gradually when Zr doping concentration increase from 2% to 6%. In addition, carrier concentration drop to $3.2 \times 10^{20}\ cm^{-3}$, after reaching the its highest value at 6% Zr concentration. From Fig. 3-8, it is clear that the bandgap different of 10% ZnO:Zr thin films was higher than that of 8% and 4% ZnO:Zr though they have similar carrier concentration. Hence, it is reasonable to deduce a conclusion that the contributions of widening energy bandgap is a combination of B-M effect and larger bandgap of ZrO_2 (5.8 eV) compared to that of ZnO (3.2 eV). Extra doping of ZrO2 results in higer energy bandgap, even though the carrier concentration decline afterward.

References for the Chapter

1. Hosono, H.; Ohta, H.; Orita, M.; Ueda, K.; Hirano, M., Frontier of transparent conductive oxide thin films. *Vacuum* **2002,** 66, (3–4), 419-425.
2. Kim, H.; Piqué, A.; Horwitz, J. S.; Mattoussi, H.; Murata, H.; Kafafi, Z. H.; Chrisey, D. B., Indium tin oxide thin films for organic light-emitting devices. *Applied Physics Letters* **1999,** 74, (23), 3444-3446.
3. Granqvist, C. G.; Hultaker, A., Transparent and conducting ITO films: new developments and applications. *Thin Solid Films* **2002,** 411, (1), 1-5.
4. Pena, J. L.; Rejon, V.; Ares, O.; Camacho, J. M.; Rios-Flores, A.; Ieee, The ZnO-reflectance effect on the heterojunction ITO/ZnO/CdS/CdTe. *2012 38th Ieee Photovoltaic Specialists Conference (Pvsc)* **2012**, 2021-2023.
5. Apostoluk, A.; Zhu, Y.; Canut, B.; Masenelli, B.; Delaunay, J. J.; Znajdek, K.; Sibinski, M., Investigation of luminescent properties of ZnO nanoparticles for their use as a down-shifting layer on solar cells. *Physica Status Solidi C: Current Topics in Solid State Physics, Vol 10, No 10* **2013,** 10, (10), 1301-1307.
6. Chalker, P. R.; Marshall, P. A.; Romani, S.; Roberts, J. W.; Irvine, S. J. C.; Lamb, D. A.; Clayton, A. J.; Williams, P. A., Atomic layer deposition of Ga-doped ZnO transparent conducting oxide substrates for CdTe-based photovoltaics. *Journal of Vacuum Science & Technology A* **2013,** 31, (1), 5.
7. Guillén, C.; Martínez, M. A.; Maffiotte, C.; Herrero, J., Chemistry of CdS / CuInSe2 Structures as Controlled by the CdS Deposition Bath. *Journal of The Electrochemical Society* **2001,** 148, (11), G602-G606.
8. Morris, G. C.; Tottszer, A.; Das, S. K., Comparison between evaporation and electrodeposited cadmium sulfide for n-CdS/p-CdTe solar cells. *Mater. Forum* **1991**, (15), 164-170.
9. Springer, J.; Rech, B.; Reetz, W.; Müller, J.; Vanecek, M., Light trapping and optical losses in microcrystalline silicon pin solar cells deposited on

surface-textured glass/ZnO substrates. *Solar Energy Materials and Solar Cells* **2005,** 85, (1), 1-11.

10. Fabreguette, F. H.; Wind, R. A.; George, S. M., Ultrahigh x-ray reflectivity from W ⁄ Al2O3 multilayers fabricated using atomic layer deposition. *Applied Physics Letters* **2006,** 88, (1), 013116.
11. Tommi, T.; Maarit, K., Atomic layer deposition of ZnO: a review. *Semiconductor Science and Technology* **2014,** 29, (4), 043001.
12. Guziewicz, E.; Godlewski, M.; Krajewski, T. A.; Wachnicki, Ł.; Łuka, G.; Domagała, J. Z.; Paszkowicz, W.; Kowalski, B. J.; Witkowski, B. S.; Dużyńska, A.; Suchocki, A., Zinc oxide grown by atomic layer deposition – a material for novel 3D electronics. *physica status solidi (b)* **2010,** 247, (7), 1611-1615.
13. Gong, S.; Bang, S.; Jeon, H.; Park, H.-H.; Chang, Y.; Chang, H., Effects of atomic layer deposition temperatures on structural and electrical properties of ZnO films and its thin film transistors. *Met. Mater. Int.* **2010,** 16, (6), 953-958.
14. Argile, C.; Rhead, G. E., Adsorbed layer and thin film growth modes monitored by Auger electron spectroscopy. *Surface Science Reports* **1989,** 10, (6), 277-356.
15. Guziewicz, E.; Godlewski, M.; Krajewski, T. A.; Wachnicki, L.; Luka, G.; Paszkowicz, W.; Domagala, J. Z.; Przezdziecka, E.; Lusakowska, E.; Witkowski, B. S., ZnO by ALD - Advantages of the Material Grown at Low Temperature. *Acta Phys. Pol. A* **2009,** 116, (5), 814-817.
16. Godlewski, M.; Guziewicz, E.; Luka, G.; Krajewski, T.; Lukasiewicz, M.; Wachnicki, L.; Wachnicka, A.; Kopalko, K.; Sarem, A.; Dalati, B., ZnO layers grown by Atomic Layer Deposition: A new material for transparent conductive oxide. *Thin Solid Films* **2009,** 518, (4), 1145-1148.
17. Min, Y.-S.; An, C. J.; Kim, S. K.; Song, J.; Hwang, C. S., Growth and Characterization of Conducting ZnO Thin Films by Atomic Layer Deposition. *Bulletin of the Korean Chemical Society* **2010,** 31, (9), 2503-2508.
18. Dasgupta, N. P.; Neubert, S.; Lee, W.; Trejo, O.; Lee, J.-R.; Prinz, F. B.,

Atomic Layer Deposition of Al-doped ZnO Films: Effect of Grain Orientation on Conductivity. *Chemistry of Materials* **2010,** 22, (16), 4769-4775.

19. Tauc, J.; Grigorovici, R.; Vancu, A., Optical Properties and Electronic Structure of Amorphous Germanium. *physica status solidi (b)* **1966,** 15, (2), 627-637.
20. Ahn, C. H.; Kim, J. H.; Cho, H. K., Tunable Electrical and Optical Properties in Composition Controlled Hf:ZnO Thin Films Grown by Atomic Layer Deposition. *Journal of the Electrochemical Society* **2012,** 159, (4), H384-H387.
21. Wang, F.; Zhao, X.; Duan, L.; Wang, Y.; Niu, H.; Ali, A., Structural, optical and electrical properties of Hf-doped ZnO transparent conducting films prepared by sol–gel method. *Journal of Alloys and Compounds* **2015,** 623, 290-297.
22. Qadri, S. B.; Kim, H.; Khan, H. R.; Piqué, A.; Horwitz, J. S.; Chrisey, D.; Kim, W. J.; Skelton, E. F., Transparent conducting films of In2O3–ZrO2, SnO2–ZrO2 and ZnO–ZrO2. *Thin Solid Films* **2000,** 377–378, 750-754.
23. Lv, M.; Xiu, X.; Pang, Z.; Dai, Y.; Han, S., Influence of the deposition pressure on the properties of transparent conducting zirconium-doped zinc oxide films prepared by RF magnetron sputtering. *Applied Surface Science* **2006,** 252, (16), 5687-5692.
24. Lin, M.-C.; Chang, Y.-J.; Chen, M.-J.; Chu, C.-J., Characteristics of Zr-Doped ZnO Thin Films Grown by Atomic Layer Deposition. *Journal of The Electrochemical Society* **2011,** 158, (6), D395-D398.

Chapter 4: Back Contact Buffer Layer as Ion Diffusion Barrier

CdTe solar cells efficiencies below 20% have been achieved by various deposition strategies and technologies. Yet, the best cell to date has been believed to be far away from the theoretical value. In the past two decades, intensive researches focused on the understanding of critical issues, including junction activation treatment, doping of heteroatoms, role of impurities in CdTe solar cells, and technological problems. Thus far, CdTe solar cells efficiency has slowly approached its theoretical value and is comparable to that of commercial available silicon solar cells. To date, one of the challenges arisen is the formation of stable ohmic back contact. As known, the introduction of back contact buffer layer, such as Cu_xTe, ZnTe:Cu, Sb_2Te_3, and MoO_x etc., improves solar cells efficiency by forming good ohmic contact with CdTe layer. However, metal ions diffuse from the buffer layer or the substrate to the junction form Generation-Recombination centers, which leading to a serious decreasing of power conversion efficiency. Therefore, it is necessary to investigate the stability issues of CdTe solar cells in regards to Cu_xTe buffer layer. In this chapter, we will deposit a CdTe thin film on glass by high vacuum thermal evaporation. After treated with wet cadmium chloride, post annealing was performed on samples. Later on, Cu_xTe buffer layer was formed by Bromine etching and copper thin film deposition. Finally, degradation modeling was carried out by

SCAPS using the parameters derived from our experiment.

4.1 Evaporated CdTe Thin Films

4.1.1 Basic Principle of High Vacuum Thermal Evaporation

High Vacuum Thermal Evaporation (HVTE) is one of the common methods to deposit CdTe layer as it is easier to control [1]. The pressure used for HVTE is usually below 10^{-5} Torr in all of our experiments. Variations of thickness were reported by using the HVTE since the thickness can be approximated by calculating the CdTe evaporated and the evaporation time. The approximation is done according to the kinetic theory of gases [2].

The number of evaporated gas atoms N_0 that strike the substrate follows [2]:

$$N_0 = 3.5 \times 10^{22} \times \frac{P_0}{MT^{1/2}} \ (\text{particles cm}^{-2}\ \text{s}^{-1}) \qquad (4.1)$$

where P_0 is the vapor pressure in Torr of the evaporated gas atoms, M is the molecular weight of the evaporated materials and T is the temperature of the substrate. Molecular weight of CdTe is

$$M_{Cd} + M_{Te} = 112.41 + 127.6 = 240.01 \qquad (4.2)$$

Assumptions along with Eq. (4.1) and (4.2) embrace the fact that the film formed from the condensation of the adatoms. Moreover the theory was made based on the conditions that the distance between the evaporation sources to the substrate is 15 cm and the substrate temperature is similar to that of chamber. Thus, the evaporation source is chosen as center with 15 cm as the radius of the sphere. Since

the size of CdTe solar cells is $1 \times 1\, cm^2$, a small area compare to the sphere, it is reasonable to deduce that the as-deposited films are with good uniformity. Suppose all the evaporated atoms impinge on the substrate without bouncing off to other direction missing the substrate, the thickness of the film can be estimated to be:

$$d = \frac{N_0 \times \tau}{n} \qquad (4.3)$$

for n the atomic density of CdTe and τ the deposition time.

Therefore, the thickness of deposited CdTe layer can be briefly calculated.

4.1.2 CdTe Thin Films Grown by High Vacuum Thermal Evaporation

In this project, CdTe fabrication by High Vacuum Thermal Evaporation was examined. The substrate used is common laboratory grade glass slide. The glass slide was first cleaned through ultrasonic cleaner in isopropyl, acetone and alcohol for ten minutes, respectively. Then it was cleaned thoroughly by rinsing it with distilled water. After the glass slide was dried by nitrogen gas, it was put into the substrate holder in the evaporator. The temperature of the holder can be precisely controlled in the range from room temperature to 300 ℃. Then, CdTe was deposited by High Vacuum Thermal Evaporator as presented in Fig. 4-1. The evaporation procedure starts when the pressure reaches 5×10^{-3} Pa.

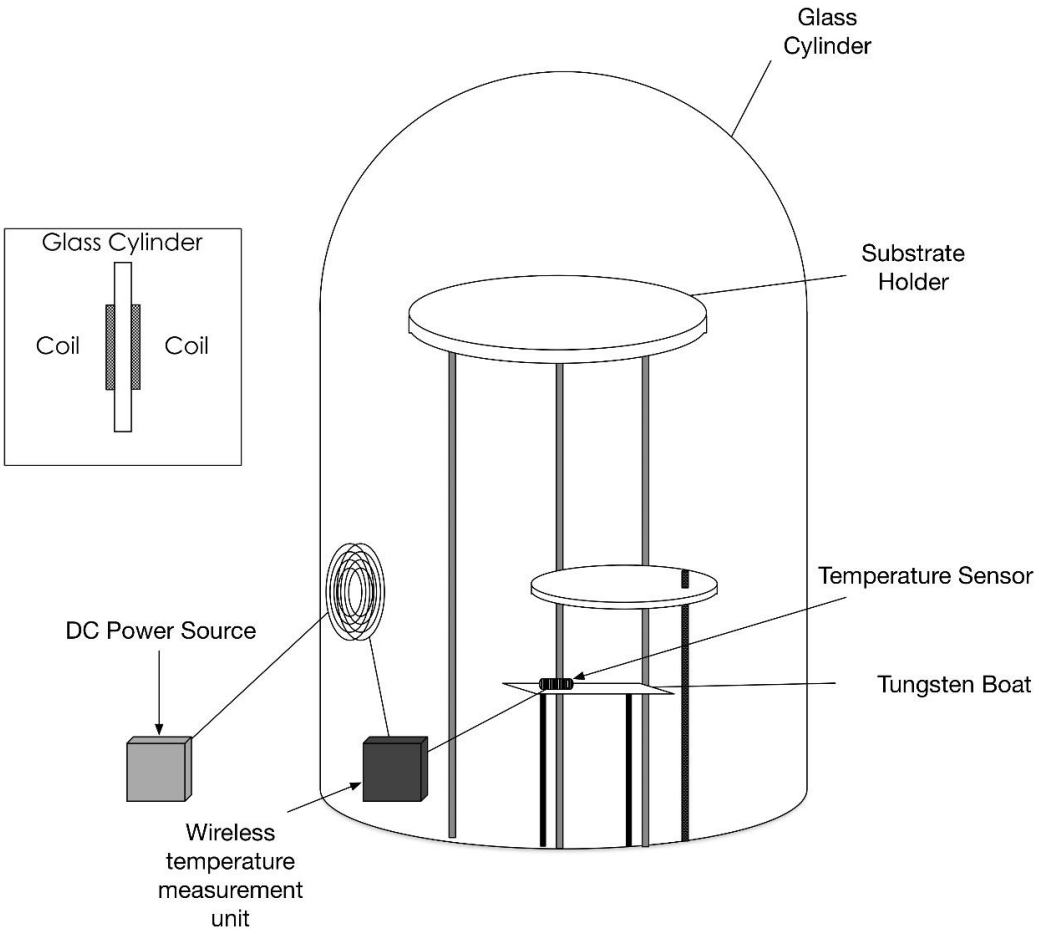

Fig. 4-1 Sketch of the chamber of high vacuum thermal evaporator used in the experiments.

Fig. 4-1 demonstrates the diagram of the HVTE device. It should be noted that a tungsten boat is being used instead of a ceramic bowl together with tungsten filament. This design enables the exploitation of better heating uniformity since that CdTe powder is uniformly spread on the tungsten boat. The conditions of the evaporation and observation include:

a. Decrease the pressure down to 5×10^{-3} Pa

b. heat the substrate holder to the setting value

b. Move the vapor blocker to protect any organic or unwanted substances being

evaporated and adsorbed onto the substrate

c. The vapor blocker also used to ensure the steady evaporation rate

d. Increase the current flow until reaching target temperature

e. Move away the vapor blocker

f. Control the deposition time according to the time value calculated form formula (4.1), (4.2), and (4.3).

Using the method described above, CdTe thin films were deposited at different substrate temperatures for 50 minutes. Fig. 4-2 illustrates that the grain sizes of each films are similar at various substrate temperatures. The grain size of peak (111) is in the range of 60-100 nm, much lower than those obtain by Closed-Space Sublimation (CSS) technology. Compare to the micron scale grain size in CSS grown thin film, smaller grain size is obtained in the HVTE grown thin film at the relatively low substrate temperature.

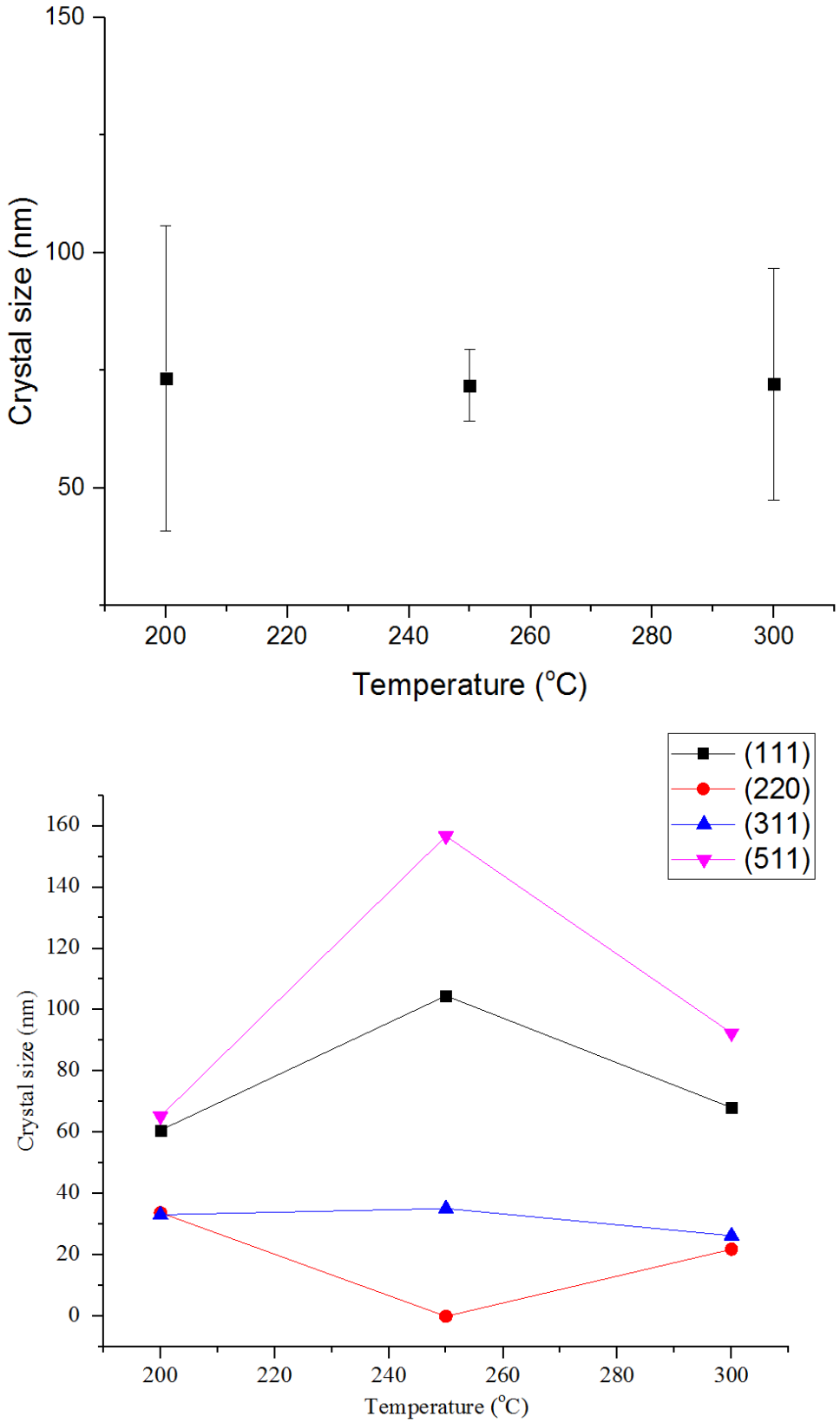

Fig. 4-2 Grain size of CdTe prepared on glass under different substrate temperatures

4.1.3 Wet $CdCl_2$ Treatment

It has been demonstrated that chloride ion acts as a fluxing agent that enhances the atom mobility of CdTe film during annealing process [3]. $CdCl_2$ was commonly used in the post-deposition treatment process to increase grain size and enhance electrical properties of CdTe thin film. To study the recrystallization of CdTe during post-annealing process, 3 micron thick CdTe thin films were evaporated on glass at 250 ℃. The samples were divided into two group: one group was treated with $CdCl_2$ in air, the other group was annealed without $CdCl_2$ treatment in air. The manufacturing process of the first group was depositing a thin $CdCl_2$ layer on the sample in $CdCl_2$-methanol saturated solution by dip coating method. After that, the samples were put into the tube furnace for annealing for 15 minutes at 300 ℃, 350 ℃, 450 ℃, and 550 ℃, respectively. The second group is annealed in tube furnace without dip coating $CdCl_2$ process. After cooling down to room temperature, samples were characterized by XRD.

Fig. 4-3 demonstrates the annealing effect on CdTe thin film without $CdCl_2$ treatment. It can be found from the figure that CdTe thin film has a strong (111) crystal direction. The intensity of (111) did not have a significant change before and after annealing. However, the increase in temperature brings the crystal orientations of (220), (311), (400), (331) and (422). When temperature reaches 350 ℃, crystal orientation (511) can be detected. Also, the grain size increase to 270 nm, four times larger than that at 250 ℃. The grain size drop to 70 nm when annealing temperature increase to 450 ℃ or higher. This phenomenon could be explained by the evaporation

of CdTe at high temperature leading to eliminate of CdTe films at the grain boundary.

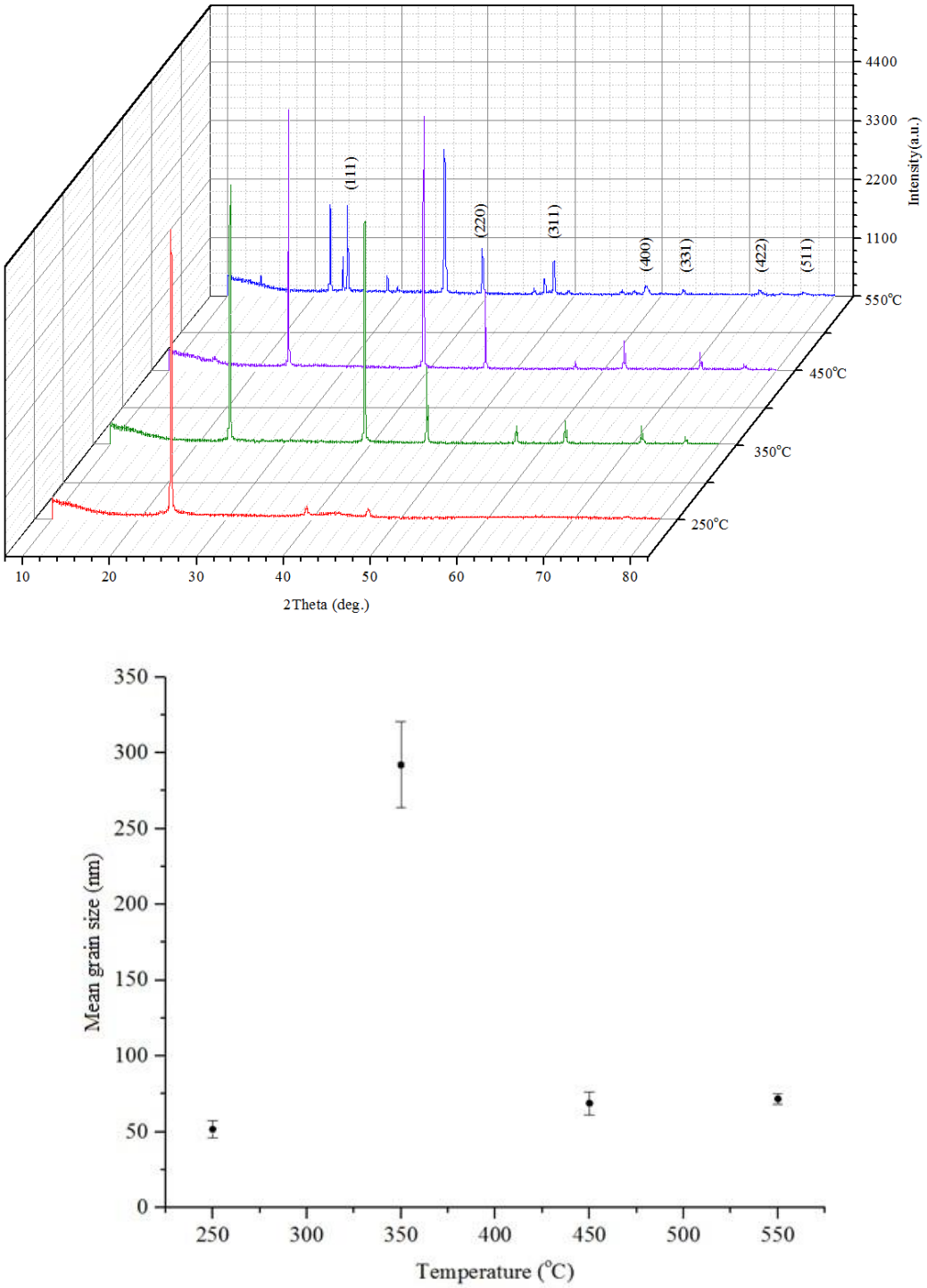

Fig. 4-3 CdTe thin films annealed at various temperatures without $CdCl_2$.

For thin films annealed with $CdCl_2$, the grain size increase from 30 nm in 250 ℃ to 110nm in 350 ℃ and 100 nm in 450 ℃. This result in agreement with those reported in literature [4-6]. For small grain size, enough energy can be provided for recrystallization at heating stage. Therefore, the grain size could increase significantly. For CdTe thin films in micron scale grain size deposited by CSS, no grain growth could be observed after $CdCl_2$ assisted annealing.

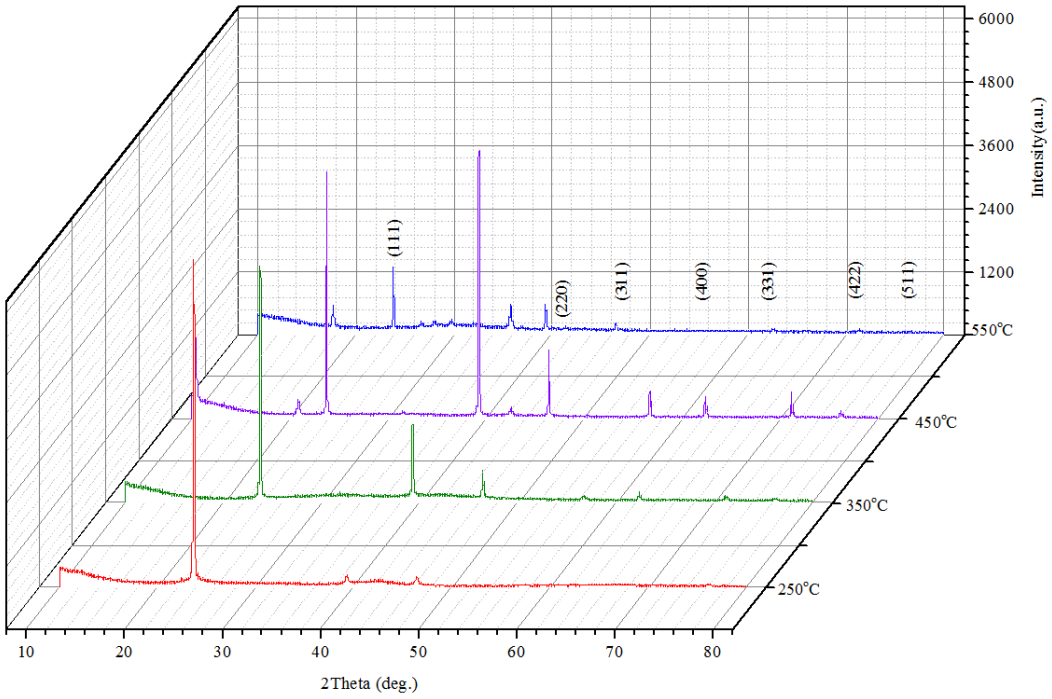

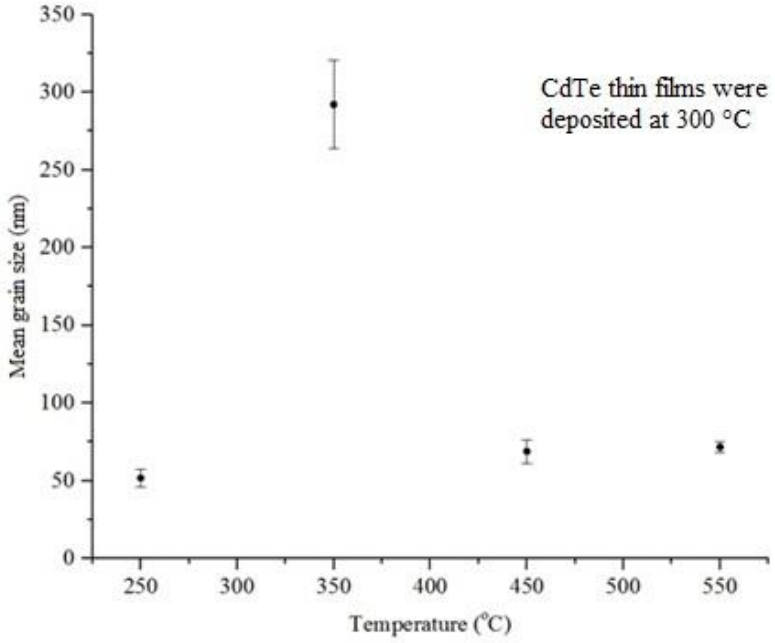

Fig. 4-4 XRD of CdTe thin films annealed at various temperatures with $CdCl_2$.

There is an interesting phenomenon in Fig. 4-5. By comparing Fig. 4-5 (a) and (b), we can found that the signal of oxide is strong in the $CdCl_2$ treated thin film. Yet, no oxidation can be detected in 350 ℃. This illustrates that the exist of $CdCl_2$ favor the generation of oxide on the surface of CdTe film.

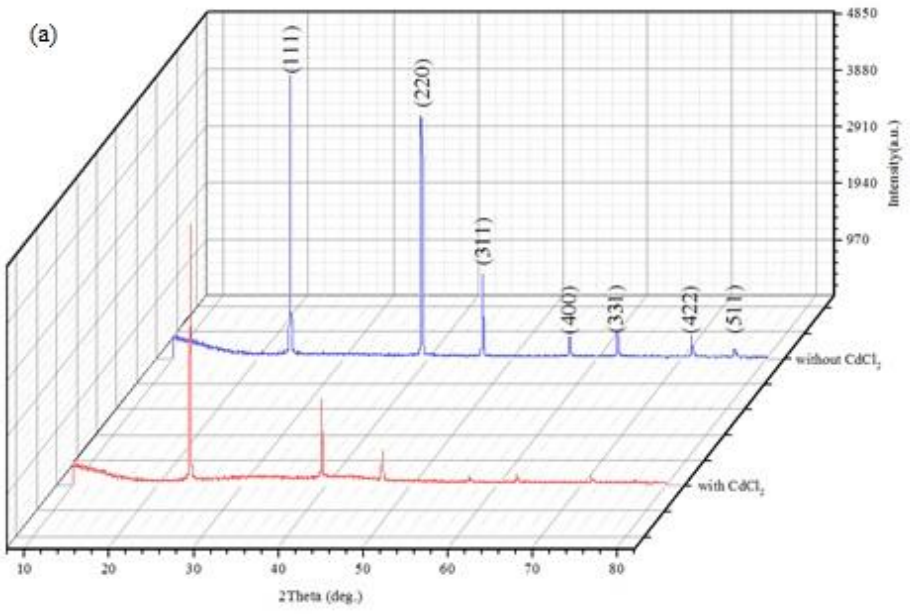

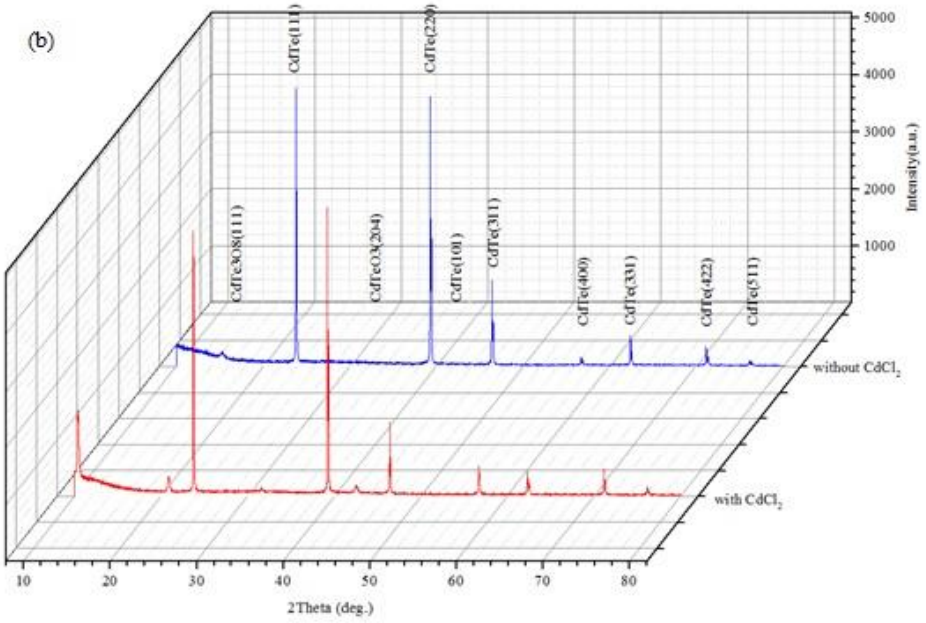

Fig. 4-5 XRD of CdTe thin films annealed at (a) 350 ℃ (b) 450 ℃.

Fig. 4-6 provides another evidence. The main oxides generated during heat treatment are: $CdTeO_3$, Te_2O_5, and CdO. The reason is a high temperature increase the energy of surface atoms, which promotes the oxidation. For the mixture of CdTe-$CdCl_2$-$CdTeO_3$, the melting point decreases with the increasing of $CdTeO_3$ concentration. Thus, at a high temperature, the chemical on the surface of CdTe thin film is in a melting state. When the sample is cooling down to room temperature, the compressive stress on the thin film will results in cracks of thin film. Hence, the best $CdCl_2$ treatment temperature should be in the range of 350-450 ℃.

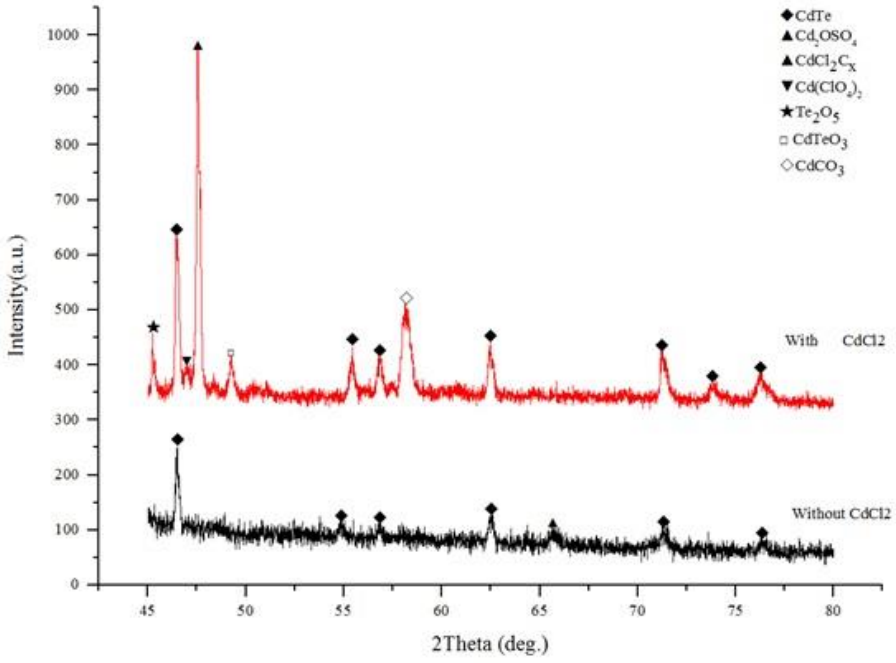

Fig. 4-6 XRD of CdTe thin films annealed at 550 ℃.

4.2 Deposition of Cu_xTe Back Contact Layer

4.2.1 Basic Principle of Br-Methanol Etching Process

As mentioned in chapter one, etching process is crucial for removing the oxide on the surface and obtaining a Te rich surface [7]. Hence, etching process cannot be neglected during back contact formation. Among various etchant, Br-methanol is a common and effective etching solution. When CdTe thin film was immersed in the Br-methanol solution, Br_2 particles absorbed on the surface of CdTe crystal. The reaction between Br and CdTe is:

$$Br_2 + Te^{2-} \rightarrow 2Br^- + Te^0 \qquad (4.3)$$

After reaction, Cd ion became free ions and dissolved in the etching solution. Therefore, a Te rich film can be obtained by such a etching process.

4.2.2 Etched-CdTe Thin Film Characterization

In these experiments, CdTe films were deposited on glass slide at substrate temperature of 300 ℃ following with $CdCl_2$ post-annealing treatment at 400 ℃. DI water was used to rinse the residual $CdCl_2$ on CdTe thin film. Finally, the sample was dried by nitrogen. The samples were treated in Br-methanol solution with different concentrations.

After etching with Br-methanol solution (1:1000), the sample shows gray color. In addition, the film shown hydrophobic after etching. The hydrophobic surface demonstrates that the microstructure of the surface has been changed. For further investigation, SEM has been used to observe the thin film surface. As shown in Fig. 4-7, the surface become smooth after 20 seconds treatment in Br-methanol solution. When the etching time is increased to 40 seconds, the crystal boundary become larger and deeper. It can be deduced that longer etching time will brings in shunt pass in the film.

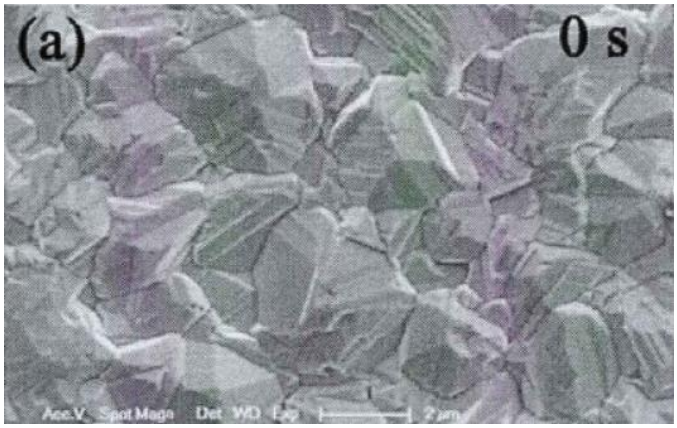

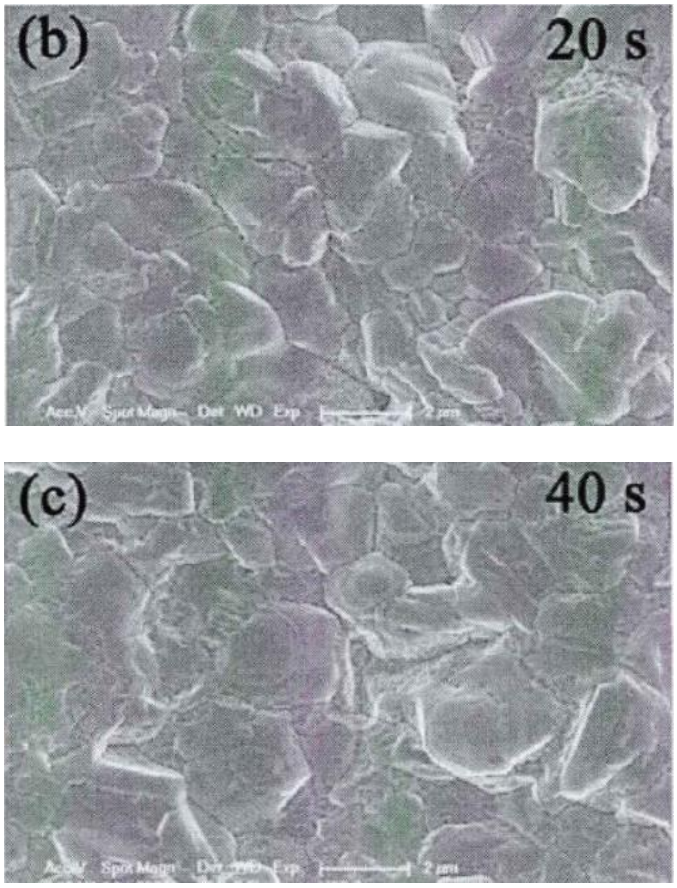

Fig. 4-7 The surface of Br-methanol treated CdTe thin films characterized by SEM: (a) no etching; (b) etched for 20 seconds; (c) etched for 40 seconds.

4.2.3 Formation of Cu_xTe

The CdTe sample was prepared at 250 ℃ on glass slide following with an $CdCl_2$ post-annealing at 450 ℃ for 15 minutes. Then, the sample was rinsed by DI water to remove the $CdCl_2$ residue before Br-methanol etching process. After being treated with Br-methanol solution for 20 seconds, the sample was rinsed with DI water and placed in the chamber of evaporator. 5 nm copper film was evaporated on the sample prior to annealing at 200 ℃ for 15 minutes to form Cu_xTe layer. It is notable that copper deposition and sample annealing must take place in vacuum environment. The reason is a few nanometers copper is very easy to be oxidized when

exposed to air at room temperature.

4.3 Stability of CdTe Solar Cells with Various Back Contact Buffer Layers

4.3.1 Role of Copper on CdTe Solar Cells

In CdTe solar cells, Cu is considered as an important back contact dopant. However, large amount of copper results in severe device degredation. As a back contact buffer layer, copper is used in the form of compound (Cu_xTe) and dopant (copper doped ZnTe and Copper doped graphite) [8-12]. However, copper ion is a fast diffuser. It has been revealed that copper will diffuse into CdTe film and form donor defect Cu_i, accepter defect Cu_{Cd}, and complexity Cu_{Cd}-Cu_i [13]. Cu_i is a deep level defect and is gathering at the interface of CdS/CdTe. The deep level defect acts as carrier recombination center further resulting in solar cell degradation. Therefore, it is necessary to investigate the ion-diffusion-caused degradation.

4.3.2 CdTe Solar Cells Degradation Model

Basically, copper ions in the CdTe thin films form new defects, which act as shallow dopant or deep level defects. Shallow dopants increase the doping concentration of the thin film. In turn, deep level defects increase the recombination rate in the CdTe.

Linear or quadratic defect generation rate can be found in nonequilibrium semiconductor. For simplicity, the linear rate is considered. The defect concentration

is given by

$$\frac{dN}{dt} = \alpha p - \beta N \qquad (4.4)$$

where N is the defect concentration; p is the hole concentration in CdTe thin film; α is defect generation rate; and β represent defect annihilation rate. However, at the beginning of solar cell degradation, the concentration of copper is far from saturated. Hence, the term with β can be neglect.

Hence, the defect concentration of next stage can be expressed by the combination of the defect concentration on current stage and hole concentration:

$$p(i+1) = p(i) + (N_{i+1} - N_i)/\alpha dt \qquad (4.5)$$

In quasi stationary approximation, the variation of hole concentration is zero. Therefore, hole concentration can be expressed as:

$$\frac{dn}{dt} = G - C_r N p \approx 0 \qquad (4.6)$$

And derived

$$p = \frac{G}{C_r N} \qquad (4.7)$$

where G is the electron-hole pair generation rate, C_r is the recombination coefficient.

Combining equation (4.4) and (4.6), we can have defect generation rate:

$$N = N_0\left[1 + \frac{t}{N_0^2 C_r / 2\alpha G}\right]^{1/2} \qquad (4.8)$$

4.3.3 Effects of Cu_xTe Back Contact Buffer Layer on CdTe Solar Cells

According to equation 4.7, defect concentration changes over time. By inserting the defect density in various time step into the CdTe solar cell model, the parameters

can be calculated from the SCAPS simulator. The parameters used in simulation were listed in Table 4-1.

Table 4-1 Parameters of each layer for SCAPS simulation

	ZnO:Zr	**CdS**	**CdTe**	**Cu_xTe**
Thickness(nm)	500	25	3000	100
bandgap(eV)	3.6	2.4	1.5	0.85
electron affinity(eV)	4	4	3.9	3.82
dielectric permittivity (relative)	9	10	9.4	10
CB effective density of state (cm^{-3})	2.20E+18	2.20E+18	8.00E+17	2.20E+18
VB effective density of state (cm^{-3})	1.80E+19	1.80E+19	1.80E+19	6.50E+20
electron thermal velocity (cm/s)	1.00E+07	1.00E+07	1.00E+07	1.00E+07
hole thermal velocity (cm/s)	1.00E+07	1.00E+07	1.00E+07	1.00E+07
electron mobility(cm/Vs)	1.00E+02	1.00E+02	3.20E+02	1.00E+02
hole mobility (cm/Vs)	2.50E+01	2.50E+01	4.00E+01	1.62E+01
Shallow uniform donor desity $N_D(1/cm^3)$	1.00E+17	1.10E+18	0.00E+00	0.00E+00
Shallow uniform acceptor desity $N_A(1/cm^3)$	0.00E+00	0.00E+00	2.00E+14	

Degradation of CdTe solar cells had been demonstrated in Fig. 4-8. In Fig. 4-8 (a), short circuit current increase at the very beginning time steps, following with a slight decrease. This phenomenon can be explained by the process of Copper ion diffusion in CdTe solar cells. Initially, copper ions diffuse to the CdTe thin film and act as a shallow dopants. The hole concentration in CdTe thin film is thus increase, which results in an increase in built-in potential voltage. Then, copper ions diffuse to the interface of CdS/CdTe which act as deep level defects. Obviously, the increase in deep level defects leads to high recombination rate and thus low short circuit current density. Open circuit voltage did not change significantly. This is in agreement with the report in the literatures. The reduction in solar cell efficiency is mostly attributed

to the loss in fill factor. The decrease in fill factor is probably due to the increase in series resistance. Since copper ions diffuse from the Cu_xTe layer, small amount of copper in the buffer layer will lead to deterioration of ohmic contact at the back electrode. The increase of ohmic value or the formation of Schottky diode at the back contact will bring in loss of fill factor.

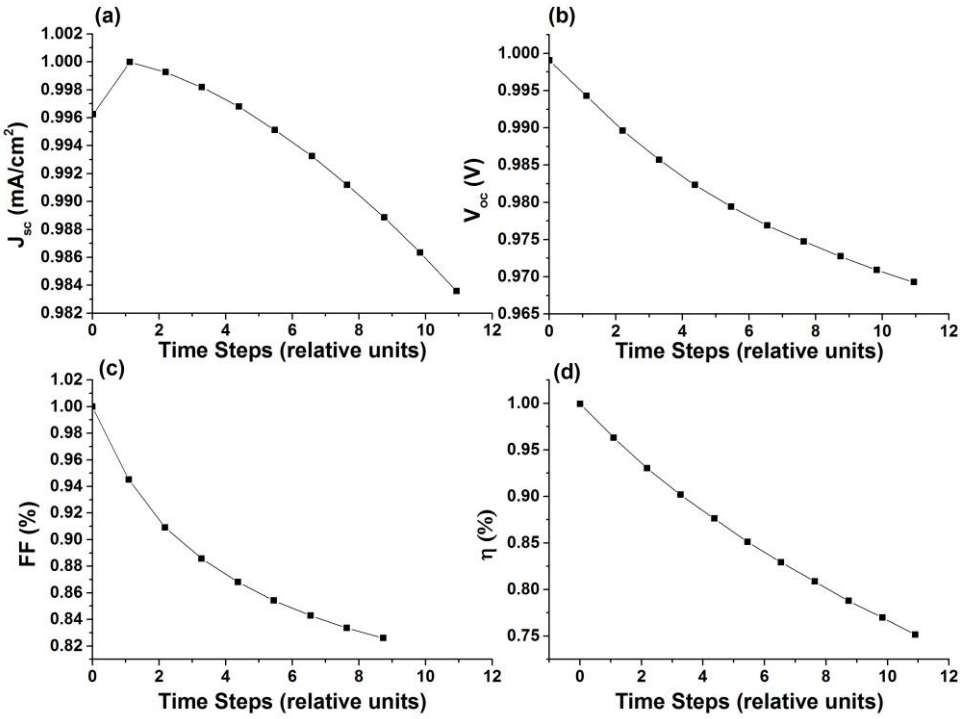

Fig. 4-8 Degradation of CdTe solar cells with Cu_xTe as back contact buffer layer.

References for the Chapter

1. Schor, C.; Imt-Bucharest, I.-B., *Vacuum deposition of CdS thin films for photoconductive cells*. 2001; p 301-304.
2. Jaber, A. Y.; Alamri, S. N.; Aida, M. S.; Benghanem, M.; Abdelaziz, A. A., Influence of substrate temperature on thermally evaporated CdS thin films properties. *Journal of Alloys and Compounds* **2012,** 529, 63-68.
3. Dharmadasa, I., Review of the CdCl2 Treatment Used in CdS/CdTe Thin Film Solar Cell Development and New Evidence towards Improved Understanding. *Coatings* **2014,** 4, (2), 282.
4. Balcioglu, A.; Ahrenkiel, R. K.; Hasoon, F., Deep-level impurities in CdTe/CdS thin-film solar cells. *Journal of Applied Physics* **2000,** 88, (12), 7175-7178.
5. Chou, H. C.; Rohatgi, A.; Jokerst, N. M.; Kamra, S.; Stock, S. R.; Lowrie, S. L.; Ahrenkiel, R. K.; Levi, D. H., Approach toward high efficiency CdTe/CdS heterojunction solar cells. *Mater. Chem. Phys.* **1996,** 43, (2), 178-182.
6. Agostinelli, G.; Batzner, D. L.; Burgelman, M., A theoretical model for the front region of cadmium telluride solar cells. *Thin Solid Films* **2003,** 431, 407-413.
7. Dobson, K. D.; Paulson, P. D.; McCandless, B. E.; Birkmire, R. W., The dynamics of cadmium telluride etching. In *Compound Semiconductor Photovoltaics*, Noufi, R.; Shafarman, W. N.; Cahen, D.; Stolt, L., Eds. 2003; Vol. 763, pp 107-118.
8. Albright, S. P.; Jordan, J. F.; Ackerman, B.; Chamberlin, R. R., DEVELOPMENTS ON CDS/CDTE PHOTOVOLTAIC PANELS AT PHOTON ENERGY, INC. *Solar Cells* **1989,** 27, (1-4), 77-90.
9. Gessert, T. A.; Mason, A. R.; Sheldon, P.; Swartzlander, A. B.; Niles, D.; Coutts, T. J., Development of Cu-doped ZnTe as a back-contact interface layer for thin-film CdS/CdTe solar cells. *Journal of Vacuum Science & Technology*

a-Vacuum Surfaces and Films **1996,** 14, (3), 806-812.

10. Uda, H.; Ikegami, S.; Sonomura, H., COMPOSITIONAL CHANGE OF THE AU-CU2TE CONTACT FOR THIN-FILM CDS/CDTE SOLAR-CELLS. *Japanese Journal of Applied Physics Part 1-Regular Papers Short Notes & Review Papers* **1990,** 29, (3), 495-496.
11. McCandless, B. E.; Qu, Y.; Birkmire, R. W.; Ieee, A treatment to allow contacting CdTe with different conductors. In *1994 Ieee First World Conference on Photovoltaic Energy Conversion/Conference Record of the Twenty Fourth Ieee Photovoltaic Specialists Conference-1994, Vols I and Ii*, 1994; pp 107-110.
12. Chou, H. C.; Rohatgi, A.; Thomas, E. W.; Kamra, S.; Bhat, A. K., EFFECTS OF CU ON CDTE/CDS HETEROJUNCTION SOLAR-CELLS WITH AU/CU CONTACTS. *Journal of the Electrochemical Society* **1995,** 142, (1), 254-259.
13. Kucys, E.; Jerhot, J.; Bertulis, K.; Bariss, V., COPPER IMPURITY BEHAVIOR IN CDTE-FILMS. *Physica Status Solidi a-Applied Research* **1980,** 59, (1), 91-99.

Chapter 5: Graphene as a Back Contact Buffer Layer

Fast diffusers, such as Cu, Al or Au, were considered as the significant reason for solar cell instability. Device degradation was increased by the increase of copper concentration at the back contact, while copper substitution at the CdS/CdTe interface act as shallow dopant and is beneficial for device performance [1]. However, some of the buffer materials, including Cu_xTe, ZnTe:Cu and Cu loaded graphite paste, do not meet the requirement for long term stability.

The Cu-based buffer materials have matched work functions with CdTe absorber which facilitate the holes transportation from CdTe thin film to the back electrode. Since the interstitial atoms of copper diffuse into CdS/CdTe at high diffusion rates, those Cu-based materials show unstable energy bandgap. Also, the extra interstitial coppers act as deep-level dopant and result in short carrier lifetime and low power conversion efficiency. It is reported that Cu_xTe (x=1~2) is an unstable chemical except $Cu_{1.4}Te$. The large amount of copper diffuse from the initial deposited Cu_xTe along the grain boundary, resulting in a poor shunt resistance for the cells [2]. For ZnTe:Cu, the mechanism is difference. Since the copper amount in the CdTe is low, a small amount of copper diffusion increases the carrier concentration in the CdTe thin film and simultaneously enhance the open circuit voltage and solar cells

efficiency [3]. The problem is the diffusion of copper leading to the change of buffer layer work function and the increase of Schottky barrier at the back surface field. The silver or nickel electrode is generally believed to fail to form back electrode in CdTe solar cells. The device using Ag back contact become susceptible for degradation due to the rapid diffusion of Ag ion. And solar cells using Ni as back contact result in the loss of fill factor due to the Ni_3Te_2 phase formation. To minimize the degradation, a Cu loaded graphite layer was introduced between the CdTe thin film and Ag or Ni electrode to enhance the device stability by limiting the diffusion of Ag and formation of Ni_3Te_2 [4]. However, the Cu loaded graphite layer was plagued by the diffusion of copper ion. Since the Cu loaded graphite layer serve as a source of Cu, Cu ions diffuse toward the CdS/CdTe surface in the course of subsequent annealing and photoinduced stress. A modest degradation around 15% was observed in the CdS/CdTe/graphite:Cu/Ag structure [4]. To ensure the stability of solar cells, Cu-free buffer materials such as Sb_2Te_3 and MoO_x are developed.

Romeo et al. first introduced Sb_2Te_3/Mo back contact into CdS/CdTe solar cells with great success [5]. The novel solar cell exhibited power conversion efficiency of 14.6%. After 6 months test under 60 ℃ and 10 suns irradiation in open circuit condition, it shows small degradation [6]. It is reported that CdTe/ Sb_2Te_3 is in thermodynamic equilibrium in a chemical point of view. Therefore, no reaction occur between CdTe and Sb_2Te_3 layer and thus contributing to long term stability. Based on thermodynamic consideration, it was deduced that the instability of Sb_2Te_3 based solar cells are highly dependent on the applied metal electrode. When Ni film is deposited

on the Sb_2Te_3, spontaneous reactions occurs at the interface of Sb_2Te_3/Ni and forms $NiTe_x$, $NiSb_x$ and Sb_2Te_3 [7]. Thus, the ohmic contact is destroyed. Conversely, Sb_2Te_3/Mo is found to be stable. CdTe/ Sb_2Te_3/Mo is proved to be a stable back contact system for long term stability consideration [8].

MoO_x is another material widely used as Cu-free buffer layer in CdTe solar cells. CdTe solar cells fabricated with MoO_x/Ni back contact system achieved high conversion efficiency of 12.2% with an optimized MoO_x thickness of 40 nm [9]. Since MoO_x is an insulating material, the series resistance is in proportion to the thickness of MoO_x. Therefore, the thickness of MoO_x will affect the device efficiency, significantly. In addition, MoO_x is highly sensitive to surface contamination. It was demonstrated that the work function of as-deposited MoO_x will dramatically reduce after air exposure from 6.80 eV to 5.24 eV [9]. It is also reported that MoO_x buffer served as diffusion barrier for Mo or Ni electrodes. However, MoO_x is least stable when depositing associated with metal like Al. From a thermodynamic point of view, the large standard enthalpy Al_2O_3 formation favor the abstraction of oxygen atom from chemical MoO_x [10, 11]. Considering the mineral reserves in earthcrust, elements including Te, Sb, Mo, and Ti limit the terawatt deployment. The development of stable buffer layer with low cost and abundance still have a long way to go.

Carbon-based nanomaterials have recently attracted tremendous attention due to their abundance, exceptional electrical properties and chemical stability. Multilayer graphene sheet has ultra-low electrical conductivity perpendicular to the

CdTe/graphene interface. Also, graphene has a perfect hexagonal carbon lattice and exceptional in-plane conductivity, and high mechanical strength. In this context, graphene is considered as the potential replacement for conventional buffer materials.

CdTe solar cells fabricated along with reduced graphene oxide (r-GO), pristine graphene (PG) and boron doped graphene (BG) highlight that graphene and its derivative can serve as efficient back contact materials [12]. Comparing with the chemically reduced exfoliated graphene oxide sheet, graphene sheet prepared by chemical vapor deposition (CVD) shows better in-plant electrical conductivity. Yet, the BG cell had the highest efficiency of 7.86% [12]. The reason for good performance is that graphene doped with 2 at.% of boron increase the carrier concentration in the valence band of the graphene together with a shift in Fermi level. This indicates that boron doped graphene can serve as a good back contact layer [13]. Impermeable graphene sheet may also serve as metal ion diffusion barrier in CdTe solar cells. It should be aware that graphene was used as anti-corrosion coating [14] and barrier membrane for hazardous ions [15]. Hence, it is necessary to investigate the permeation of graphene to metal ions, e.g., copper, silver, nickle ions from the metal electrode.

5.1 LPCVD Synthesized Graphene Using Copper Catalyst

Various metals have been used as graphene synthesis catalyst, including Cu, Ni, Co, Ru, Ir, etc. [16-19]. The growth conditions and merits have been listed in Table

5-1.

Table 5-1 Comparison of different metal catalysts.

Metal catalyst	Cu	Ni	Ru	Ir	Pt
Crystal orientation	(1 1 1), (200)	(1 1 1)	(0001)	(111)	(111)
Growth mechnism	Surface adsorption-dehydrogenation-growth	Segregation and precipitation	Segregation and precipitation	Attachment of C-atom clusters	Chemisorption/deposition growth mechanism
Disadvantages	wrinkles on the graphene and structural defects at the joints of	Various thicknesses and numbers of grain boundaries	Large lattice mismatch possess a corrugated surface	Form several graphene orientations	Cost high
Advantages	Large areas, high quality	Low cost, at a large scale	Surface is most stable for hcp structure:	Well-aligned with the substrate	Wrinkles are useful
Thickness of substrate	25μm	Above SiO2/Si (300nm)	0.220nm	>3.2nm	> 568.2 nm
Layer number of graphene	1-2	3-8	1-2	1-3	1-3
Reaction Temperature(°C)	1000	900	1000	1077-1257	877-1027
Carbon solubility	<0.001 atomic %)	~0.6 at. %	~0.34 at. %	low	low
Substrate	No	SiO2/Si	No	Si(100)	No
Interaction with graphene	strong	strong	strong	Weak	weak
Reference	[16, 17, 20]	[16, 21]	[22, 23]	[21, 22, 24, 25]	[22, 26]

Among all those catalysts, Cu and Ni are most popular due to their low cost and mature synthesis technologies from carbon nanotube growing research. However, the growth mechanism of Cu and Ni are different. By sequential depositing carbon isotope, it has been revealed that the growth of graphene on Ni film surface involves carbon absorption and desorption process. Since Ni has high carbon solubility, a low cooling process will results in multilayer graphene or even amorphous carbon. The quality of graphene and number of layers were determined by cooling rate.

In comparison, Graphene growth in Cu is not absorption-desorption method. The growth mechanism of Cu is regarded as adsorption-dehydrogenation-growth process, as shown in Fig. 5-1.

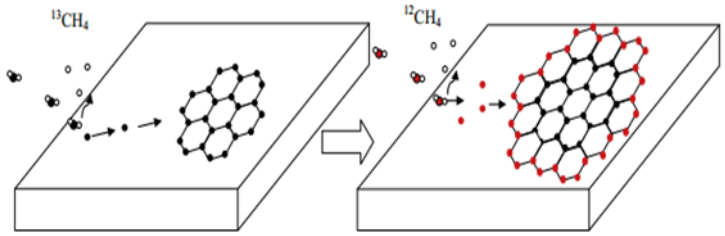

Fig. 5-1 The surface growth mechanism. Black particles indicate 13C isotope, red particles indicate 12C isotope and white particle indicates hydrogen atoms. *Reproduce from ref. [20]*.

Essential growth steps of graphene on Cu foil are: 1) hydrocarbon is catalyzed by Cu and decompose, 2) carbon atoms nucleate and grow into graphene. 3) lateral extension of graphene nucleus attached and form graphene islands [17]. The growth stops after the surface of copper is fully covered with graphene.

5.1.1 Treatment of Copper

Graphene growth on Cu surface is adsorption-dehydrogenation-growth method. Generally, copper assisted graphene growth process can be divided into two steps, namely nucleation and expansion of nucleus domains, as shown in Fig. 5-2.

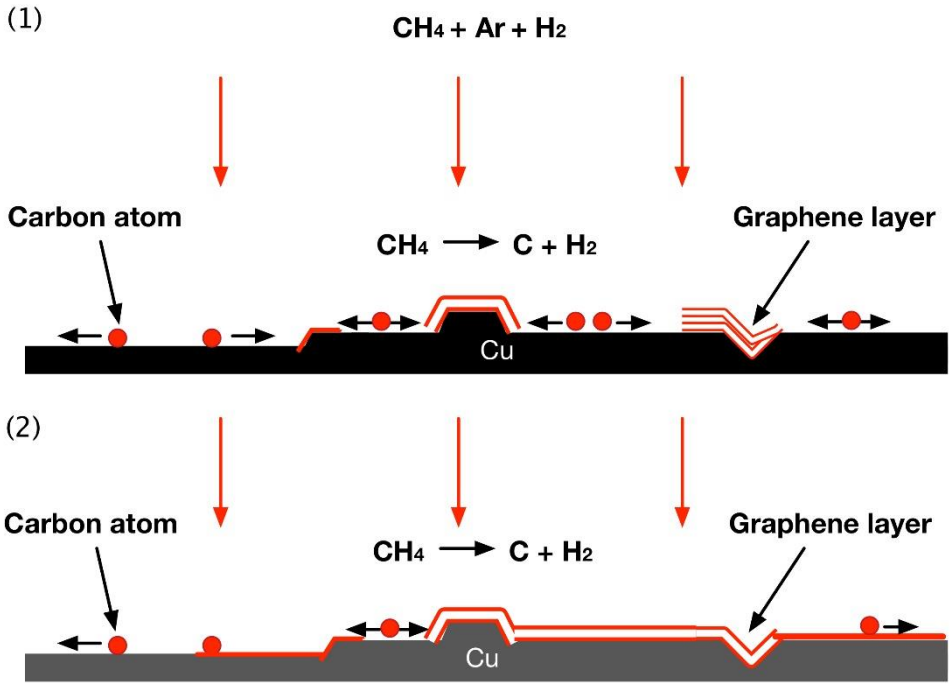

Fig. 5-2 Graphene growth mechanism under 1000 ℃, (a) methanol decompose on the surface of Cu foil, the carbon atoms move around on the copper surface. Then they nucleate on the defect position and grow to a small graphene nucleus; (b) laterally extension of graphene nucleus to graphene islands. When graphene islands keep extension and connect together, the surface of the Cu foil is covered by graphene sheet. Since methanol cannot reach the catalyst, no methanol particles are decompose afterwards.

The density of the defect on copper surface determines the number of graphene nucleus. In other words, low defect density on copper foil results in large graphene grain size. Considering the carrier scattering effect of the grain boundary, large grain size of graphene is crucial for high carrier mobility and good electrical conductivity

[27]. Therefore, in order to obtain high quality graphene films, it is necessary to obtain Cu film with large grain size to minimized point defects and stacking fault. Pre-treatment process and hydrogen relief annealing are two methods that are widely used to obtain high quality copper foil [27].

The commercial available copper foil (Alfa Aesar, #13382) is not smooth enough, numerous rolling strips can be seen under optical microscopy. To eliminate the rolling strips, two methods, including chemical etching and electrochemical corrosion were adopted.

In our case, $FeCl_3$-HCl-H_2O solutions were used as chemical etchant to eliminate the rolling strips. The copper foil (Alfa Aesar, 25 μm) was first cut into small pieces. Then, the copper pieces were cleaned by isopropyl alcohol, acetone, and DI water for 20 minutes in ultrasonic machine, respectively. Subsequently, nitrogen were used to dry the copper pieces. Later on, fresh copper pieces were treated by the $FeCl_3$-HCl-H_2O solutions followed with rinsing in DI water for three times. The untreated and treated copper foils were listed in Fig. 5-3.

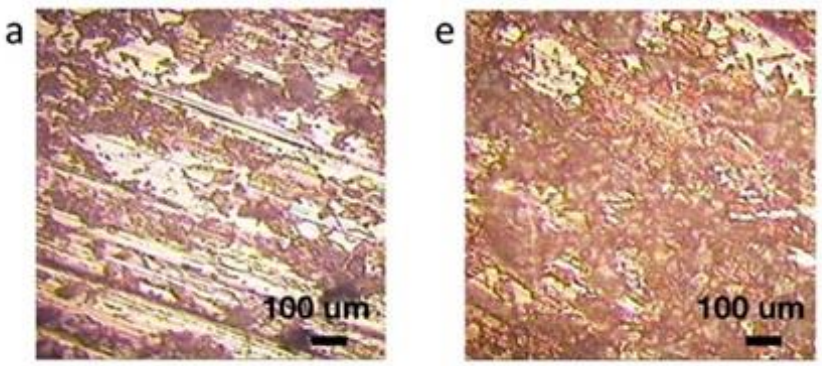

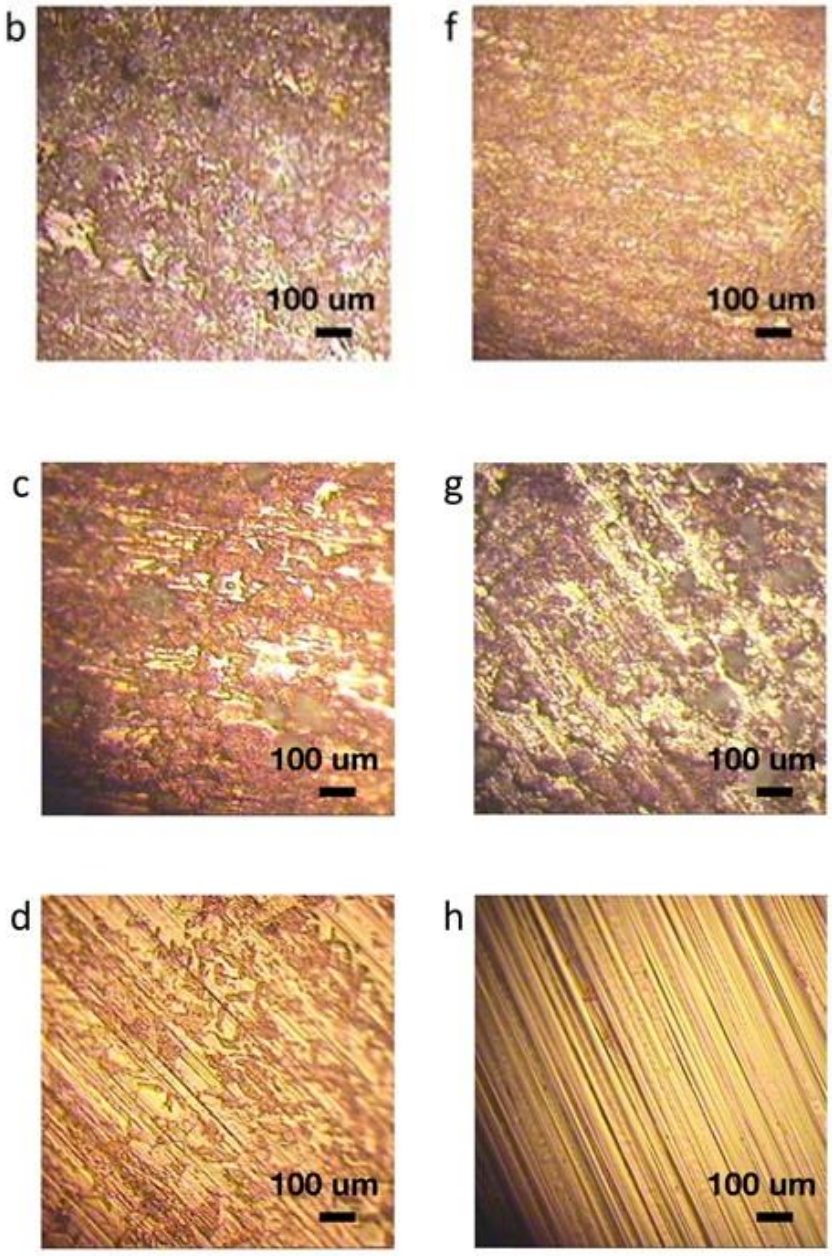

Fig. 5-3 Optical microscopic images of the surface of the copper foils cleaned by $FeCl_3$-HCl-H_2O solutions under 20 ℃ with various treatment condition: (a) 1 g: 1 ml: 100 ml, 1 minute; (b) 5 g: 1 ml: 100 ml, 1 minute; (c) 5 g: 5 ml: 100 ml, 1 minute; (d) 1 g: 5 ml: 100 ml, 1 minute; (e)1g: 1 ml: 100 ml, 10 minutes; (f) 5 g: 1 ml: 100 ml, 1 minute, ultrasonic cleaning; (g) 5 g: 5 ml: 100 ml, 1 minute, under 40 ℃; (h) copper foil before cleaning process.

Fig. 5-3 illustrates the surface morphology of the copper under different treatment conditions. It can be found that the strip elimination effect is closely related

to the concentration of ferric chloride. Low ferric chloride concentration results in poor strip elimination, as shown in (a), (d), (e). The best sample was obtained from decent ferric chloride concentration solution under ultrasonic-assisted condition, as shown in (f). While, higher temperature (40 ℃) did not have a significant effect on etching, as demonstrate in (g).

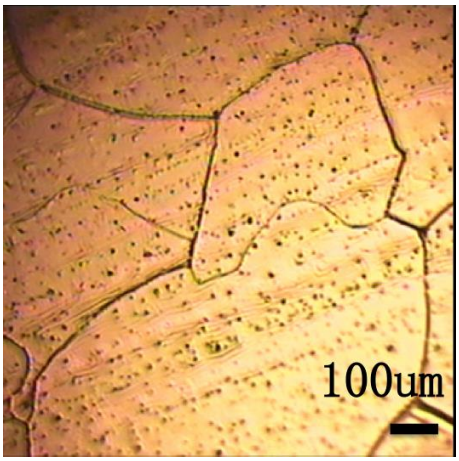

Fig. 5-4 Optical image of the surface of etchant-treated copper film after hydrogen relief annealing.

The best treated sample , i.e. Fig. 5-3 (f), was placed into the tube furnace and annealed for 30 minutes under the atmosphere of H_2 (100 sccm) and Ar (100 sccm) at 1000 ℃. After the annealing process, the strips were eliminated, as shown in Fig. 5-4. The grain sizes grew and reached sub-millimeter scale. However, there are many point defects and line imperfections in the grain. Thereby, it is necessary to investigate the effort of hydrogen relief annealing on solution etched copper foil.

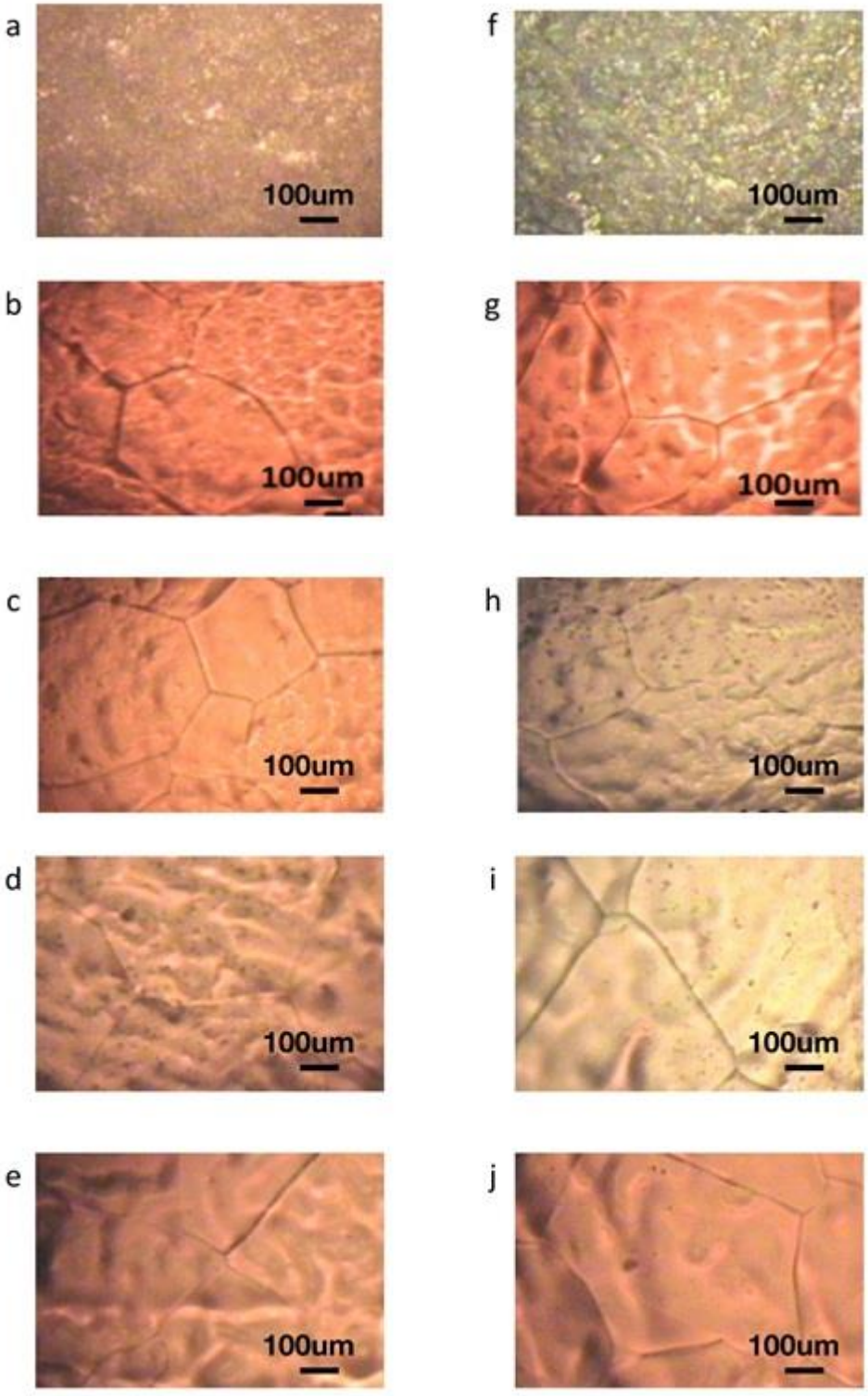

Fig. 5-5 Effect of hydrogen annealing on copper recrystallization under 1000 ℃: (a) $FeCl_3$ 3g: HCl 1ml: H_2O 100ml, ultrasonic-assisted etching for 80 s; (b) annealed at LPCVD for 30 min, with hydrogen partial pressure as 2 Torr; (c) annealed at LPCVD for 30 min, with hydrogen partial pressure as 3 Torr; (d) annealed at LPCVD for 30 min, with hydrogen partial pressure as 4 Torr; (e) annealed at LPCVD for 20 min, with hydrogen partial pressure as 4 Torr; (f) $FeCl_3$ 5g: HCl 1ml: H_2O 100ml, ultrasonic-assisted etching for 40 s; (g) annealed at LPCVD for 30 min, with

hydrogen partial pressure as 2 Torr; (h) annealed at LPCVD for 30 min, with hydrogen partial pressure as 3 Torr; (i) annealed at LPCVD for 30 min, with hydrogen partial pressure as 4 Torr; (j) annealed at LPCVD for 20 min, with hydrogen partial pressure as 4 Torr.

After optimization, two samples were obtained by removing the strips in differnet etchant for 80s and 40s, respectively. The result of dilute solution is better than that of concentrated solution, as shown in Fig.5-5 (a) and (f). After annealing in hydrogen atmosphere, the grounded surface of (a) and (f) become flat and smooth. Some protuberances were removed under hydrogen atmosphere. It is reasonable to deduce that point defects are valleys left by removal of protuberances. We can predict that the density of point defects first increases and then decreases with the increase of hydrogen partial pressure. By comparing the result of (d), (e), (i) and (f), it is found that large hydrogen partial pressure treatment for a long time will not bring to smooth copper foil. The reasons are copper evaporation at the high annealing temperature and hydrogen etching effects on copper foil. The optimum annealing condition is treating at LPCVD for 20 min with hydrogen partial pressure as 4 Torr, as shown in Fig. 5-5 (e) and (j).

Electrochemical polishing technology bases on the electrolysis of metal in the anode under specific electrochemistry condition. Since the protuberances on the metal surface will dissolve in the electrolyte, a flat metal surface can be obtained by electrochemical polishing technology. Here, we used the electrochemical polishing technology to improve the smoothness of copper substrate.

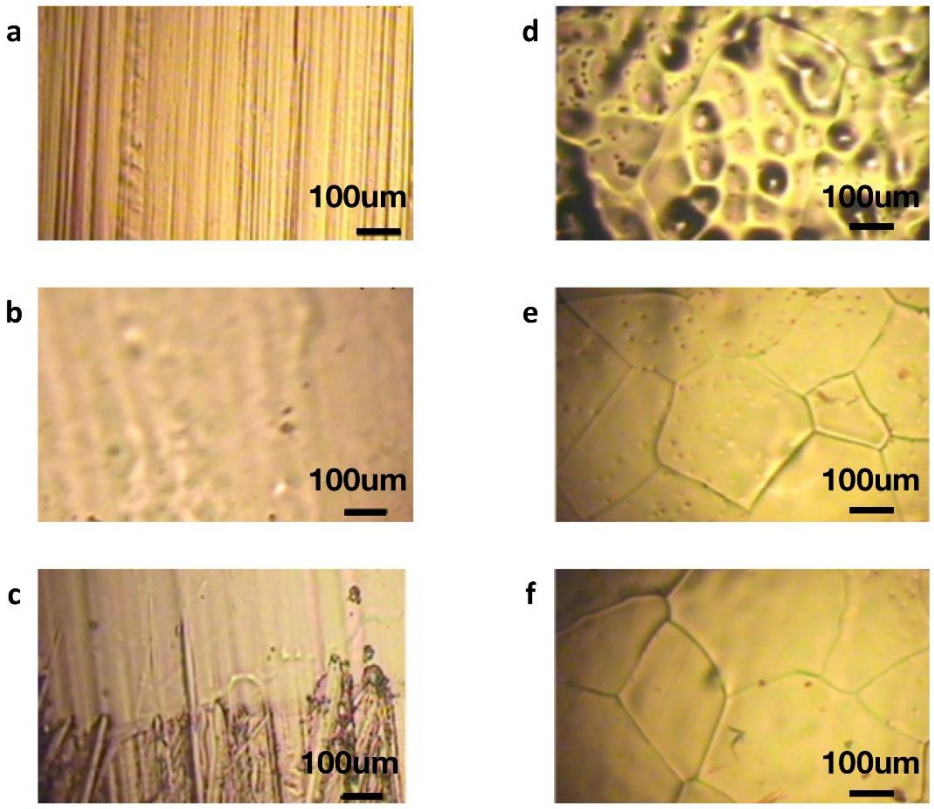

Fig. 5-6 Surface of electrochemically polished copper: (a) untreated copper; (b)electrochemically polished copper; (c) boundary of treated and untreated copper; (d) polished at 1.2V for 30min followed with annealing in H_2 atmosphere; (e) polished at 1.5V for 30min follow with annealing in H_2 atmosphere; (f) polished at 1.5V for 25min follow with annealing in H_2 atmosphere.

The electrolyte is a mixture solution of 100 ml phosphoric acid and 20 ml propylene glycol. A DC power generator is used to provide constant reaction voltage. It can be found from Fig. 5-6 (a), (b), and (c) that the flatness of the surface before and after electrochemical polishing is different. It can also demonstrate from (d) that a low reaction voltage result in a rough surface. The optimum treatment conditions in our case are 1.5 V for 25 minutes.

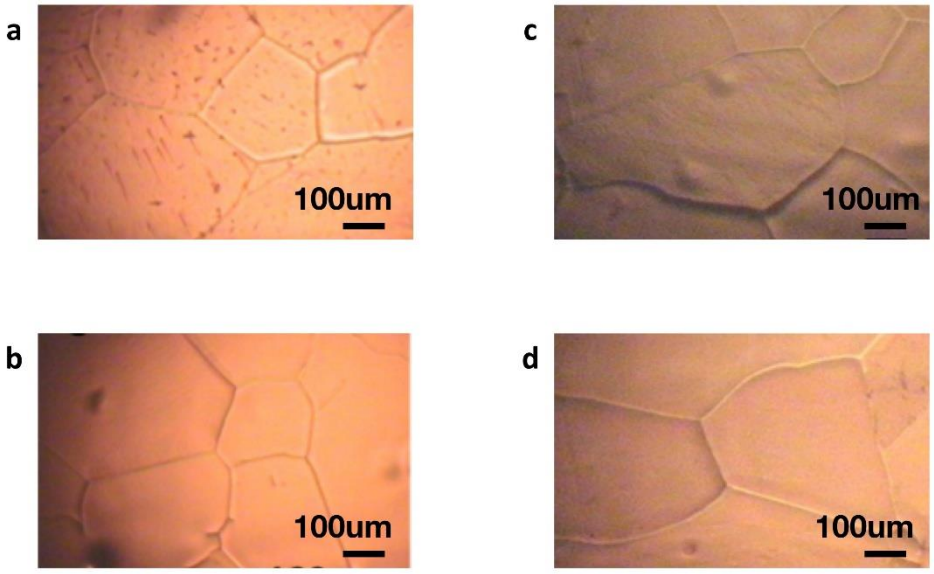

Fig. 5-7 Surface morphologies of Cu foils first polished at 1.5 V for 25 minutes, and then annealed at hydrogen atmosphere: (a) annealing for 30 minutes under 2 Torr hydrogen partial pressure; (b) annealing for 20 minutes under 4 Torr hydrogen partial pressure; (c) annealing for 30 minutes under 3 Torr hydrogen partial pressure; (d) annealing for 30 minutes under 4 Torr hydrogen partial pressure.

After polishing at 1.5V for 25 minutes, copper foils were annealed at various hydrogen partial pressures. At low hydrogen partial pressure, a large number of pinholes can be found on the surface. By increase the hydrogen pressure to 3 Torr and 4 Torr, the pinholes and valleys on the surface of copper foils were eliminated. The difference between those specimens is grain size. Obviously, the average grain size of copper at annealed higher hydrogen pressure is larger. Furthermore, the optimum annealing time is proved to be 30 minutes. A relatively short annealing time results in incompletely elimination of protuberances.

5.1.2 Graphene Synthesis

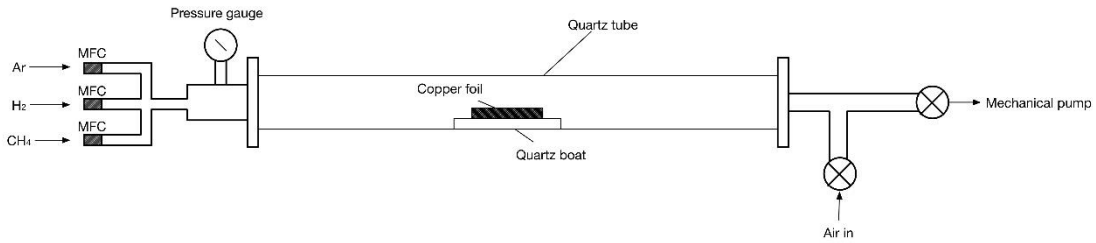

Fig. 5-8 Schematic diagram of the LPCVD system for graphene synthesis.

In this LPCVD system, three ways of gases are fed into the quartz tube. Gases flow rate are controlled by Mass Flow Controllers (MFC). Inert gas, Argon, is used to dilute the carbon concentration in the reaction chamber. Hydrogen is used during copper recrystallization and catalytic decomposition of methane. Methane is the carbon source in graphene synthesis. The partial pressure of each gases can be calculated by values in the pressure gauge and MFCs.

The well prepared copper foils were placed on a quartz boat. The quartz boat is then put into the uniform temperature area of the tube furnace. As shown in Fig. 5-9, at the heating stage (stage I), hydrogen is fed into the system to prevent the copper foil from being oxidation. At the annealing stage (stage II), hydrogen of a flow rate around 20 sccm is fed into the system to smooth the Cu foil surface and increase the grain size in Cu foil. Graphene was deposited on the third stage (stage III) with various flow rates of Methane, hydrogen and argon. After 30 minutes growing stage, the furnace is slid to other side to achieve a rapid cooling. The cooling rate is higher than 10 ℃/min, so that graphene cannot either be etched by hydrogen or be absorbed by copper foil. Hydrogen is also used as protective gas during cooling stage (stage IV).

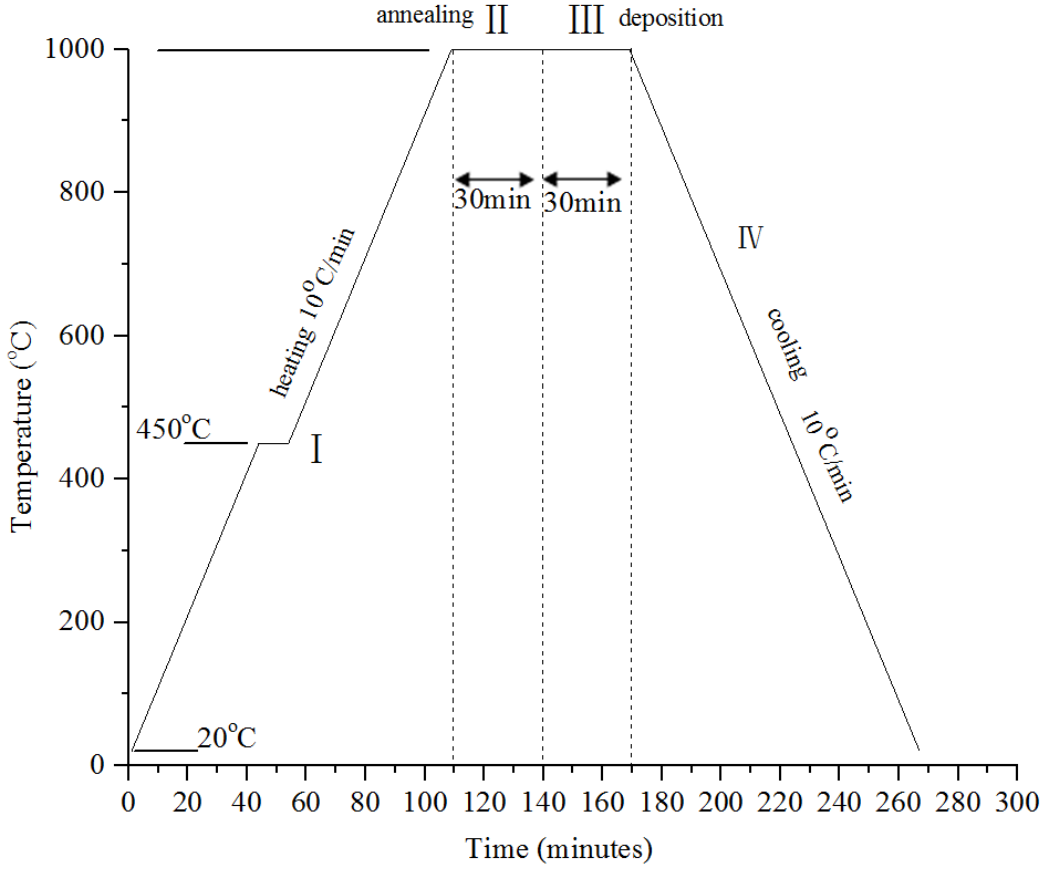

Fig. 5-9 Temperature profile of graphene growth.

5.1.3 Graphene Transfer

As-deposited graphene/Cu foil cannot be used in electronic devices directly. It is required to transfer graphene to an arbitrary substrate for further application. In addition, the characterization of electrical properties and transmittance requires the transfer of graphene to insulating and transparent substrates. Among various transfer technologies, PMMA-assisted (polymethyl methacrylate) transfer is of great success. The transfer process is listed in the flow chart beneath.

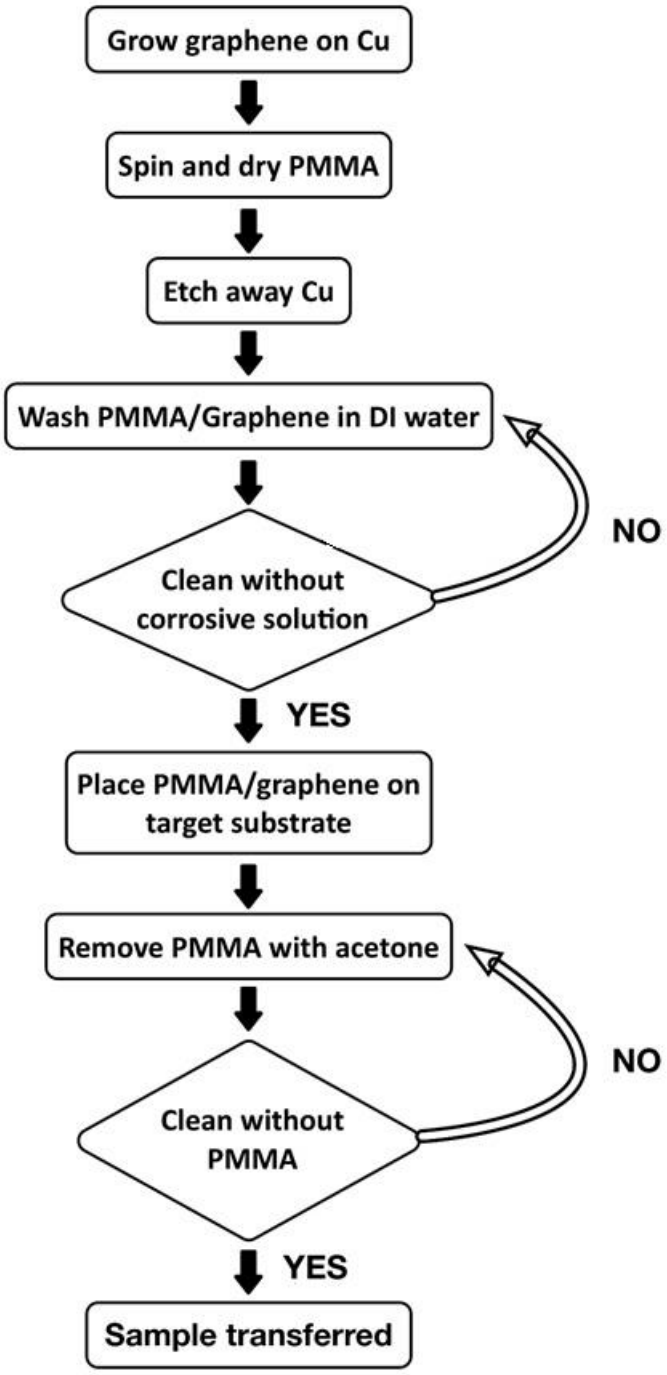

Fig. 5-10 PMMA-assisted graphene transferring process.

Initially, PMMA solution was prepared by mixing 2.075g PMMA (Sigma-Aldrich, 960K) and 50 ml acetone in a sealed reagent bottles and stirring for 2 hours under 50 ℃. Then, the fresh graphene/Cu foil was fixed on a silicon wafer by PE protective film. After adding a few droplets of PMMA solution on the specimen,

the spin coater run at 500 rpm for 5 seconds and 4000 rpm for 60 seconds in sequence. By drying the sample at 90 ℃ for one minute, we obtained a solid PMMA film on graphene/Cu foil with a thickness approximately 300 nm. The PMMA-coated graphene/Cu foil was then put into the $FeCl_3$ solution (0.9mol/L). Generally, it took 24 hours to etch the Cu foil entirely. After that, PMMA/Graphene was rinsed by DI water for three times. Later on, the floating PMMA/graphene was picked up by target substrates, such as glass slide, quartz glass, silicon wafer, and SiO_2/Si. Target substrate/graphene/PMMA was baked at 90℃ for one hour for good adhesion between substrate and graphene. Finally, PMMA was removed by acetone and cleaned in DI water. After the rinsed sample was dried naturally, we obtained the transferred sample. The transferred graphene with and without PMMA can be found in Fig. 5-11.

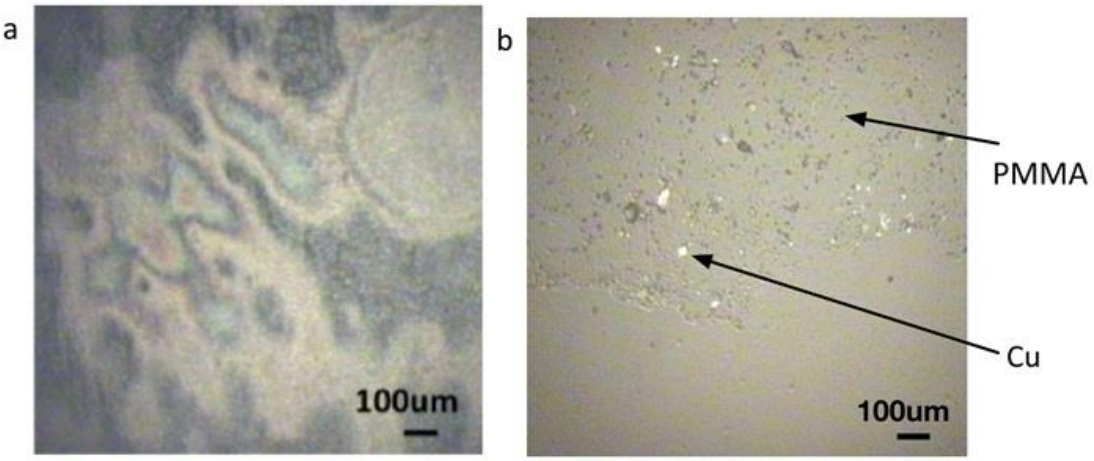

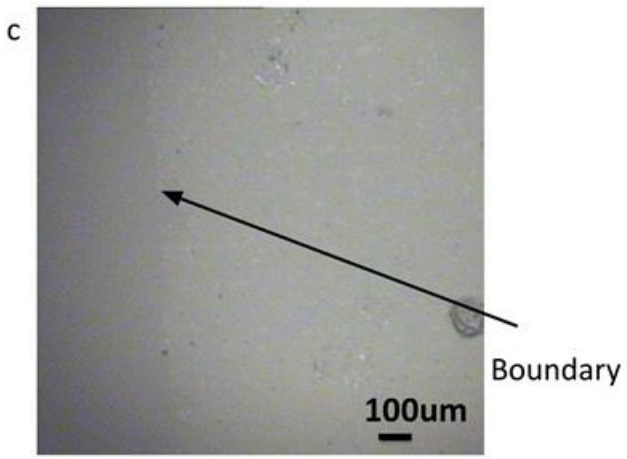

Fig. 5-11 Surface of transferred graphene observed by optical microscopy. (a) graphene/PMMA on glass slide; (b) Cu particle residual and PMMA residual on transferred graphene; (c) boundary of successfully transferred graphene.

5.1.4 Graphene Characterization

The specimen of first trial was characterized by SEM, which is shown in Fig. 5-12. The experiment was carried out at low methane flow rate (5 sccm) for 30 minutes. The graphene islands are discrete. The size of each graphene islands are in sub-micron scale. We can deduce from this figure that low methane flow rate results in a low carbon concentration in the furnace tube and low graphene island grow rate. In our case, it is not enough to obtain a fully covered graphene sheet in 30 minutes with low methane flow rate.

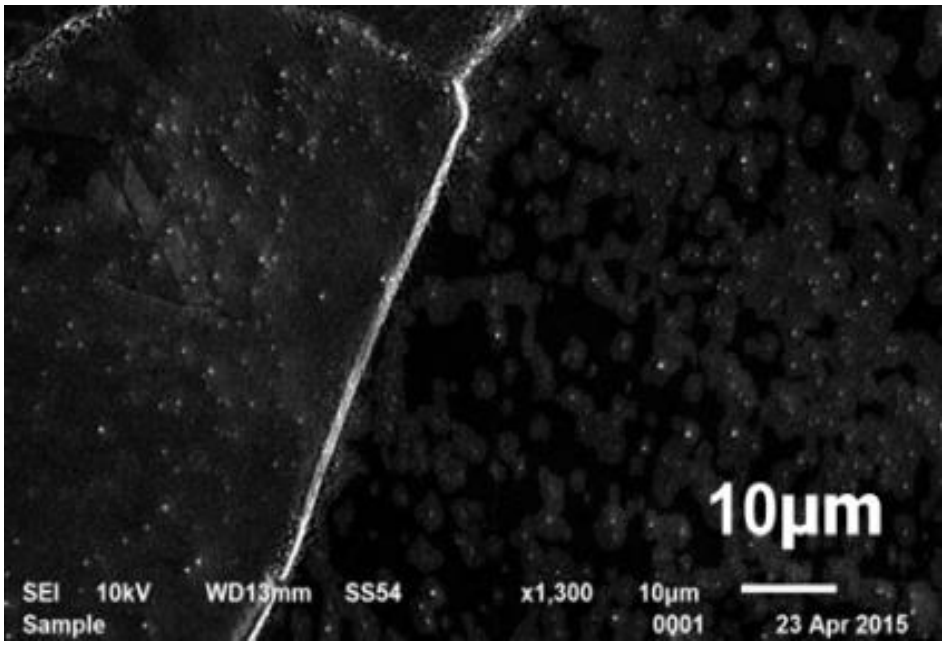

Fig. 5-12 Discrete graphene islands on Cu foil.

Therefore, it is necessary to study the effect of methane flow rate and deposition time. Two group experiments were carried out: one group was with fixed 10 sccm methane flow rate and various deposition time, other group was with fixed the flow rate at 20 sccm and changed deposition times. The graphene were evaluated by Raman Spectroscopy and the results were listed in Fig. 5-13. In the first group, the spectrum changes from graphite shape to graphene shape with increasing deposition time. In addition, the G peak value increased continuously. This phenomenon indicates that thin film tends to be graphene film with the increase of deposition time at a low carbon concentration. When methane flow rate increased to 20 sccm, longer deposition time resulted in poor film. High flow rate of methane results in high carbon concentration. Thus, graphene sheet covers the copper foil rapidly. Extra methane results in the formation of graphite. Best condition can be found at methane flow rate

of 20 sccm and 20 minutes annealing time. At such condition, the obtained graphene has high 2D peak. Also, the ratio of I_{2D}/I_G is superior than other experiment conditions in that group. However, we are aware that the D peak exists in all cases, which indicates poor graphene quality. The SEM figure of thin film can be found in Fig. 5-14 (a-c).

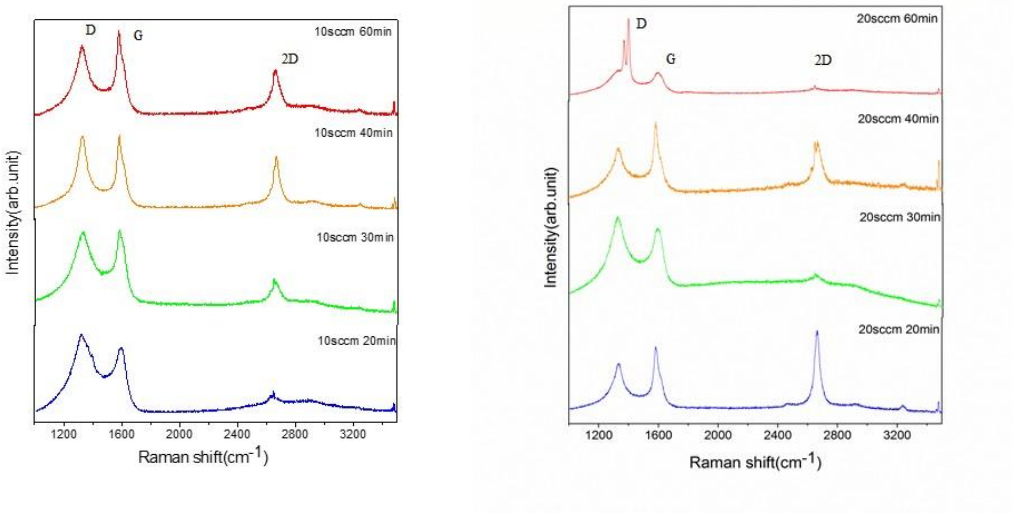

Fig. 5-13 Effects of carbon concentration and deposition time on thin film quality.

Fig. 5-14 are selected examples of graphene film. It can be found in Fig. 5-14 (a) that graphene films can grow across the boundary of copper grains. However, the different color indicate ununiformed thickness of graphene. Holes and wrinkles can also be found in Fig. 5-14(c), which might result from the low flow rate of methane. In the limited growing time, there was not enough carbon atoms decomposed from methane to deposit on copper foils and form the continuous graphene films. In addition, for SEM characterization, the samples are required to have good conductivity to stimulate the secondary electrons during scanning [28]. Therefore, the

high-quality SEM images imply the high conductivity of graphene films. Furthermore, Fig. 5-14 (d-f) shows the surface of single-layer graphene. The smooth and uniform surface manifests the high quality and continuity of graphene.

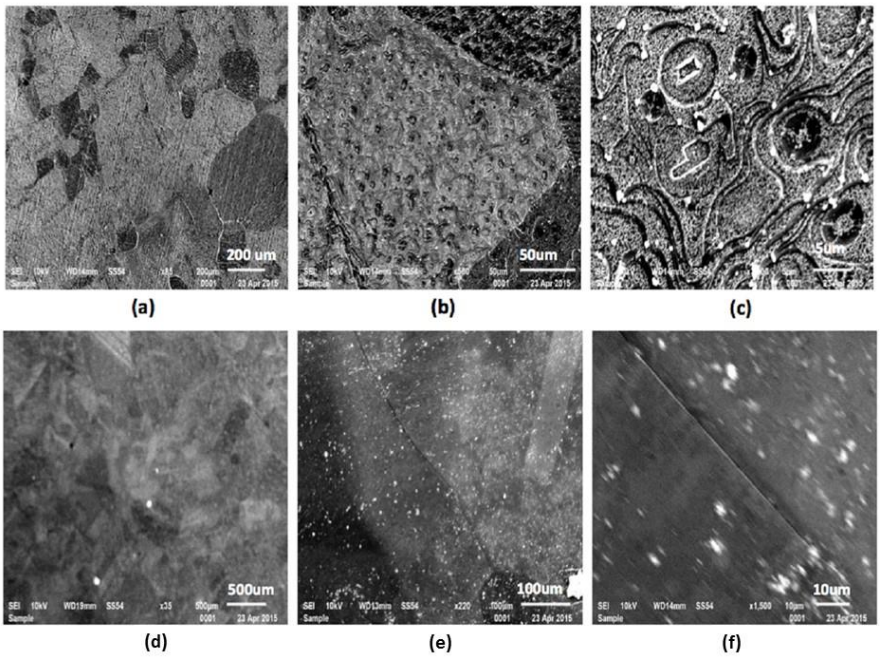

Fig. 5-14 (a-f) SEM images of graphene on Cu foils. (a-c) SEM images of the multi-layer graphene. (d-f) SEM images of the single-layer graphene.

5.2 Stability of CdTe Solar Cells with Graphene as Back Contact Buffer Layer

By employing the solar cell simulator, SCAPS, we had examined the stability of graphene as buffer materials in the CdTe solar cells. By neglecting the degradation arisen from other aspects, such as front contact and intermixing of CdS/CdTe, we had considered the degradation caused by ion diffused from back contact for simplicity. Therefore, most parameters about graphene are from the library of SCAPS, as shown

in Table 4-2.

Table 5-2 Parameters of each layer for SCAPS simulation using graphene as buffer layer

	ZnO:Zr	**CdS**	**CdTe**	**Graphene**
Thickness(nm)	500	25	3000	0.13
bandgap(eV)	3.6	2.4	1.5	0.6
electron affinity(eV)	4	4	3.9	4.29
dielectric permittivity (relative)	9	10	9.4	10
CB effective density of state (cm^{-3})	2.20E+18	2.20E+18	8.00E+17	8.00E+17
VB effective density of state (cm^{-3})	1.80E+19	1.80E+19	1.80E+19	2.00E+18
electron thermal velocity (cm/s)	1.00E+07	1.00E+07	1.00E+07	1.00E+07
hole thermal velocity (cm/s)	1.00E+07	1.00E+07	1.00E+07	1.00E+07
electron mobility(cm/Vs)	1.00E+02	1.00E+02	3.20E+02	1.00E+02
hole mobility (cm/Vs)	2.50E+01	2.50E+01	4.00E+01	1.32E+01
Shallow uniform donor desity $N_D(1/cm^3)$	1.00E+17	1.10E+18	0.00E+00	0.00E+00
Shallow uniform acceptor desity $N_A(1/cm^3)$	0.00E+00	0.00E+00	2.00E+14	

After inserting the Cu-NanoWire layer and the graphene layer into the CdTe solar cells, the solar cells were imposed to stress. It can be found from Fig. 5-15 that all parameters of graphene-based solar cell superior to those of Cu-NWs based solar cells. The decrease of short circuit current and open circuit voltage are similar over time. Hence, it can be deduced that the degradation in efficiency is mostly caused by the decline in fill factor. Therefore, graphene is expected to be a robust back contact buffer layer for CdTe solar cells in the future.

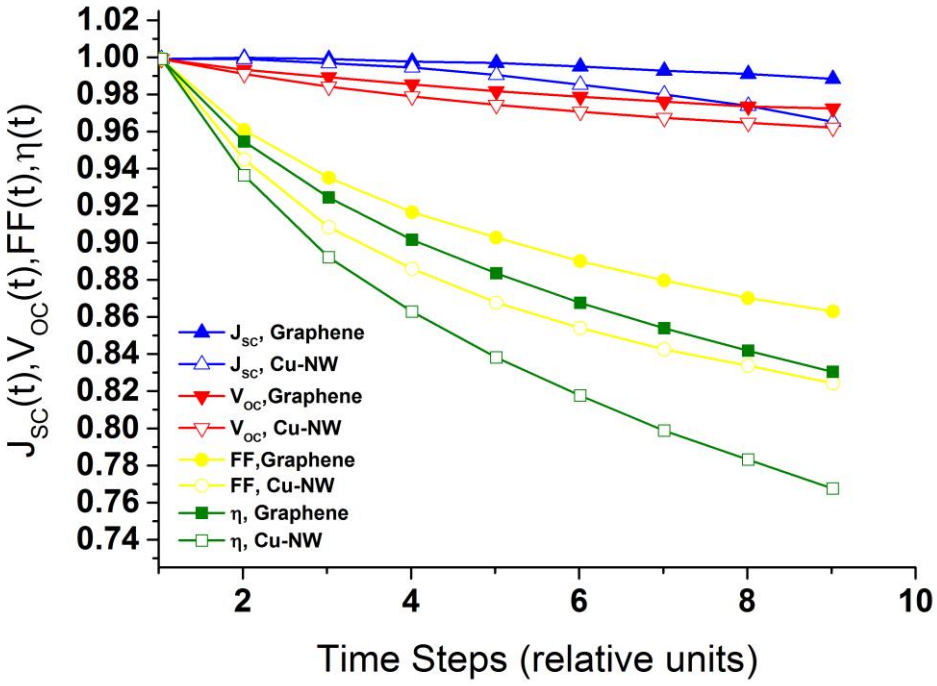

Fig. 5-15 Degradation of CdTe solar cells with different back contact buffer layer.

References for the Chapter

1. Erra, S.; Shivakumar, C.; Zhao, H.; Barri, K.; Morel, D. L.; Ferekides, C. S., An effective method of Cu incorporation in CdTe solar cells for improved stability. *Thin Solid Films* **2007,** 515, (15), 5833-5836.
2. Zhou, J.; Wu, X.; Duda, A.; Teeter, G.; Demtsu, S. H., The formation of different phases of CuxTe and their effects on CdTe/CdS solar cells. *Thin Solid Films* **2007,** 515, (18), 7364-7369.
3. Gessert, T. A.; Metzger, W. K.; Dippo, P.; Asher, S. E.; Dhere, R. G.; Young, M. R., Dependence of carrier lifetime on Cu-contacting temperature and ZnTe:Cu thickness in CdS/CdTe thin film solar cells. *Thin Solid Films* **2009,** 517, (7), 2370-2373.
4. Demtsu, S. H.; Albin, D. S.; Pankow, J. W.; Davies, A., Stability study of CdS/CdTe solar cells made with Ag and Ni back-contacts. *Solar Energy Materials and Solar Cells* **2006,** 90, (17), 2934-2943.
5. Romeo, N.; Bosio, A.; Tedeschi, R.; Romeo, A.; Canevari, V., A highly efficient and stable CdTe/CdS thin film solar cell. *Solar Energy Materials and Solar Cells* **1999,** 58, (2), 209-218.
6. Romeo, N.; Bosio, A.; Tedeschi, R.; Canevari, V., Growth of polycrystalline CdS and CdTe thin layers for high efficiency thin film solar cells. *Mater. Chem. Phys.* **2000,** 66, (2–3), 201-206.
7. Schmidt, T.; Durose, K.; Rothenhausler, C.; Lerch, M., Chemical stability of Sb2Te3 back contacts to CdS/CdTe solar cells. *Thin Solid Films* **2000,** 361, 383-387.
8. Abken, A. E.; Bartelt, O. J., Sputtered Mo/Sb2Te3 and Ni/Sb2Te3 layers as back contacts for CdTe/CdS solar cells. *Thin Solid Films* **2002,** 403–404, 216-222.
9. Lin, H.; Xia, W.; Wu, H. N.; Tang, C. W., CdS/CdTe solar cells with MoOx as back contact buffers. *Applied Physics Letters* **2010,** 97, (12), 123504.
10. Gretener, C.; Perrenoud, J.; Kranz, L.; Baechler, C.; Yoon, S.; Romanyuk, Y.

E.; Buecheler, S. G., 2013 #1311}; Tiwari, A. N., Development of MoOx thin films as back contact buffer for CdTe solar cells in substrate configuration. *Thin Solid Films* **2013,** 535, 193-197.

11. Yi, X.; Liou, J. J., Surface oxidation of polycrystalline cadmium telluride thin films for Schottky barrier junction solar cells. *Solid-State Electronics* **1995,** 38, (6), 1151-1154.
12. T. Lin; F. Huang; Liang，, J.; Y. Wang, *Energy Environ. Sci.* **2011**, (4), 862－865.
13. L. S. Panchokarla; K. S. Subramanyam; S. K. Saha, A. G.; H. R. Krishnamurthy; Waghmare，, U. V.; C. N. R. Rao, *Adv. Mater.* **2009**, (21), 4726－4730.
14. Kirkland, N. T.; Schiller, T.; Medhekar, N.; Birbilis, N., Exploring graphene as a corrosion protection barrier. *Corrosion Science* **2012,** 56, 1-4.
15. Guo, F.; Silverberg, G.; Bowers, S.; Kim, S.-P.; Datta, D.; Shenoy, V.; Hurt, R. H., Graphene-Based Environmental Barriers. *Environmental Science & Technology* **2012,** 46, (14), 7717-7724.
16. X. Li, e. a., Evolution of graphene growth on Ni and Cu by carbon isotope labeling. *Nano Lett.* 9, (12), 4268–72.2009.
17. W .H .Zhang, e. a., Mechanisms of Graphene Growth on Metal Surfaces: Theoretical Perspectives. *Small* **2014,** 10, (1002), 1-5.
18. K.I. Bolotin, e. a., Ultrahigh electron mobility in suspended graphene. *Solid State Commum* **2008,** 146, 351-355.
19. Z. Xiao, e. a., Graphene-Based Electrodes. *Advanced Material* **2014,** 24.
20. K. S. Anseth, e. a., Progress in Materials Science. *Journal* **2011,** 56, 1178-1271.
21. A. A. Balandin, e. a., Superior Thermal Conductivity of single-layer graphene. *Nano Lett.* 8, (3), 902-907.
22. C. M. Seah, e. a., Mechanisms of graphene growth by chemical vapour deposition on transition metals. *Carbon* **2014,** 70, 1-21.
23. P. W. Sutter, e. a., Epitaxial graphene on ruthenium. *Nat Mater* **2008,** 7, (5),

406–411.

24. M. R. Kim, e. a., Effect of hydrogen plasma on growth of Ir thin film by plasma enhanced hybrid atomic layer deposition. *Microelectronic Engineering* **2012,** 98, 400-404.

25. S. I. Song, e. a., Hydrogen-plasma-assisted hybrid atomic layer deposition of Ir thin film as novel Cu diffusion barrier. *Surfcoat* **2012,** 211, 14-17.

26. E. Cazzanelli, e. a., Spectroscopic characterization of graphene films grown on Pt (1 1 1) surface by chemical vapor deposition of ethylene. *Journal* **2013,** 44, (10), 1393-1397.

27. Li, X.; Magnuson, C. W.; Venugopal, A.; Tromp, R. M.; Hannon, J. B.; Vogel, E. M.; Colombo, L.; Ruoff, R. S., Large-Area Graphene Single Crystals Grown by Low-Pressure Chemical Vapor Deposition of Methane on Copper. *Journal of the American Chemical Society* **2011,** 133, (9), 2816-2819.

28. Cai, X. Study of Chemical Vapor Deposition Growth of Graphene on Copper Surface Taiyuan University of Technology, 2013.

Chapter 6: Conclusion and Further Works

In conclusion, the thesis focused on developing novel materials for scarce materials and their substitutions by introducing straight forward technology for CdTe thin film doping. Two novel materials were grown and characterized. The two materials are: zirconium doped zinc oxide and graphene. After analysis, it was found that zirconium doped zinc oxide has superior transmittance and thermal stability when compare to aluminum doped zinc oxide. In addition, the effect of the buffer layer on solar cells degradation was modeled and further showed that the solar cells with graphene as buffer layer exihibits good stability. In addition, a simple copper doping method was proposed to substitute tellurium doping in CdTe thin films.

It is known that indium tin oxide has low thermal stability at high temperature. At temperatures above 700K, indium ions diffuse to the neighboring films and further destroy the solar cells. Unfortunately, the fabrication of CdTe thin film solar cells involves a complex manufacturing processes, which requires the development of stable and abundant materials substitution. By precisely doping zirconium oxide into zinc oxide using ALD, it is found that the transmittance shows blue shift with the increasing zirconium concentration. In other words, the bandgap energy Eg increases with the zirconium concentration from 3.21 eV to 3.33 eV. In addition, XRD indicated that ZrZO films have an orientation of (002) perpendicular to the substrate surface and

the intensity of the ZnO peak (002) increases with increasing annealing temperature.

Other barriers that hinder the development of CdTe solar cells are large recombination rate and low carrier concentration. Since the photon absorber in CdTe solar cells is a polycrystalline thin film, grain boundaries become recombination centers and further result in a low power conversion efficiency. $CdCl_2$ post-treatment under air atmosphere is proved to be an effective method to solve the problem. The $CdCl_2$–treated vacuum evaporated CdTe thin film shows larger grain size. The grain size increases from few tens of nanometer to more than one hundred nanometers; the peak intensities increase significantly in every orientation except the (111).

Copper ion has dual roles in CdTe solar cells. On one hand, it acts as a dopant that increases the carrier concentration in CdTe thin film; on the other hand, large amount of copper leads to serious cell degradation. Copper ion is an impurity with fast diffusion in CdTe layer. Accelerated by the build-in electric field, copper ions will accumulate at the CdS/CdTe interface. The large number of copper ions form recombination centers and hence result in degradation. Therefore, it is necessary to introduce a buffer layer to prevent extra copper ions or metal ions diffusing from metallic electrode. Through simulation, it is found that carbon-based buffer layer performs better than that of telluride buffer layers. Copper-based buffer layer shows fastest degradation. Later on, we extracted the parameters from the graphene synthesized by LPCVD and applied in to the degradation model. The result showed that graphene has the potential to be the ion diffusion barrier among the materials that we have investigated.

According to the roadmap of photovoltaics development, 15% of the global electricity demand relies on the renewable energy utilization in 2050. Thus, 50% solar fraction scenarios translate into 12.5 TWp photovoltaics capacity. The potential market of thin film solar cells is expected to be approximately one TWp. Since the estimation was based on the current market outlook, this result can be rescaled easily to accommodate the market share. It should also be noted that chemical elements used in photovoltaics technologies differ greatly from that in abundance. Unlike many other materials, the cost of scarce elements does not benefit from increasing demand and economics of scope. On the contrary, the increase in demand of rare elements will likely raise the solar cells and module cost. Hence, effects of scarce elements of photovoltaics deployment are very difficult to predict and control. Therefore, novel materials are explored to substitute the scarce elements involved materials, and thus to ease the constraint. Carbon-based films are expected to be much more economical and versatile; among all the carbon-based nanomaterials, graphene is the most perspective material.

The introduction of graphene as the transparent conducting film has been regarded as a potential solution. Graphene has many superior properties, including high flexibility, excellent conductivity, ultra-high transparency in all wavelengths, and comparative low thickness. High flexibility of graphene allows the application on flexible electronic devices. In comparison, the mechanical brittleness limits the application of traditional transparent conductors. The properties such as conductivity and transparency make graphene a perfect transparent conductor. Large area graphene

films have successfully synthesized by chemical vapor deposition. With four layers of graphene, the sheet resistance and transmittance get close to the values of conventional transparent conducting oxide. However, there are constraints on the synthesis technology and transfer method. Hence, it is necessary to work on this topic to grow large grain graphene to reduce the sheet resistance. In addition, straight forward graphene doping technologies are crucial for low sheet resistance transparent conductor application.

Appendix I

```
unction varargout = test1(varargin)
% TEST1 MATLAB code for test1.fig


% --- Executes on button press in calculate.
function calculate_Callback(hObject, eventdata, handles)
% hObject    handle to calculate (see GCBO)
% eventdata  reserved - to be defined in a future version of MATLAB
% handles    structure with handles and user data (see GUIDATA)
t1=str2num(get(handles.t1,'String'));
t2=str2num(get(handles.t2,'String'));
t3=str2num(get(handles.t3,'String'));
l1=str2num(get(handles.lamb1,'String'));
l2=str2num(get(handles.lamb2,'String'));
l3=str2num(get(handles.lamb3,'String'));
t1=t1/100;
t2=t2/100;
t3=t3/100;
na=1.5;
nb=1;
```

```
if get(handles.radiobutton7,'value')    //two maximum and one minimum
        NN=(na^2+nb^2)/2+2*na*nb*(t1-t2)/(t1*t2);
        n1=(NN+(NN^2-na^2*nb^2)^(1/2))^(1/2);
        NN=(na^2+nb^2)/2+2*na*nb*(t3-t2)/(t3*t2);
        n2=(NN+(NN^2-na^2*nb^2)^(1/2))^(1/2);
        thick=l1*l3/(2*(n1*l3-n2*l1));
        thickness=num2str(thick);
        indexlower=num2str(n1);
        indexhigher=num2str(n2);
        set(handles.lowerindex,'String',indexlower);
        set(handles.higherindex,'String',indexhigher);
        set(handles.thick,'String',thickness);
        c11=(n1+na)*(nb+n1);
        c21=(n1-na)*(nb-n1);
        alpha1=c11*(1-(t1/t2)^(1/2))/(c21*(1+(t1/t2)^(1/2)));
        k1=log(1/alpha1)/thick;
        c12=(n2+na)*(nb+n2);
        c22=(n2-na)*(nb-n2);
        alpha2=c12*(1-(t3/t2)^(1/2))/(c22*(1+(t3/t2)^(1/2)));
        k2=log(1/alpha2)/thick;
        absorblower=num2str(k1);
```

```
        absorbgreater=num2str(k2);
        set(handles.lower,'String',k1);
        set(handles.greater,'String',k2);

elseif get(handles.radiobutton8,'value') //two minimum and one maximum
        NN=(na^2+nb^2)/2+2*na*nb*(t2-t1)/(t1*t2);
        n1=(NN+(NN^2-na^2*nb^2)^(1/2))^(1/2);
        NN=(na^2+nb^2)/2+2*na*nb*(t2-t3)/(t3*t2);
        n2=(NN+(NN^2-na^2*nb^2)^(1/2))^(1/2);
        thick=l1*l3/(2*(n1*l3-n2*l1));
        thickness=num2str(thick);
        indexlower=num2str(n1);
        indexhigher=num2str(n2);
        set(handles.lowerindex,'String',indexlower);
        set(handles.higherindex,'String',indexhigher);
        set(handles.thick,'String',thickness);
        c11=(n1+na)*(nb+n1);
        c21=(n1-na)*(nb-n1);
        alpha1=c11*(1-(t2/t1)^(1/2))/(c21*(1+(t2/t1)^(1/2)));
        k1=log(1/alpha1)/thick;
        c12=(n2+na)*(nb+n2);
        c22=(n2-na)*(nb-n2);
```

```
        alpha2=c12*(1-(t2/t3)^(1/2))/(c22*(1+(t2/t3)^(1/2)));
        k2=log(1/alpha2)/thick;
        absorblower=num2str(k1);
        absorbgreater=num2str(k2);
        set(handles.lower,'String',k1);
        set(handles.greater,'String',k2);
end


% --- Executes on button press in reset.
function reset_Callback(hObject, eventdata, handles)
% hObject    handle to reset (see GCBO)
% eventdata  reserved - to be defined in a future version of MATLAB
% handles    structure with handles and user data (see GUIDATA)
set(handles.t1,'String','0')
set(handles.t2,'String','0')
set(handles.t3,'String','0')
set(handles.lamb3,'String','0')
set(handles.lamb2,'String','0')
set(handles.lamb1,'String','0')
set(handles.thick,'String','0')
set(handles.lower,'String','0')
set(handles.greater,'String','0')
```

```
set(handles.lowerindex,'String','0')

set(handles.higherindex,'String','0')
```